INFORMATION TO USERS

This manuscript has been reproduced from the microfilm master. UMI films the text directly from the original or copy submitted. Thus, some thesis and dissertation copies are in typewriter face, while others may be from any type of computer printer.

The quality of this reproduction is dependent upon the quality of the copy submitted. Broken or indistinct print, colored or poor quality illustrations and photographs, print bleedthrough, substandard margins, and improper alignment can adversely affect reproduction.

In the unlikely event that the author did not send UMI a complete manuscript and there are missing pages, these will be noted. Also, if unauthorized copyright material had to be removed, a note will indicate the deletion.

Oversize materials (e.g., maps, drawings, charts) are reproduced by sectioning the original, beginning at the upper left-hand corner and continuing from left to right in equal sections with small overlaps. Each original is also photographed in one exposure and is included in reduced form at the back of the book.

Photographs included in the original manuscript have been reproduced xerographically in this copy. Higher quality 6" x 9" black and white photographic prints are available for any photographs or illustrations appearing in this copy for an additional charge. Contact UMI directly to order.

UMI

A Bell & Howell Information Company
300 North Zeeb Road, Ann Arbor MI 48106-1346 USA
313/761-4700 800/521-0600

A LOW POWER PULSED ARCJET THRUSTER FOR SPACECRAFT PROPULSION

BY

GARY FRANCIS WILLMES

B.S., Rensselaer Polytechnic Institute, 1985
M.S., University of Dayton, 1987

THESIS

Submitted in partial fulfillment of the requirements
for the degree of Doctor of Philosophy
in Aeronautical and Astronautical Engineering
in the Graduate College of the
University of Illinois at Urbana-Champaign, 1997

Urbana, Illinois

UNIVERSITY OF ILLINOIS AT URBANA-CHAMPAIGN

THE GRADUATE COLLEGE

MAY 1997
(date)

WE HEREBY RECOMMEND THAT THE THESIS BY

GARY FRANCIS WILLMES

ENTITLED A LOW POWER PULSED ARCJET THRUSTER

FOR SPACECRAFT PROPULSION

BE ACCEPTED IN PARTIAL FULFILLMENT OF THE REQUIREMENTS FOR

THE DEGREE OF DOCTOR OF PHILOSOPHY

Rodney L. Burton
Director of Thesis Research

Wayne C. Solomon
Head of Department

Committee on Final Examination†

Rodney L. Burton
Chairperson

H. C. Beddini

Herman Krier

Lee H. Sentman

† Required for doctor's degree but not for master's.

O-517

Abstract

An electrothermal thruster that operates in a pulsed mode at low power (<200 W) is investigated. The thruster, called a pulsed arcjet, uses a capacitor and a pulse-forming electrical circuit to transfer stored electrical energy to a helium propellant gas in 3-10 μsec arc discharges at repetition rates of 550 to 2600 pulses-per-second with pulse energies from 24 to 130 mJ. The arc discharges occur in a cylindrical capillary upstream of a converging-diverging nozzle, and all the energy addition occurs in the subsonic region. Peak currents in the arc are 110 to 270 amps. Pulsed arcjet performance at thermal steady state is measured for two 20 degree half angle conical nozzles with area ratios of 20 and 230. Thrust levels from 10 to 30 mN are measured on an inverted pendulum-type thrust stand, and input power levels from 24 to 119 watts are determined from measurements of pulse rate and breakdown voltage. A maximum specific impulse of 305 seconds is achieved with 38% efficiency.

A time-dependent, quasi-1D numerical model is developed to evaluate energy losses in the pulsed arcjet. The numerical model uses a time-marching procedure and the MacCormack predictor-corrector algorithm. Viscous and heat transfer effects are incorporated though a friction factor and an average heat transfer coefficient. A numerical study of nozzle parameters, capillary geometry, wall temperature, and pulse energy shows that the performance is insensitive to capillary and nozzle geometry and that thermal characteristics are the dominant factor affecting performance. The specific impulse and efficiency of the pulsed arcjet are found to be sensitive to wall temperature due to heat transfer losses in the subsonic region. Viscous effects become important as the specific energy increases, and the 20:1 nozzle has a higher specific impulse than the 230:1 nozzle above 12 MJ/kg.

A pulse-forming electrical circuit is developed to reduce energy losses in the storage capacitor, and greater than 85% of the initial stored energy is transferred to the arc in a unipolar pulse. A high current diode installed across the capacitor terminals is used to eliminate voltage reversals in the current. The experimental breakdown voltage of the helium gas between the electrodes is found to follow a

Paschen relationship where the minimum electrode separation distance is used in evaluating the data. The arc voltage is approximately constant during the discharge. A channel model for the arc gives a calculated value for the arc voltage that is consistent with experiment between 95 and 180 volts.

This thesis is dedicated to my daughter, Megan.

Acknowledgements

I am indebted to my advisor and mentor, Professor Rodney Burton, who converted me from launch vehicles to electric propulsion. He taught me a great deal about how to solve practical engineering problems, but more importantly he showed me the value of engineering insight. The pulsed arcjet experiment was his concept, and I appreciate the opportunity to study with him. I hope that I will have the good fortune to work with him again in the future.

The other faculty that I wish to acknowledge are Professor Wayne Solomon, for believing in my potential from the beginning and giving me the chance to test my abilities; Professor Lee Sentman, who taught me that a Ph.D. represents the ability to formulate and solve new problems; Professor Herman Krier, for his special combination of technical expertise and good humor; and Professor Shee Mang Yen, for giving me encouragement when I needed it.

The friends that I wish to note here include Nick Tiliakos, who was my office mate for over four years. We shared many of the same frustrations, setbacks and problems, and our many discussions benefited this work immensely. Scott Bufton finished his thesis before me, and my final year of study was much more difficult without his steady presence and good nature. Other people that deserve more mention than I can include here are Shawn Gordon, Mike Wilson, Bruce Powers, Stu Bushman, and Dave Jenkins. I am glad that our paths crossed, and I hope they will again.

The person who sacrificed the most for this research is my wife, Liesel, who had to tolerate my long hours and sustained absences while I was working on this thesis. To her I owe special appreciation for her support and understanding of what seemed to be an endless task.

Table of Contents

List of Symbols

A	Nozzle area [m^2]
A_{WALL}	Capillary wall area for heat transfer [m^2]
a	Sound speed [m/s]
b_0	Impact parameter for 90° scattering [m]
C	Capacitance [F], electrical conductivity constant [ohm-m]$^{-1}$
C_D	Discharge coefficient
C_P	Specific heat [J/kg-K]
D	Capillary diameter [m]
DF	Capacitor dissipation factor
d	Paschen breakdown distance [m]
d*	Nozzle throat diameter [m]
E	Energy [J], electric field strength [V/m]
e	Specific energy [J/kg]
f	Frequency [Hz], friction factor
g	Standard gravity [m/s^2]
g_i	Feedback control gains
h	Enthalpy [J/kg-K]
$\bar{h}$	Average convection coefficient [W/m^2-K]
h_0	Total enthalpy [J/kg]
I	Arc current [amps], impulse [N-s]
I_{SP}	Specific impulse [s]
I_{EFF}	Effective ionization potential [eV]
k_B	Boltmann constant [J/K]
L	Capillary length [m]
L_{ARC}	Arc inductance [H]
L_{CAP}	Capacitor internal inductance [H]
L_{EXT}	Circuit inductance [H]
M_0	Initial payload mass [kg]
M_P	Total propellant mass exiting nozzle during one pulse [kg]

MW	Molecular weight [kg/kmol]
m	Propellant mass [kg]
$\dot{m}$	Mass flow rate [kg/sec]
Nu	Nusselt number
n	Number density [m^{-3}]
P	Pressure [Pa], perimeter of conductor [m], power [W]
P_{AMB}	Ambient pressure [Pa]
PPS	Pulse rate [pulses-per-second]
Pr	Prandtl number
Q	Heat transfer rate [W]
Q_{ea}	Electron-neutral collision cross section [m^2]
Q_{ei}	Electron-ion collision cross section [m^2]
q	Heat transfer rate per unit mass [W/kg]
R	Capillary radius [m], specific gas constant [J/kg-K]
Re	Reynolds number
R_{ARC}	Arc resistance [Ω]
R_{ESR}	Capacitor equivalent series resistance [Ω]
R_{EXT}	High frequency resistance [Ω]
R_t	Nozzle throat radius of curvature [m]
r	Radial distance from centerline [m]
r_0	Arc radius [m]
rc	Adiabatic recovery factor
T	Temperature [K]
T_1	Propellant inlet temperature [K]
T_{AW}	Adiabatic wall temperature [K]
T_{HR}	Thrust [N]
T_m	Arc channel mean temperature [K]
T_{WALL}	Wall temperature [K]
t	Time [sec]
U_E	Exhaust velocity [m/s]

U_{EQ}	Equivalent exhaust velocity [m/s]
u	Flow velocity [m/s]
V	Voltage [volts], volume [m^3]
V_{ARC}	Arc voltage [volts]
V_B	Breakdown voltage [volts]
V_{DIODE}	Voltage drop in diode [volts]
ΔV	Orbital velocity change [m/s]
v	Velocity [m/s]
x	Axial location [m]
x_{SET}	Initial thrust stand setpoint [m]

Greek

α	Nozzle divergent section half angle [deg], ionization fraction [%], Townsend primary ionization coefficient [m^{-1}]
δ	Conductor skin depth [m]
γ	Effective secondary ionization coefficient, ratio of specific heats
η	Thrust efficiency [%]
η_C	Circuit transfer efficiency [%]
κ	Thermal conductivity [W/m-K]
Λ	Coulomb logarithm
μ	Viscosity [kg/m-sec], relative permeability [H/m]
ρ	Density [kg/m^3]
σ	Electrical conductivity $[ohm\text{-}m]^{-1}$
τ	Time between pulses = 1 / PPS [sec]
θ	Nozzle convergent section half angle [deg]
ω	Characteristic frequency for resistance [rad/s], measurement uncertainty
ω / α	Townsend's second ionization coefficient

Subscripts

1	Propellant inlet location
2	Capillary
CAP	Capacitor, capillary
E	Nozzle exit plane
EXT	External circuit
SS	Steady state
*	Nozzle throat

1. Introduction

Propulsion systems onboard spacecraft are used for a number of different operations, such as satellite attitude control, stationkeeping and orbit maintenance, orbit-raising, and drag makeup. For many commercial, scientific and defense missions, the mass of the propulsion system is a major fraction of the total payload mass. If the propulsion system mass can be reduced, either the useful payload capability can be increased, or possibly a smaller and less expensive launch vehicle can be used to launch the spacecraft to its desired orbit. Electric thrusters provide enough improvement in payload mass fraction over chemical thrusters that electric propulsion systems are likely to be selected for an increasing number of satellites over the next decade.

At the present time, spacecraft propulsion systems are predominantly based on chemical monopropellant or bipropellant thrusters. Chemical thrusters use a chemical reaction to heat a propellant to a high temperature in a combustion chamber, which is connected to a converging-diverging nozzle. The exhaust velocity obtained in an isentropic expansion through a supersonic nozzle is proportional to $\sqrt{T / MW}$, where T is the gas temperature, and MW is the molecular weight. While higher exhaust velocities are achieved by increasing T, the maximum temperature that can be attained by chemical propulsion is limited by the energy stored in the chemical bonds of the propellant. Thus, chemical thrusters have a maximum performance limit established by the propellant chemistry.

Electric thrusters overcome the exhaust velocity limits of chemical thrusters in a number of ways. Electrothermal thrusters, such as arcjets and resistojets, heat the propellant to a higher temperature than can be achieved in a chemical reaction by using an external power source on-board the spacecraft. This is a useful tradeoff because power from the spacecraft solar arrays is a renewable resource, whereas the depletion of the spacecraft's propellant often represents the end of the satellite's useful life. A thermal expansion process is not the only mechanism for mass

acceleration, and non-thermal types of thruster have also been developed. These can generally be classified as either electrostatic or electromagnetic devices, depending on the physics of their operation. Electrostatic devices, such as ion thrusters, use an applied electric field to accelerate positively-charged heavy ions in an $\overline{F} = q\,\overline{E}$ interaction. Electromagnetic thrusters are characterized by magnetic and electric fields that are configured in such a way as to create a $\bar{j} \times \overline{B}$ force to accelerate the gas particles. These different categories of electric thruster and their physical principles are described by Jahn in the well-known text Physics of Electric Propulsion.[1]

1.1 Definitions and Basic Equations

The selection of the propulsion system, whether it be chemical or one of the classes of electric thruster, depends on the overall mission requirements for a given spacecraft. While chemical thrusters may be characterized by thrust level and specific impulse, I_{SP}, electric thrusters are generally compared in terms of power level, P, and thrust efficiency, η, in addition to specific impulse. These three parameters are described below.

1.1.1 Specific Impulse

The fundamental concept that defines the problem of spacecraft propulsion is Newton's second law of motion. The momentum of a spacecraft can be changed by accelerating mass away from the spacecraft. Hence the problem becomes one of accelerating a part of the spacecraft, i.e. the propellant, at a high velocity away from the spacecraft. When applying the principle of conservation of momentum to a rocket, the thrust for one-dimensional steady flow is given by,

$$T_{HR} = \dot{m}_E U_E + (P_E - P_{AMB})A_E = \dot{m}_E U_{EQ} \quad [N] \tag{1.1}$$

The variable U_{EQ} is an equivalent exhaust velocity that includes the pressure term in the thrust equation. In many electrothermal devices, the pressure term is small,

and U_E and U_{EQ} are used interchangeably. The specific impulse, I_{SP}, is a useful parameter in comparing the performance of different propulsion devices,

$$I_{SP} = \frac{T_{HR}}{g\dot{m}} = \frac{U_{EQ}}{g} \quad [\text{sec}] \tag{1.2}$$

The importance of the specific impulse in spacecraft propulsion is shown in the relationship for the ratio of the final payload mass to the initial payload mass for a given orbital change, characterized by ΔV,

$$M_F = M_0 \exp\left(\frac{-\Delta V}{U_{EQ}}\right) \quad [kg] \tag{1.3}$$

Because the influence of propellant exhaust velocity on payload mass is exponential, the specific impulse tends to be a critical parameter for evaluating thruster performance, hence its use throughout this text.

1.1.2 Efficiency

The thrust efficiency is a measure of the fraction of input power that is converted into useful thrust. For an electrothermal thruster, the efficiency can be written as,

$$\eta = \frac{I_{SP_{HOT}}^2}{I_{SP_{COLD}}^2 + \dfrac{2P}{g^2\dot{m}}} \tag{1.4}$$

where the subscripts on I_{SP} refer to whether or not power is applied. In the limit $P \to 0$, the efficiency in Eq. 1.4 goes to unity, as it should. Typically, devices such as dc arcjets have sufficiently high specific energies ($P/\dot{m}$) that the cold flow I_{SP} can be neglected, and the expression for thrust efficiency reduces to,

$$\eta = \frac{T_{HR}\, U_{EQ}}{2P} \tag{1.5}$$

In the low power limit, $\eta \to \infty$ in Eq. 1.5, and this simplified expression should be used only when the cold flow specific impulse can be neglected relative to

the input power term in the denominator. For the pulsed arcjet, the experimental values of $P/\dot{m}$ range from 3 to 11 MJ/kg, and the cold flow specific impulse is not negligible. Therefore, the efficiency data presented for the pulsed arcjet experiments are calculated using Eq. 1.4.

1.1.3 Input Power

The amount of available power onboard a spacecraft will most likely affect the selection and design of an electric propulsion system. The propulsion system must compete with other subsystems for a limited supply of stored electrical energy provided by the spacecraft solar arrays and battery subsystems. The different types of electric thruster - electrothermal, electrostatic, and electromagnetic - have a wide range of performance capabilities which depend on their required input power. Large geosynchronous satellites may have several kilowatts of power available for routine orbit adjustments, and a number of different arcjets, ion and Hall thruster systems have been developed for North-South stationkeeping operations at kilowatt power levels.[2, 3, 4] The operating envelope of these devices is being extended to sub-kilowatt levels to meet the needs of smaller spacecraft with a more limited supply of power.[5, 6, 7]

On the low end of the power scale, the 10-watt pulsed plasma thruster (PPT) originally developed in the early 1970's [8, 9, 10, 11] is presently receiving a great deal of research effort due to its high I_{SP} (~1000 seconds) and ability to deliver discrete impulse bits for precise spacecraft attitude adjustment.[12, 13, 14, 15] A comparison of specific impulse and power levels for some benchmark electric thrusters is shown in Fig. 1-1.[7, 11, 16, 17, 18]

1.2 Previous Research

Two devices that are closely related to the pulsed arcjet are the pulsed electrothermal thruster (PET) and the dc arcjet. The origins of the pulsed arcjet come from work performed by R. L. Burton on the PET thruster in the early-mid 1980's.[19, 20, 21] The PET development effort involved liquid water propellant, and one conclusion of the experimental work was that a switch to a gaseous propellant

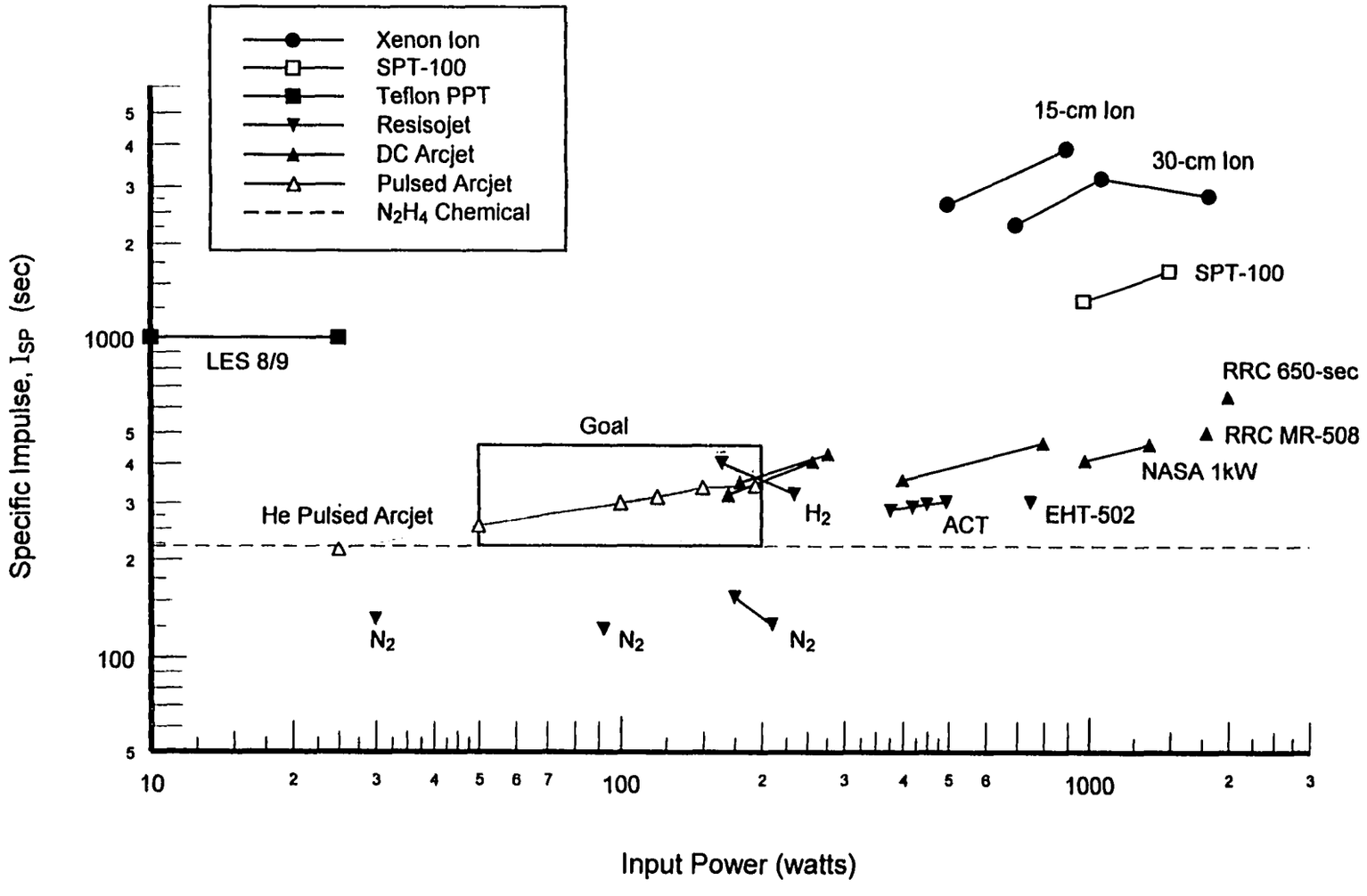

Fig. 1-1. Comparison of input power and specific impulse for selected electric propulsion devices.

might be beneficial. The pulsed arcjet is also related to the dc arcjet, with the major difference being a pulsed versus steady mode of operation.

1.2.1 Pulsed Electrothermal Thruster (PET)

The pulsed electrothermal thruster (PET) has been demonstrated experimentally in laboratory tests by R. L. Burton, et al.[19, 20, 21] This electrothermal device used a pulsed electrical discharge to heat liquid water propellant in a cylindrical capillary, and the high pressure gas was accelerated in a supersonic nozzle. The pulse energies reported for the PET thruster were 40-70 J at pulse repetition rates of 2-10 pps. Average input power was 80-630 watts. Tests involving the PET thruster included thrust stand measurements of the individual impulse "bits" as well as voltage and current measurements of the discharge.

Description		PET	Pulsed Arcjet	Units
Propellant		H_20 (Liquid)	He (Gas)	
Pulse Rate	PPS	2-40	550-2630	[pps]
Pulse Energy	E	40-70	0.02-0.13	[J]
Impulse Bit	I	2800-5400	10-40	[μN-sec]
Pulse Time	τ	16	3-10	[μsec]
Average Power	P_{AVE}	80-630	24-119	[W]
Peak Power	P	3100-6200	10-40	[kW]
Peak Current	I_{PEAK}	3200-4000	110-270	[amps]
Breakdown Voltage	V_B	2100-3000	970-2300	[volts]
PFN Capacitance	C	16	0.05	[μF]
Exhaust Velocity	U_E	12-14	3	[km/s]
Efficiency	η	46-58	34-57	[%]

Table 1-1. Comparison of the water-injected PET thruster with the helium pulsed arcjet. The PET thruster operated at low pulse rates with high pulse energies compared to the high frequency gas-fed pulsed arcjet.

A significant difficulty with the PET thruster was boiling of the liquid at the injection orifice. At low mass flowrates, water surface tension caused droplets to form at the injector tip, and the droplet formation resulted in erratic thruster breakdown. The PET thruster was recommended for application at mean power

levels > 5 kW, since it is easier to achieve steady injection of liquid water at high flowrates. The problem with the liquid propellant feed encountered in the PET thruster led to the consideration of using a gaseous propellant. This evolution of the PET thruster is called a pulsed arcjet, which is the subject of this research.

While the operating concept of the pulsed arcjet is similar to the PET thruster, many of the primary variables are widely different. In short, the PET thruster operated at low frequency with high pulse energies compared to the high frequency pulsed arcjet with low pulse energies. Some of the characteristics of the two devices are shown in Table 1-1. The values for the pulsed arcjet are discussed in detail in subsequent chapters.

1.2.2 Low Power DC Arcjet

The dc arcjet range of operation has been extended to the sub-kilowatt level, though the performance penalties at low power may limit applications of the dc arcjet to power levels above 500 watts. An emphasis in recent years has been to study and improve the performance of 1-2 kW dc arcjets using hydrazine propellant.[4, 22, 23, 24, 25, 26] Hydrazine (N_2H_4) is a storable monopropellant that is widely used in chemical thrusters, and the ability to combine existing hydrazine feed system technology with an arcjet thruster is a significant cost and risk benefit at a systems level. Presently, flight-qualified hydrazine arcjets provide a specific impulse in the 500-600 second range with 30-35% efficiency.[16]

A relatively standard 1-kW thruster has been developed by NASA LeRC with 450-460 seconds specific impulse and 33-38% efficiency. This device has been used frequently for detailed studies of arcjet physics.[27, 28, 29] Arcjets can become difficult to operate as the power level decreases, primarily due to problems with arc stability, though recent experiments with a miniaturized dc arcjet at 300 watts yielded an I_{SP} equal to 370 seconds with 27% efficiency. The conical nozzle used in the miniaturized arcjet had an area ratio equal to 400 and a 15 degree half angle. The large area ratio nozzle was believed to have large viscous losses, and an experimental study with various nozzle designs increased the performance at 250 watts to 370-440 seconds with 25-36% efficiency.[7]

Helium propellant is sometimes considered for electric thrusters due to its low molecular weight and high frozen flow efficiency. The primary disadvantage of using helium as a spacecraft propellant is the problem of long term storage of cryogens in space. However, tankage fractions below 10% may be possible, making helium a viable choice of propellant.[30] Because of these system issues, little work has been done on helium propellant arcjets, although recently the NASA 1-kW laboratory arcjet has been operated with helium at approximately 500-700 watts input power.[30] Typical specific impulses are 450-550 seconds. Helium dc arcjet operation has been observed to be unstable on time scales of seconds to minutes, and these recent experiments investigated the effects of hydrogen seeding on arcjet stability.[30]

1.3 Thesis Overview and Objectives

The present trends for both commercial and government satellite programs are toward smaller spacecraft in order to reduce launch costs and decrease risks associated with single large satellites. A large number of commercial communications satellites are planned for launch to low-to-medium orbits over the next decade, and these multi-satellite constellations consist of relatively small spacecraft of less than 500 kg, compared to 2500-3500 kg for typical geostationary satellites.[31] At this size, the available power will most likely be less than the several kilowatts available on a geostationary satellite, limiting the number of options for the propulsion system.

The actual power levels in this research were 24 to 119 watts, which is a range between the 10-watt PPT and the low power dc arcjet. At sub-kilowatt power levels, the present alternative to traditional chemical propulsion is the hydrazine resistojet, with specific impulses greater than 293 seconds (303 seconds for the EHT-502)[16] and 78% efficiency.[17] The hydrazine resistojet therefore sets the benchmark performance against which the pulsed arcjet may be compared, and the pulsed arcjet should have at least this level of specific impulse to warrant further consideration. The experimental performance obtained in the laboratory for the pulsed arcjet is 305 seconds I_{SP} and 38% efficiency. Numerical results indicate that

400+ seconds I_{SP} and 60+ % efficiencies are possible with an improved thermal design.

1.3.1 Experimental Approach

The experimental part of this research focused on four objectives: 1) to demonstrate the operation of the thruster, 2) to measure the overall pulsed arcjet performance in terms of specific impulse and efficiency over a range of operating conditions and different arcjet geometries; 3) to determine the individual energy loss mechanisms in the pulsed arcjet system, including the thruster and the external circuit; and 4) to evaluate the characteristics of the arc discharge from measurements of arc current and voltage. These experiments were intended to provide sufficient data for a basic understanding of the physics of the pulsed arcjet, and to identify specific areas for future work.

Preliminary experiments with the pulsed arcjet were conducted using simulated-hydrazine propellant; however, the performance did not appear promising, and the range of test conditions was restricted by the unfavorable breakdown characteristics of the propellant. Switching to helium propellant reduced or eliminated many of the initial problems, allowing clear performance trends to be obtained experimentally. In order to make the presentation of the results as clear as possible, only the helium results are included in the body of this paper. Selected results for simulated-hydrazine are included in Appendix A.

1.3.2 Numerical Methods

Measurements of thruster performance tend to provide overall results that are needed to assess the usefulness of the device, but global performance measurements are lacking in detail regarding the specific energy loss mechanisms. The primary goal of the numerical work was to develop a pulsed arcjet performance code that would predict the specific impulse and efficiency for a given arcjet geometry and operating condition. The numerical model was intended to complement the experiments and to provide detail on energy losses which could be used to assess approaches for improving the performance. A secondary objective

was to study the behavior of the capillary arc discharge and voltage breakdown with simple models which could be used to evaluate experimental data.

References

[1] Jahn, R. G., *Physics of Electric Propulsion*, McGraw_Hill, New York, 1968.

[2] Sankovic, J. M., Hamley, J. A., Haag, T. W., "Performance Evaluation of the Russian SPT-100 Thruster at NASA LeRC," IEPC Paper 93-094, 1993.

[3] Patterson, M. J., and Haag, T. W., "Performance of the NASA 30 cm Ion Thruster," IEPC Paper 93-108, 1993.

[4] Lichon, P., and Sankovic, J., "Development and Demonstration of a 600 Second Mission Average I_{SP} Arcjet," *Journal of Propulsion and Power*, Vol. 12, No. 6, pp. 1018-1025, 1996.

[5] Brophy, J. R., Mueller, J., and Anderson, J. R., "Operating Characteristics of a 15-cm-dia. Ion Engine for Small Planetary Spacecraft," IEPC Paper 93-110, 1993.

[6] Sankovic, J. M., and Jacobson, D. T., "Performance of a Miniaturized Arcjet," AIAA Paper 95-2822, 1995.

[7] Sankovic, J., and Hopkins, J., "Miniaturized Arcjet Performance Improvement," AIAA Paper 96-2962, 1996.

[8] Guman, W. J., and Nathanson, D. M., "Pulsed Plasma Microthruster Propulsion System for Synchronous Orbit Satellite," *Journal of Spacecraft and Rockets*, Vol. 7, No. 4, pp. 409-415, 1970.

[9] Vondra, R. J., "Flight Qualified Pulsed Electric Thruster," *Journal of Spacecraft and Rockets*, Vol. 11, No. 9, Sept 1972.

[10] Vondra, R. J., "Flight Qualified Pulsed Electric Thruster for Satellite Control," AIAA Paper 73-1067, 1973.

[11] Vondra, R. J., and Thomassen, K. I., "Flight Qualified Pulsed Electric Thruster for Satellite Control," *Journal of Spacecraft and Rockets*, Vol. 11, No. 9, pp. 613-617, 1974.

[12] Meckel, N. J., Hoskins, W. A, Cassady, R. J., Myers, R. M., Oleson, S. R., and McGuire, M. L, "Improved Pulsed Plasma Thruster Systems for Satellite Propulsion," AIAA Paper 96-2735, 1996.

[13] Kamhawi, H., Turchi, P. J., Leiweke, R. J., and Myers, R. M., "Design and Operation of a Laboratory Benchmark PPT," AIAA Paper 96-2732, 1996.

[14] Tilley, D. L., and Spores, R. A., "Life Extension Strategies for Space Shuttle-Deployed Small Satellites Using a Pulsed Plasma Thruster," AIAA Paper 96-2730, 1996.

[15] Spanjers, G. G., McFall, K. A., Gulczinski, F. S., and Spores, R. A., "Investigation of Propellant Inefficiencies in a Pulsed Plasma Thruster," AIAA Paper 96-2723, 1996.

[16] Butler, G. W., and Cassady, R. J., "Directions for Arcjet Technology Development," *Journal of Propulsion and Power*," Vol. 12, No. 6, pp. 1026-1034, 1996.

[17] McKevitt, F. X., "Design and Development Approach for the Augmented Catalytic Thruster," AIAA Paper 83-1255, 1983.

[18] Morren, W. E., Whalen, M. V., Sovey, J. S., "Performance and Endurance Tests of a Laboratory Model Multipropellant Resistojet," *Journal of Propulsion and Power*, Vol. 6, No. 1, pp. 18-27, 1990.

[19] Burton, R. L., et al., U.S. Patent Application No. 743,150, Pulsed Electrothermal Thruster, June 20, 1985.

[20] Burton, R. L., Fleischer, D., Goldstein, S. A., and Tidman, D. A., "Experiments on a Repetitively Pulsed Electrothermal Thruster," *Journal of Propulsion and Power*, Vol. 6, No. 2, pp. 139-144, 1990.

[21] Burton, R. L., Hilko, B. K., Witherspoon, F. D., and Jaafari, G., "Energy-Mass Coupling in High-Pressure Liquid-Injected Arcs," *IEEE Transactions on Plasma Science*, Vol. 19, No. 2, 1991.

[22] Curran, F. M., and Sarmiento, C. J., "Low Power Arcjet Performance," AIAA Paper 90-2578, 1990, (also NASA TM 103280, 1990).

[23] Deininger, W. D., Pivirotto, T. J., and Brophy, J. R., "Effect of Nozzle and Cathode Configuration on Arcjet Performance," *Journal of Propulsion and Power*, Vol. 6, No. 3, pp. 271-275, 1990.

[24] Curran, F. M., Sarmiento, C. J., Birkner, B. W, and Kwasny, J., "Arcjet Nozzle Area Ratio Effects," NASA TM 104477, 1990.

[25] Curran, F. M., Sovie, A. J., and Haag, T. W., "Arcjet Nozzle Design Impacts," NASA TM 102050, 1989.

[26] Brophy, J. R., Pivirotto, T. J., and King, D. Q., "Investigation of Arcjet Nozzle Performance," AIAA Paper 85-2016, 1985.

[27] Burton, R. L., and Bufton, S. A., "Exit-Plane Electrostatic Probe Measurements of a Low-Power Arcjet," *Journal of Propulsion and Power*, Vol. 12, No. 6, pp. 1099-1106, 1996.

[28] Tiliakos, N. T., and Burton, R. L., "Arcjet Anode Sheath Voltage Measurement by Langmuir Probe," *Journal of Propulsion and Power*, Vol. 12, No. 6, pp. 1174-1176, 1996.

[29] Cappelli, M. A., and Storm, P. V., "Interior Plasma Diagnostics of Arcjet Thrusters," *Journal of Propulsion and Power*, Vol. 12, No. 6, pp. 1070-1076, 1996.

[30] Welle, R. P., "Space Propulsion Applications of Helium Arcjets," AIAA Paper 97-0794, 1997.

[31] Ropelewski, R., "Satellite Services Soar," *Aerospace America*, Nov. 1996.

2. *Experimental Apparatus*

2.1 General Description of Pulsed Arcjet Operation

As electrothermal devices, arcjets use electrical energy to heat a propellant, and the resulting high enthalpy gas is exhausted through a nozzle to produce thrust. In other words, stored electrical energy is converted into random thermal energy of the propellant by ohmic heating in an arc discharge. Then the random thermal energy is converted into directed kinetic energy in a converging-diverging nozzle expansion process. In the conventional dc arcjet, electrical current emitted from the cathode is pushed through the nozzle constrictor (throat) region by gas dynamic forces, and the arc attaches diffusely in the supersonic region of the nozzle (anode). The arc current, voltage and input power are essentially constant in a dc arcjet. For example, the NASA 1-kW dc arcjet operates with a nominal current of 10 amps and an arc voltage of 100 volts.[1]

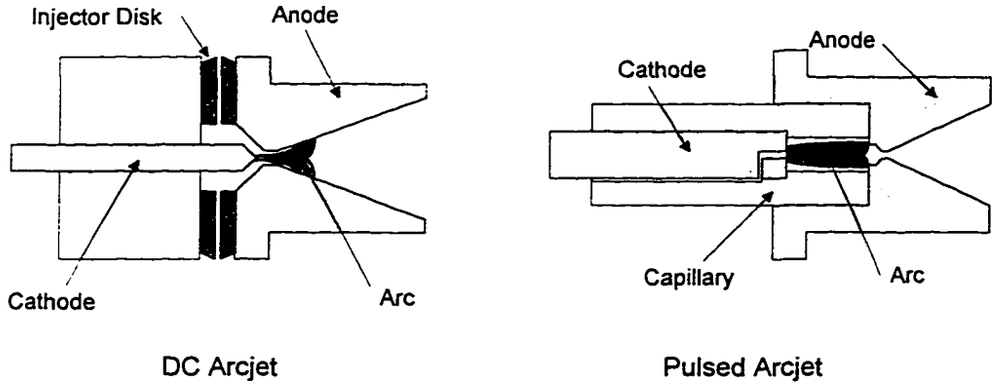

Fig. 2-1. Comparison of electrode geometry and arc attachment regions for a DC arcjet and a pulsed arcjet. The pulsed arcjet employs subsonic heat addition.

In the pulsed arcjet investigated here, energy is transferred to the propellant in short intense bursts rather than continuously. The arc is present only for short time periods, approximately 3-10 μsec, but the discharges occur at repetition rates of several thousand pulses-per-second (pps). The arc discharges are produced using a constant current power supply, a storage capacitor, and a pulse-forming electrical circuit. The power supply ramps up the voltage and stored energy on the capacitor

until the breakdown voltage of the propellant between the electrodes is reached. At the breakdown voltage, an arc discharge initiates in a cylindrical capillary between the electrodes, and the energy stored on the capacitor is transferred to the propellant gas in a short intense pulse. The arc completely extinguishes when the voltage on the capacitors is not sufficient to maintain the arc, and the charging cycle repeats. Utilizing the self-breakdown of the propellant eliminates the need for a switch or spark igniter, greatly simplifying the electrical circuit. The time between pulses is on the order of 10^{-3} seconds, which is much longer than the arc discharge time of 10^{-6} to 10^{-5} seconds so that the arc is present for only a small fraction of the total cycle time. Arc peak currents are several hundred amps, and arc voltages are typically 100 to 200 volts. Pulse energies are 20 to 130 mJ.

In the dc arcjet, energy addition to the propellant occurs in both the subsonic and supersonic flow regions. In the pulsed arcjet investigated here, the arc attachment occurs upstream of the nozzle convergent section, and the heat addition to the gas is entirely subsonic. Though the pulsed arcjet could potentially be developed to employ heat addition in the supersonic flow region, only subsonic heat addition is investigated here.

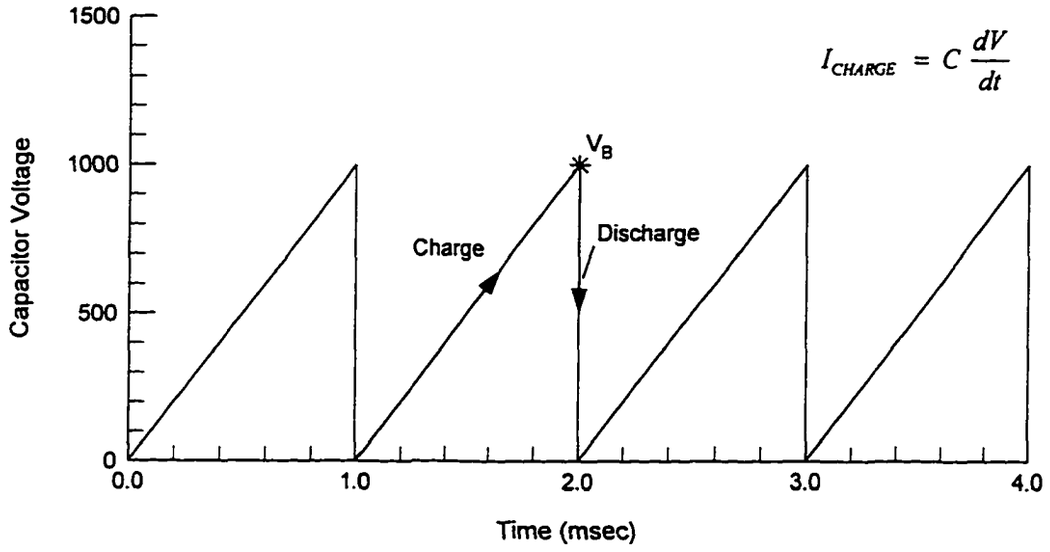

Fig. 2-2. Schematic of the capacitor voltage for a series of pulses at 1000 pps. The voltage has a linear ramp rate when the charge current is constant.

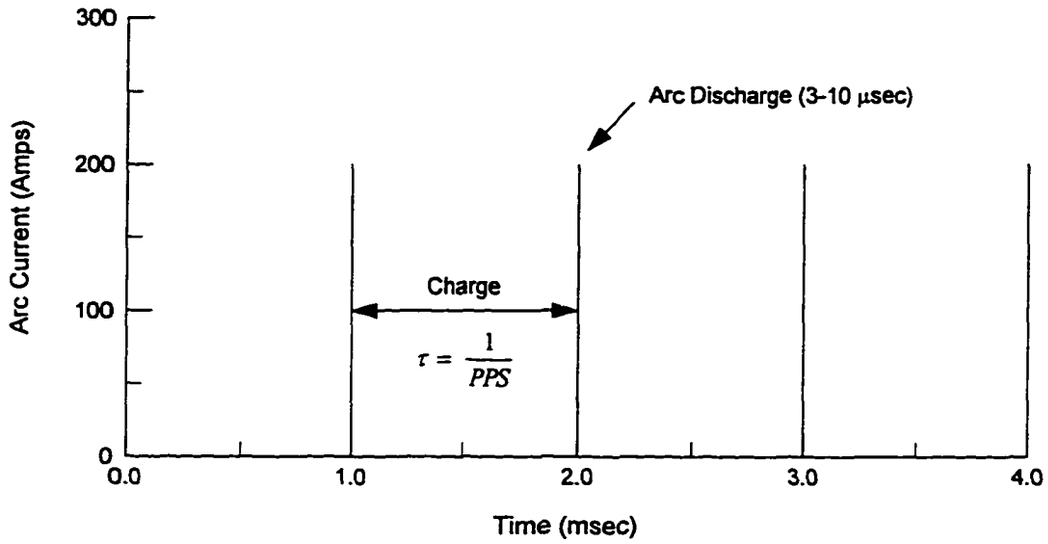

Fig. 2-3. Schematic of the arc discharge current for a series of pulses at 1000 pps. The arc is present for only a small percentage of the total cycle time.

2.2 Thruster Design

The pulsed arcjet assembly consists of the thruster itself and the pulse-forming electrical circuit including the storage capacitor. The arcjet mechanical/thermal design is based on a NASA 1-kW laboratory-type arcjet with modifications to the thruster head for pulsed operation (Fig. 2-4). The pulse-forming electrical circuit was designed to provide a unipolar pulse to benefit capacitor life and to minimize energy losses in the external circuit.

2.2.1 Mechanical Design

The design of the thruster head is modified from the NASA 1-kW design to include a cylindrical insulator tube between the cathode and the anode (nozzle). This cylindrical tube is called a capillary and is analogous to a combustion chamber in a chemical rocket. The cathode consists of 3 pieces: a 4.76 mm diameter, 2%-thoriated tungsten front section, a 4.76 mm diameter brass rear section, and a stainless steel connector. The front cathode section is spring-loaded against the boron nitride capillary tube with approximately 90 N [20 lb.] force to seal both ends of the capillary against internal leakage. The connection between the rear cathode

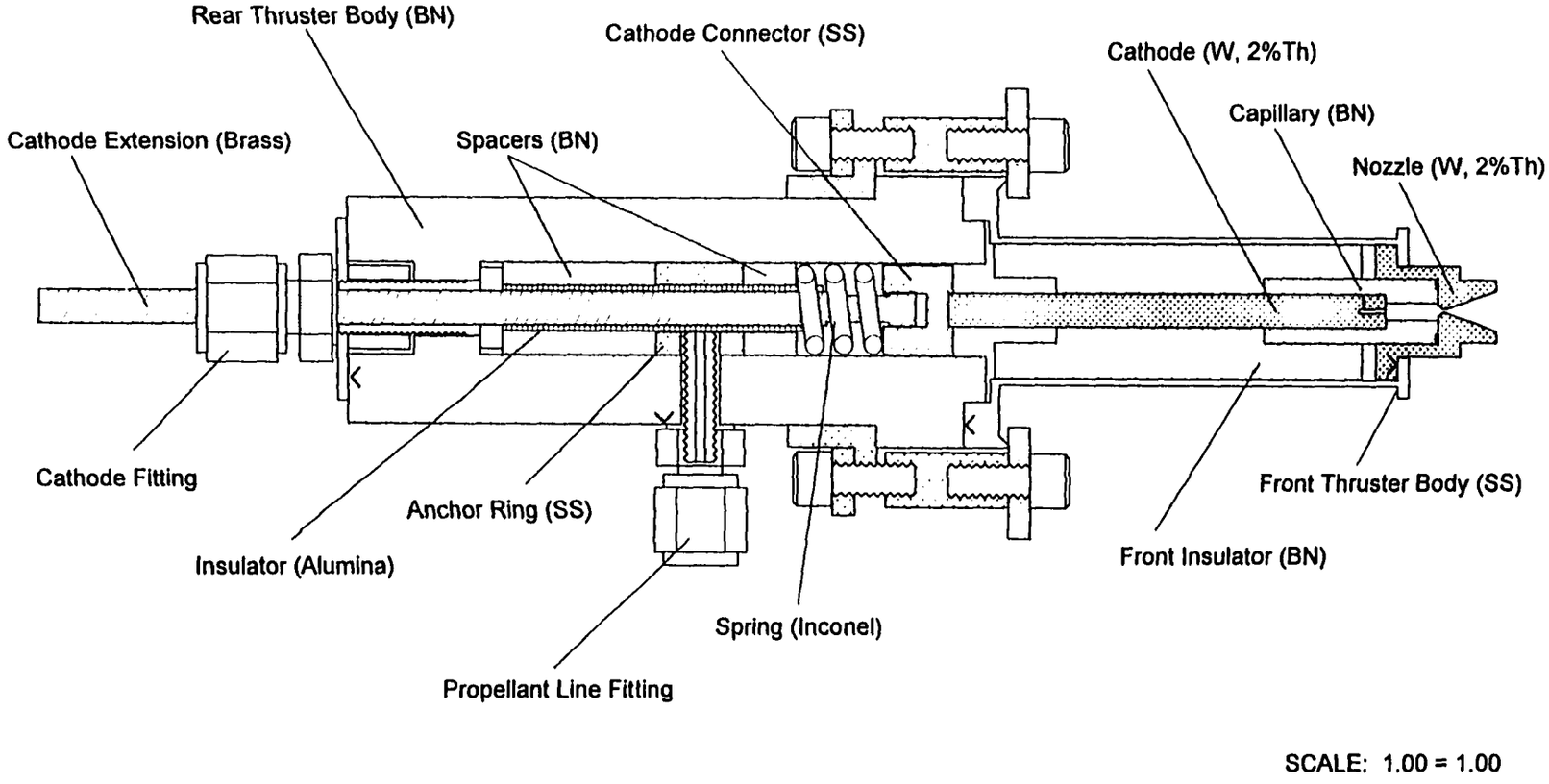

Fig. 2-4. Assembly drawing of pulsed arcjet thruster.

section and the stainless steel connector is a friction fit. The anode is a 20-degree half-angle conical nozzle fabricated from 2% thoriated tungsten. The nozzle throat was machined using an EDM process to 0.38 mm diameter, measured from a photomicrograph.

The arcjet design allows testing with different nozzle and capillary geometries and values of capacitance as shown in Table 2-1. The 20-degree nozzle half-angle was selected because a number of cold gas and dc arcjet studies have shown that this value is near the optimum for these devices.[2, 3, 4] Two different nozzles with area ratios of 20 and 230 were fabricated to evaluate the tradeoff between the additional gas expansion at higher area ratio compared to viscous losses. Friction effects are significant because the Reynolds numbers in the pulsed arcjet are relatively low, ~1000. The capillary lengths were selected so that electrical breakdown would occur at voltages from 1000 to 2000 volts for the desired range of mass flow rates. The 2.5 mm capillary diameter was selected as a baseline geometry from volume considerations. The capacitor was sized for the desired pulse energies, power levels and peak temperatures.

Nozzle	
α (deg)	A/A*
20	20
20	230

Capillary	
L (mm)	D (mm)
7.5	1.5
7.5	2.5
12.5	1.5
12.5	2.5
12.5	3.5

Capacitors
(μF)
0.05
0.10

Table 2-1. Nozzle, capillary and capacitor values used in pulsed arcjet tests. The two nozzles are used to compare viscous effects; two capacitances are used to examine the effect of pulse energy; five capillaries are tested to evaluate subsonic heat transfer.

Propellant gas is fed to the thruster through a tube fitting on the side of the rear insulator. The propellant flow is continuous and is not pulsed with a propellant valve. The gas flows through grooves in the front insulator and is then injected axially into the capillary through a 0.28 mm diameter orifice in the cathode. The size of the orifice is smaller than the 0.38 mm nozzle throat diameter in order

to limit the amount of gas that is blown back upstream after each arc discharge. The four mechanical joints use graphite foil seals to prevent leakage.

During the pulsed arcjet tests, the 0.38 mm diameter throat was found to be susceptible to blockage by foreign particles. At high pulse energies corresponding to high peak temperatures, small particles assumed to be pieces of boron nitride would become lodged in the nozzle throat. The decreased throat area would consequently cause the gas pressure and number density in the capillary to increase such that the breakdown voltage, pulse energy, and peak temperature also increased. Within a few seconds, the nozzle would become nearly or completely blocked so that the gas number density in the capillary was too high for voltage breakdown. At that point, the power supply simply held the voltage at its programmed limit. The arcjet was most susceptible to this failure mode at low flow rates and high peak temperatures, which was typical of tests with simulated-hydrazine.

2.2.2 Thermal Design

The pulsed arcjet is a thermal device, and the surface temperatures of the nozzle and front thruster body have an important effect on overall performance. Heat loss from the propellant gas to the wall surfaces is removed from the thruster head by radiation to the external environment and conduction to the rear of the thruster. Typically, the NASA 1-kW dc arcjet operates with a steady state surface temperature of approximately 1160-1320 K.[5] For the pulsed arcjet running on less than 150 watts in a 1-kW arcjet body, the steady state operating temperature with the original thermal design would be relatively low with correspondingly poor performance. The original thermal design indeed proved to be cold in preliminary tests and was improved by reducing the wall thickness of the front thruster body from 6.35 mm to 0.8 mm to reduce heat conduction to the rear of the thruster. This modification allowed the thruster to operate with nozzle temperatures up to 800 K, though this was still much less than desired for optimal thruster performance.

Limits on the maximum operating temperature of the pulsed arcjet include the maximum temperature of the capillary material and its dielectric strength at high temperature. Though the temperature of the boron nitride capillary was not measured directly, it can be assumed that the capillary temperature was equal to or

greater than the nozzle temperature. The nozzle material was chosen as 2%-thoriated tungsten for considerations of arc attachment rather than the steady state bulk temperature, which was well below the material melting temperature.

	Material	*Mass*	*Operating Temp*	*Maximum Temp*
Capillary	Boron Nitride (grade AX05)	2.6 g	Not measured	1120 K
Nozzle	2% Thoriated Tungsten	32 g	800 K	3680 K

Table 2-2. Nozzle and capillary material, component mass, and maximum temperature.

2.2.3 Electrical design

The shape of each current pulse, the peak current, and the duration of the arc are determined by the characteristics of the arc resistance and the design of the external electrical circuit. The external circuit design determines how much energy is transferred to the propellant gas compared to energy lost in the external circuit components. The circuit design is shown in Fig. 2-5, and includes a single storage capacitor, a pair of high voltage, high current diodes, and an inductor.

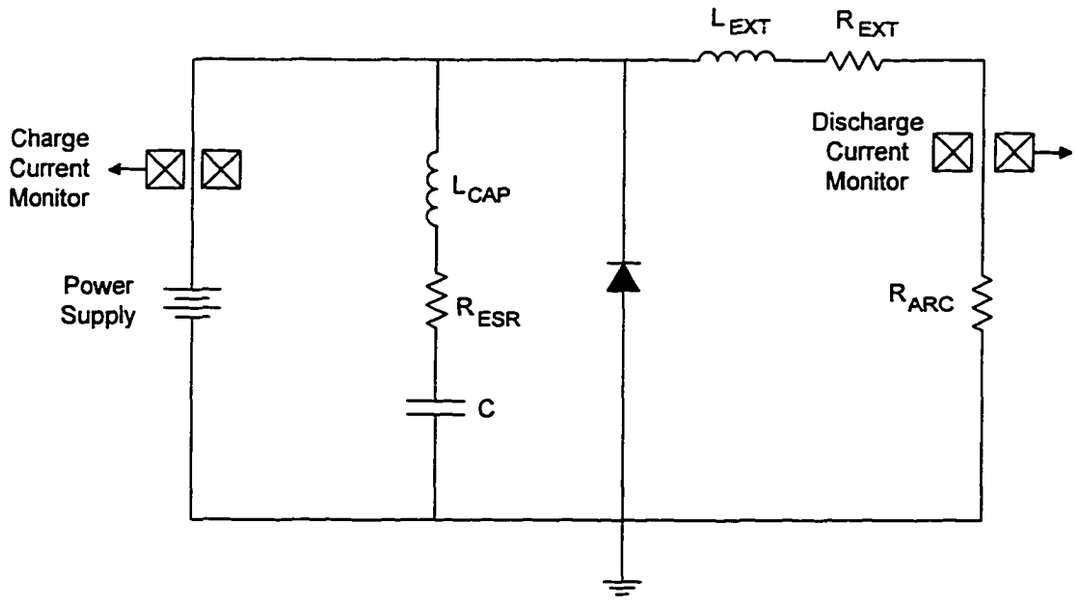

Fig. 2-5. Electrical diagram of the pulse-forming electrical circuit.

The value of the capacitance establishes the pulse energy and indirectly sets the gas peak temperature and pressure. The inductor sets the magnitude of the

peak current and the time duration of the arc. The diodes are used to eliminate oscillations in the discharge current that would occur if the circuit were simply an underdamped LCR circuit. The arc current is measured using a 0.1 volt/amp inductive current monitor, and this data is used to analyze the circuit efficiency in Chapter 5.

The capacitors used in this research are General Electric SCR commutation capacitors with an all-film dielectric. Two sizes are used: 0.05 μF (GE series 97F8581) and 0.10 μF (GE series 97F8610) with a maximum voltage rating of 2500 volts and a maximum dissipation factor, DF, less than 0.0002. For these capacitors, the dissipation factor is approximately constant over the range of 1 kHz to 10 kHz.[6]

The total circuit inductance is the sum of the self inductance of the individual elements plus the sum of the mutual inductance of each pair of elements. The inductance of the thruster without the fixed inductor is measured to be 330 nH (see Appendix B-4). The circuit inductance is increased to 2.90 μH using two Brooks coils[7] in series arranged as two opposing dipoles. Except for the inductor, the physical current path is designed in a coaxial configuration. The coaxial design is mainly employed to reduce the magnetic field outside the thruster, which could produce electrical noise in the thrust stand wiring. The magnetic field along the axis or at a large distance from a dipole decays as $1/r^3$, whereas for the two opposing dipoles, the magnetic field decays approximately as $1/r^4$.

The diodes are high current devices with a maximum reverse voltage rating of 3600 volts and a maximum forward voltage drop of 3 volts.[8] Two diodes are used in parallel and are connected to copper heat sinks to dissipate heat. The diodes are cooled by heat conduction through the 1.3 mm diameter leads. A thermocouple is mounted on one of the diodes using Omegabond™ 101 epoxy to monitor diode temperature during arcjet operation. Finally, the diodes are connected as close to the capacitor terminals as possible in order to minimize the inductance associated with the capacitor side of the circuit.

2.3 Propellant Flow Control

The helium propellant is supplied at room temperature from a high pressure gas cylinder with 99.995 % purity. The propellant flow control system is shown in

Fig. 2-6. The propellant flows through a regulator valve to a Unit Instruments model UFC-1500A (5 slm) flow controller. The Unit Instruments model URS-100-5 control unit provides a 0-5 volt analog signal to the data acquisition system during performance tests for continuous monitoring of the propellant flow rate. The flow controller is calibrated to an accuracy of better than 2.2% using a control volume method (see Appendix B-1). Calibration was performed periodically, and the calibration factor was found to vary less than 1.6% between tests. The total uncertainty in the mass flow is taken to be $\sqrt{(0.022^2+0.016^2)} = 2.7\%$.

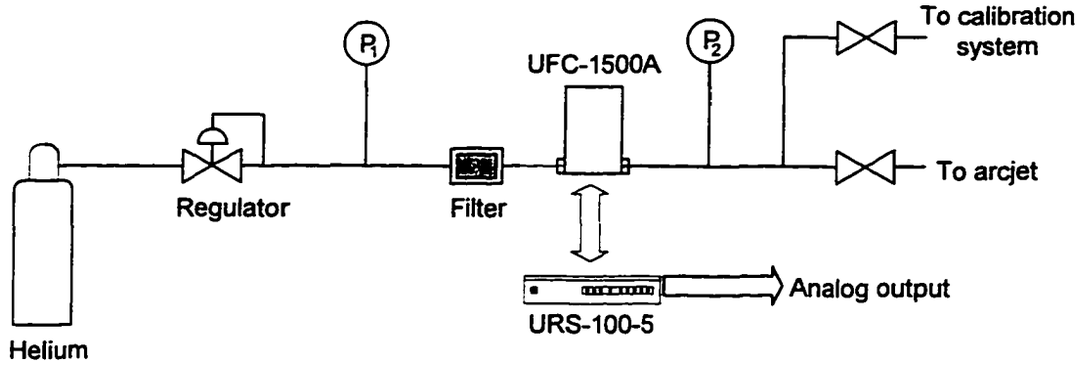

Fig. 2-6. Schematic of propellant supply and flow control.

2.4 Performance Measurements

The arcjet thruster is operated in a 1.0 m diameter x 1.5 m long vacuum tank. Vacuum conditions are created by a 2500 cfm Roots-type blower backed by a 1300 cfm Roots blower and two 150 cfm mechanical displacement pumps. With zero propellant flow rate, the vacuum system is capable of being evacuated to less than 1 mTorr. At typical propellant flow rates, the background pressure in the vacuum tank is approximately 50 mTorr. Power is supplied through a high voltage coaxial power cable by a Converter Power Model RCS 3000 power supply operating outside the vacuum tank. Inside the vacuum tank, the power line is an RG/U 188 coaxial cable looped to minimize drag on the thrust stand.

2.4.1 Thrust Stand Mechanical Description

The thrust stand is an inverted pendulum-type similar to the instrument used at the NASA Lewis Research Center.[1] The thruster assembly is mounted on a

support plate which is free to move translationally over a short range with negligible friction. The force required to move the thruster is proportional to distance based on the spring constant of the mechanical system. The displacement is measured with a 1.6 volt/mm Lucas Instruments model 100-HR linear variable differential transformer (LVDT) sensor and a Schaevitz DTR-451 digital transducer readout. Because the mechanical design is nearly frictionless, the thrust stand would oscillate indefinitely following any applied force. A magnetic damper coil is used to remove oscillations so that the steady state thrust can be measured. Since the arcjet pulse rate is two orders of magnitude greater than the thrust stand natural frequency, the output signal appears as a steady time-averaged thrust, and the individual impulse bits are not observed in the thrust measurement. Thrust calibration is performed before and after each test with a pulley arrangement providing three known force levels. Details of the thrust calibration technique are described in Appendix B-2. The repeatability of the thrust calibration method was found to be approximately 0.8%.

2.4.2 Thrust Stand PID Control Unit

The thrust levels produced by the pulsed arcjet at 24 to 119 watts are typically in the range of 10-30 mN. In order to achieve a sufficient signal from the LVDT, the spring constant of the mechanical system must be relatively low. However, with a low spring constant, the thrust stand will not balance its own weight and becomes unstable. A proportional-integral-derivative (PID) control unit was used for feedback control of the thrust stand. The PID controller was adapted for the pulsed arcjet tests from a circuit initially built under a NASA contract, "10 kW Laser Propulsion Thruster Test Program."[9] The original circuit was modified for a different magnetic damper coil and revised control gains.

With PID feedback control, instead of measuring a linear displacement from an initial position, the thrust stand is held at its initial location, x_{SET}, by the counterforce/damper coil. The electrical current through the coil required to hold this position is measured, and thrust is proportional to the steady-state current applied to the coil. The proportional and integral stages of the control unit are used to maintain the thruster position at the LVDT zero setting while the derivative

stage magnetically dampens thrust stand oscillations. Using the analog signal from the Schaevitz transducer readout as its input, the PID controller sets its output voltage according to,

$$V_{OUT} = g_1 \left[g_2(x - x_{SET}) + g_3 \int (x - x_{SET})\, dt + g_4 \frac{dx}{dt} \right] \quad (1.1)$$

where the g_i are the control gains in the system, and (x - x_{SET}) is the linear displacement of the thrust stand from its initial setpoint. A power amplifier is used to buffer the PID controller output and provide sufficient electrical current to the coil. A classical control theory analysis using Routh-Hurwitz stability criterion was required to set the gains so that the system was stable.

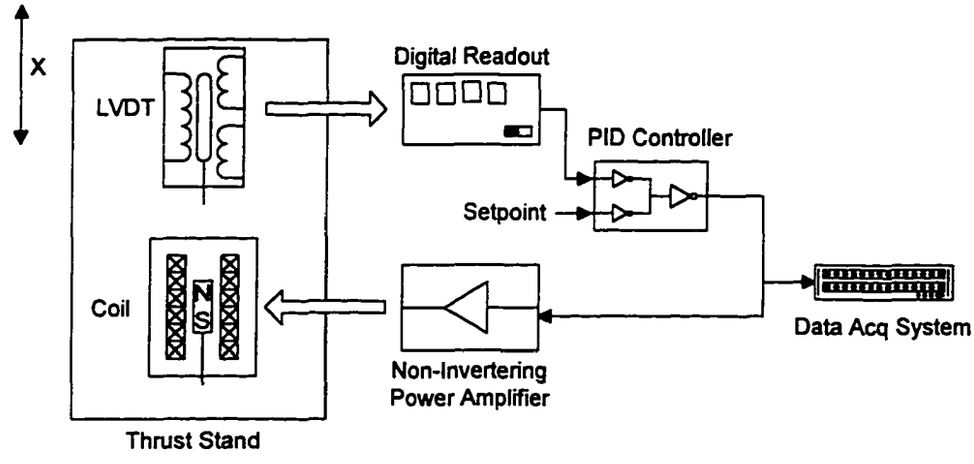

Fig. 2-7. Block diagram of thrust stand control and measurement system. The proportional-integral-derivative circuit provides feedback control.

With the feedback control loop, the current through the coil is continuously adjusted at a frequency of 100-200 Hz. These current adjustments together with vibrations from the vacuum pumping system limited the thrust stand sensitivity. The measurement variations for steady state cold flow are shown in Fig. 2-8 for 1.4 mN and 15.9 mN thrust levels. Thrust measurement data are taken for 12 thrust levels up to 29 mN with each thrust level measured over a period of 50 seconds. A total of 100 samples are recorded at 0.5 second intervals for each thrust level. The standard deviation, maximum and minimum are calculated from each set of 100

samples. The error increases rapidly below 4 mN as shown in Fig. 2-8. Since most of the thrust measurements are obtained above 10 mN, the maximum uncertainty due to the thrust stand vibrations is taken to be 1.0%.

Two additional uncertainties in the thrust data are thruster alignment and thrust stand hysterisis. The alignment of the thruster is done visually and is assumed to be parallel to the thrust stand axis within 5 degrees, or a maximum 0.4% error in the thrust. Hysterisis is checked during each performance test. After completion of a 10-15 minute test to thermal steady state, the power and propellant flow are turned off, and the thrust offset from the initial zero is recorded. The maximum offset from the initial zero was 14% of the steady thrust; however, it was found that the offset could be subtracted from the data by assuming that the hysterisis drift occurred linearly with time. A maximum hysterisis error of 0.2 mN was retained. The total uncertainty in the thrust data includes the calibration repeatability (0.8%), thrust stand vibration (1.0%), alignment (0.4%) and hysterisis (1.3%). Taking the root mean square value of these four values gives a total uncertainty of 1.9%.

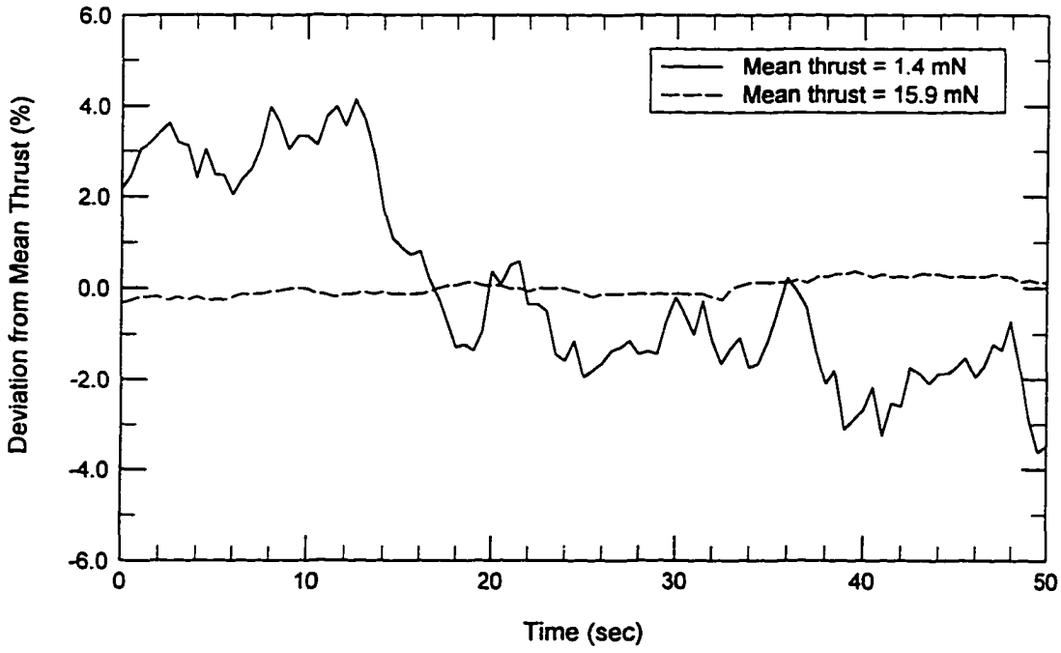

Fig. 2-8. Variation in the thrust measurement at thrust levels of 1.4 and 15.9 mN.

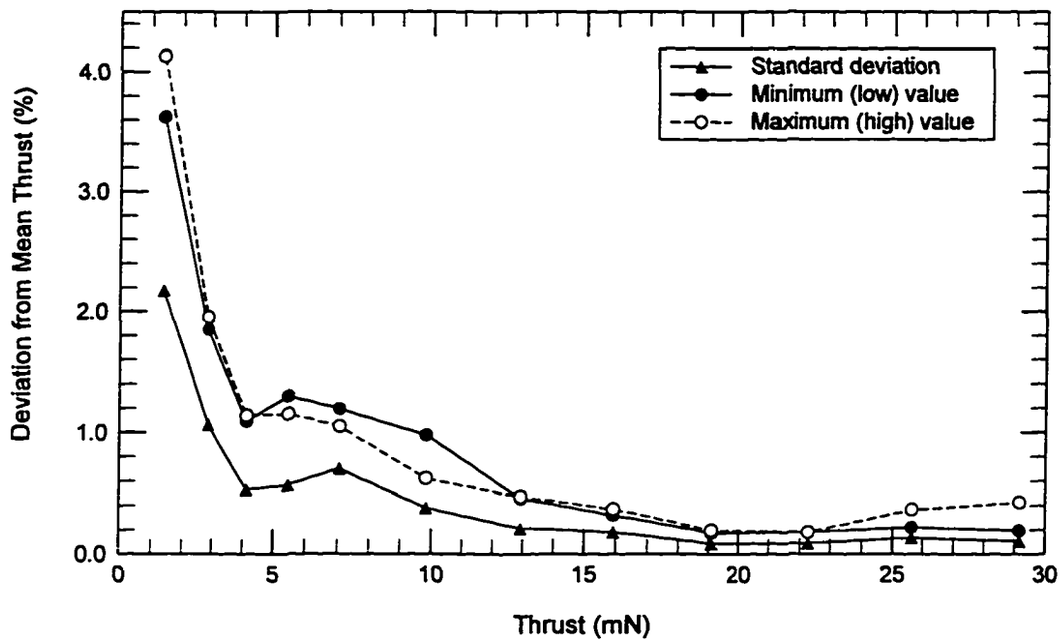

Fig. 2-9. Deviations in thrust for an experiment with room temperature helium. Thrust is recorded at 2 samples-per-second. Measurement errors increase rapidly below 4 mN.

2.4.3 Thermocouple Measurements

Type K thermocouples were installed on the pulsed arcjet to measure temperatures of the diode, the capacitor, and the nozzle. Temperatures were recorded manually by observing a Fluke 52 K/J digital thermometer and an Omega model DP462 digital readout. The diode thermocouple was installed as a health monitoring measurement rather than a diagnostic, and the arcjet was turned off when the diode temperature exceeded 100 C. This situation occurred for the two performance tests where the steady state power was greater than 100 watts. The diode temperature generally increased linearly throughout the test without any indication of a steady state temperature being approached. The diode temperature ramp rate was approximately constant from test to test at 0.024 deg C / min / watt.

The capacitor temperature was recorded to allow a rough calculation of the power loss in the capacitor based on an assumed heat capacity, mC_P, of 200 J/deg C. The temperature ramp rate of the 0.05 μF capacitor was approximately 0.010 deg C

/ min / watt. The energy loss in the capacitor derived from the temperature measurement is estimated to be,

$$\eta = \frac{Q_{CAP}}{P} = \frac{(mC_P)_{CAP}\,(0.010P)}{P} = 3.3\% \qquad (1.2)$$

This calculation assumes no heat conduction or radiation heat loss from the capacitor. The value of 3.3% is less than the 5.8% value discussed in Chapter 5, though the agreement is relatively good considering the uncertainty in the value used for the capacitor heat capacity.

The nozzle temperature was used to determine the time to thermal steady state as well as to provide the wall temperature boundary condition used in the numerical model. Unfortunately, the single thermocouple did not provide enough information for an evaluation of the thruster thermal efficiency because the uncertainties in calculating heat conduction to the thruster rear were relatively high. The nozzle thermocouple was a bare junction type installed using a high temperature zirconia adhesive. A thin layer of adhesive was applied between the thermocouple and the nozzle to electrically insulate the two surfaces. In initial tests, the thermocouple was electrically grounded to the anode, but the discharge current introduced more electrical noise than the thermocouple readout was able to filter. A disadvantage of the zirconia adhesive was the uncertainty in the temperature measurement introduced because the thermocouple was not in direct thermal contact with the nozzle surface.

2.5 Data Acquisition and Power Control

Two separate data acquisition systems are used in the experiments: a 10 MHz system for measurements related to individual pulses on μsec time scales, and a lower speed system for recording arcjet performance parameters on a time scale of seconds to minutes. This section also describes conditioning of the pulse rate and breakdown voltage signals as well as control of the arcjet power supply.

2.5.1 High Speed Data Acquisition System

For detailed measurements related to individual arc pulses or charging cycles, a 4-channel, 8-bit, 10 MHz Soltec digital oscilloscope is used. Two Pearson

inductive current monitors (Models 411 and 4100) are used to measure the capacitor charging current and the arc discharge current. The capacitor charging voltage is measured using a low level 0-10 volt analog signal from the power supply. The Soltec oscilloscope was also used to obtain several photodiode and single probe measurements in the arcjet plume. The data is recorded at the maximum 10 MHz sample rate, giving a time resolution of 100 nsec.

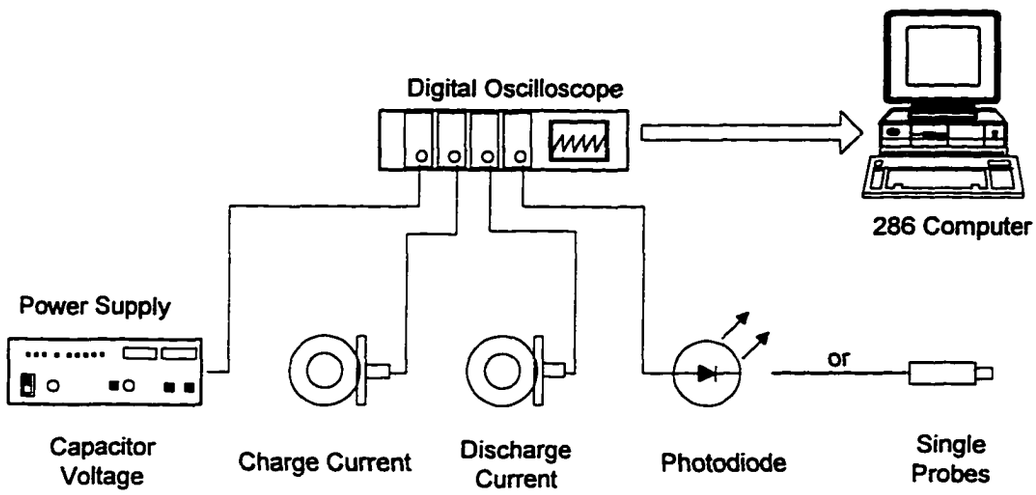

Fig. 2-10. High sample rate (10 MHz) data acquisition system.

A few optical emission measurements were made using a Motorola MRD500 photodiode. The external metal surfaces of the photodiode were insulated with silicone RTV so that the photodiode would not also act as a Langmuir probe. Data from a pair of single probes in the arcjet plume was also obtained in a simple experiment. The probes were placed in the plume at two different axial locations in order to give a rough estimate of the flow velocity. The electrical circuit diagrams for the photodiode and single probe measurements are included in Appendix C.

2.5.2 Low Speed Data Acquisition System

Arcjet performance is measured using a 12-bit Keithley Metrabyte DAS-1802HC data acquisition card installed in a 486 personal computer. Four channels of thruster operating parameters are recorded: thrust, mass flow rate, breakdown voltage and pulse rate. Data for all 4 measurements are recorded at 0.5 sec intervals where each data point represents the root mean square (RMS) value of 100 samples taken at a 1 kHz rate. In addition to recording data, the data acquisition

system was programmed to shut down the power supply automatically if a specified pulse rate or voltage was exceeded in order to protect the thruster hardware from an excessive power level.

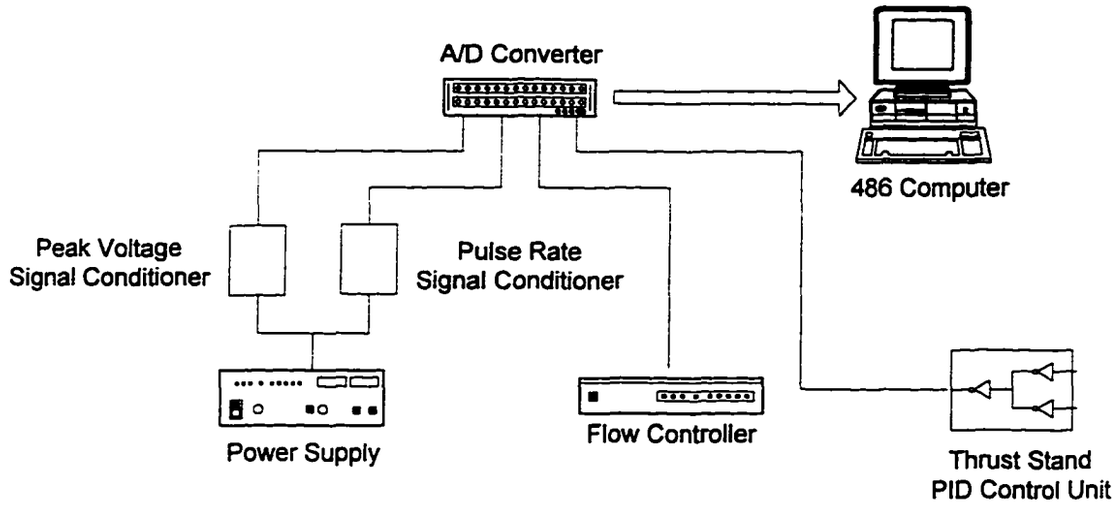

Fig. 2-11. Low sample rate (2 Hz) data acquisition system.

The thrust signal is taken from the PID control unit, and mass flow rate is obtained from the flow controller analog output. The thrust and mass flow rate determine the specific impulse from $I_{SP} = T_{HR} / (g\dot{m})$. Input power is determined from the measurements of pulse rate and stored energy at breakdown, $P = (\frac{1}{2} CV^2)(PPS)$. The specific impulse and input power are then used to calculate the thrust efficiency (see Eq. 4.3). The signals are processed and displayed in real-time allowing continuous evaluation of the thruster operating characteristics.

The average breakdown voltage and pulse rate measurements require special signal conditioning circuits. The average input power to the thruster is determined by the breakdown voltage and the pulse rate, but the analog output signal from the power supply is a time-varying voltage signal which is not directly usable to evaluate the average input power over a period of time. Two analog signal conditioning circuits are used to divide this signal into separate breakdown voltage and pulse rate signals (see Appendix C). Both the peak detector and pulse rate circuits are calibrated using a square wave from a WaveTek Model 147 sweep and function generator. The experimental uncertainty in the thruster operating voltage

is approximately 2% from the time response of the voltage peak detector circuit, and the voltage is the primary contributor to the uncertainty in the input power. The experimental uncertainty in the pulse rate is taken to be 1% based on the linearity of the frequency-to-voltage converter (National Semiconductor LM2917N). The uncertainty in the input power calculated from these two measurements is 4.1%.

2.5.3 Input Power Control

A constant current, switching-type power supply (Converter Power Model RCS 3000) provides a series of charging cycles to the arcjet storage capacitor. During initial tests, the power supply was allowed to begin a new charging cycle immediately after the arc discharge, and the pulse rate was then established by the magnitude of the charging current to the capacitors. This technique had the disadvantage that the pulse rate was coupled to the breakdown voltage, and small shot-to-shot variations in the breakdown voltage also led to variations in the pulse rate. This coupling caused instabilities in the operating characteristics of the thruster and also made it difficult to set the input power at any given level.

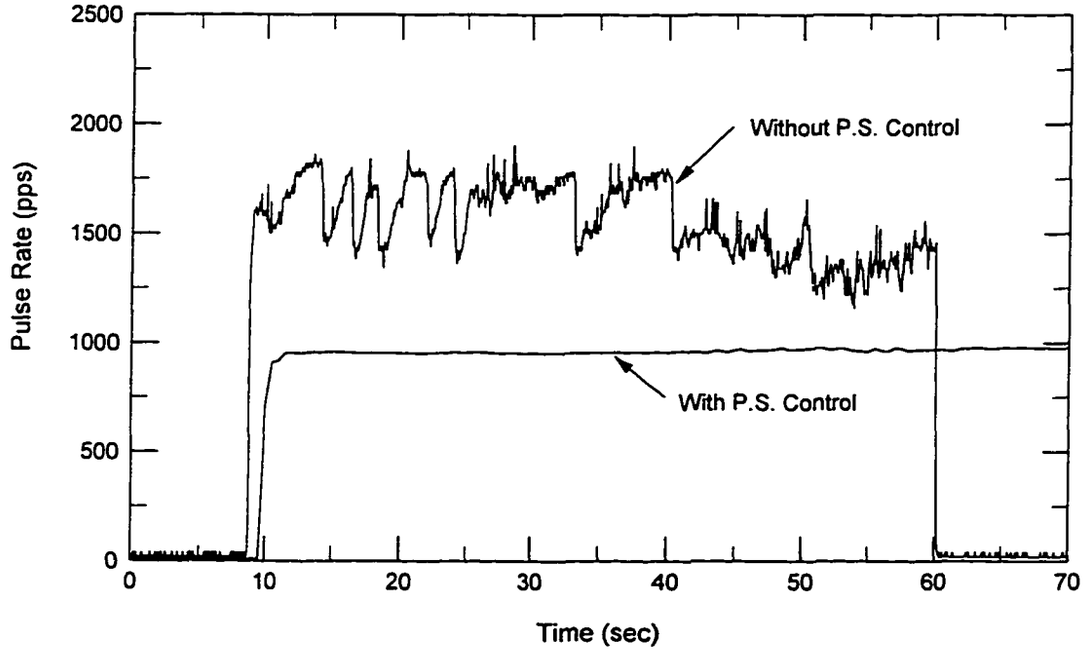

Fig. 2-12. Without external control of the power supply, the coupling of the pulse rate to the breakdown voltage leads to variations in arcjet input power.

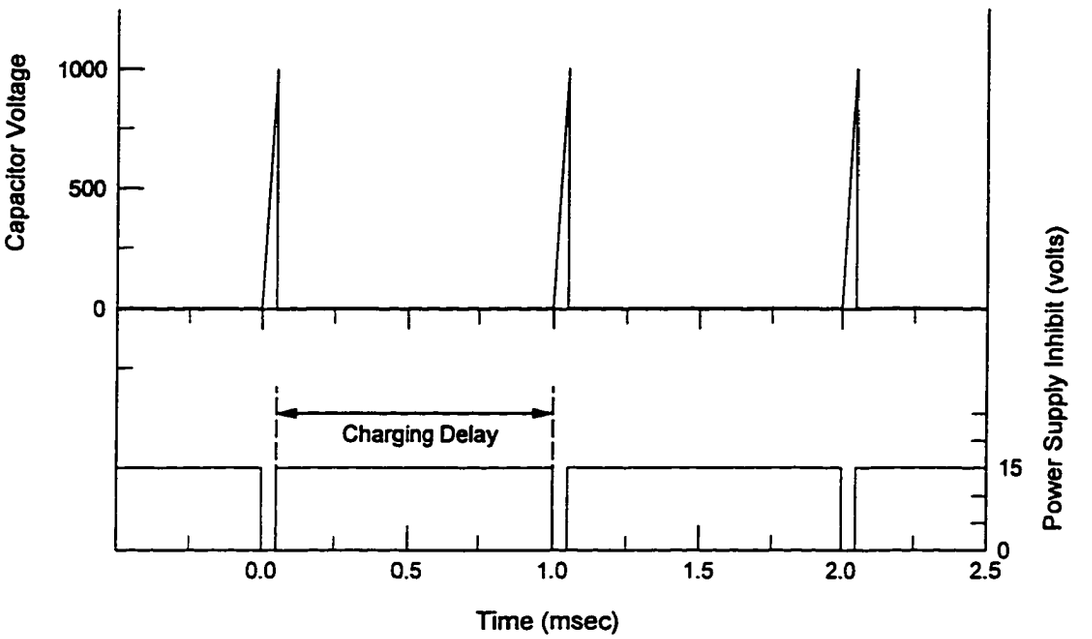

Fig. 2-13. Ideal capacitor charging voltage with power supply control. An inhibit signal to the power supply decouples the pulse rate from the breakdown voltage.

To correct the pulse rate / breakdown coupling problem, a separate control circuit was employed that stopped the power supply from charging the capacitor for a fixed delay, as shown in Fig. 2-13. A 15 volt inhibit signal produced a time delay that allowed the pulse rate to be set externally and reduced the instabilities caused by the feedback between the pulse rate and the breakdown voltage. The inhibit signal also allowed better control over the average input power to the arcjet.

2.6 Uncertainty Analysis Summary

The uncertainties in the four primary measurements (thrust, mass flow rate, voltage, pulse rate) are used to calculate the uncertainties in the three derived performance quantities (specific impulse, power, efficiency) from Eq. 1.3 to 1.5 below. The uncertainties in the pulsed arcjet performance measurements are summarized in Table 2-3.

$$\frac{w_{I_{SP}}}{I_{SP}} = \left[\left(\frac{w_{T_{HR}}}{T_{HR}} \right)^2 + \left(\frac{w_{\dot{m}}}{\dot{m}} \right)^2 \right]^{1/2} \qquad (1.3)$$

$$\frac{w_P}{P} = \left[\left(\frac{2w_{V_B}}{V_B} \right)^2 + \left(\frac{w_{PPS}}{PPS} \right)^2 \right]^{1/2} \tag{1.4}$$

$$\frac{w_\eta}{\eta} = \left[\left(\frac{2w_{T_{HR}}}{T_{HR}} \right)^2 + \left(\frac{w_{\dot{m}}}{\dot{m}} \right)^2 + \left(\frac{w_P}{P} \right)^2 \right]^{1/2} \tag{1.5}$$

Measurement	Symbol	Typical Values	Units	% Uncertainty
Thrust	T_{HR}	4 - 30	mN	1.9%
Mass flow rate	$\dot{m}$	1.5 - 17	mg/s	2.7%
Operating voltage	V_B	970 - 2300	volts	2.0%
Pulse rate	PPS	550 - 2630	pps	1.0%
Specific impulse	I_{SP}	160 - 305	sec	3.3%
Input power	P	24 - 120	watts	4.1%
Thrust efficiency	η	34 - 57	%	6.2%

Table 2-3. Summary of measurement uncertainties in pulsed arcjet performance.

References

[1] Curran, F. M., and Haag, T. W., "Extended Life and Performance Test of a Low-Power Arcjet," *Journal of Spacecraft and Rockets*, Vol. 29, No. 4, pp. 444-452, 1992.

[2] Curran, F. M., Sarmiento, C. J., Birkner, B. W, and Kwasny, J., "Arcjet Nozzle Area Ratio Effects," NASA TM 104477, 1990.

[3] Brophy, J. R., Pivirotto, T. J., and King, D. Q., "Investigation of Arcjet Nozzle Performance," AIAA Paper 85-2016, 1985.

[4] Whalen, M. V., "Low Reynolds Number Nozzle Flow Study," NASA TM 100130, July 1987.

[5] Bufton, S. A., *Exit Plane Plasma Measurements of a Low-Power Hydrazine Arcjet*, Ph.D. Thesis, University of Illinois at Urbana-Champaign, 1996.

[6] Patton, Bob, personal communication, 1995.

[7] Grover, F., *Inductance Calculations*, New York, 1962.

[8] Electronic Devices, Inc., 21 Gray Oaks Ave., Yonkers, NY, 10710.

[9] Black, J. W., Cowie, R. G., Glum, R. and Krier, H., "10 kW Laser Propulsion Thruster Test Program, Final Report," SBIR Program, NASA Contract Number NAS3-25636, 1991.

3. Numerical Model of Propellant Acceleration Process

This chapter presents a numerical technique for predicting the performance of a pulsed arcjet for a given geometry and set of operating conditions. The purpose of the numerical model is 1) to evaluate the effects of different design variables and operating conditions on overall performance, and 2) to quantify the individual energy losses in the arcjet. The parameter space being investigated includes 6 design variables (capillary length and diameter, nozzle throat diameter, nozzle area ratio and half angle, and external circuit inductance) as well as 5 operating variables (mean mass flow rate, pulse rate, pulse energy, inlet gas temperature, and wall temperature). Numerical results are compared with experimental data in Chapter 4.

3.1 Basic Assumptions

The propellant gas flow in the pulsed arcjet is viscous, time-dependent, chemically reacting, two-dimensional axisymmetric, and has time-varying boundary conditions. In addition, the presence of an arc requires consideration of electromagnetic effects during the discharge. The problem is extremely complex, and solving the full time-dependent Navier-Stokes equations coupled to Maxwell's equations is beyond the scope of this research. The problem can be simplified by making several important assumptions. First, the arc discharge itself occurs upstream of the nozzle and is very short in duration. Therefore, a good approximation is to neglect electromagnetic effects when solving for the gas dynamics of the nozzle flowfield. A second approximation is to use a quasi-1D formulation rather than a full 2-D system of equations. This approach gives reasonable results for overall performance characteristics (thrust, specific impulse and efficiency), although the effects of friction and heat transfer are incorporated in semi-empirical fashion rather than calculated directly from temperature and velocity gradients at the wall. A third approximation is to assume local thermodynamic equilibrium in both the capillary and the nozzle, and the validity of this assumption is discussed further in the next section.

3.2 Computational Domain

The pulsed arcjet geometry can be discussed in terms of four regions: the propellant inlet reservoir, the cathode orifice, the constant area capillary, and the converging-diverging nozzle. Each region is included in the numerical model where each region is used as a boundary condition for the neighboring downstream region. It is important to note that with this electrode geometry, all the energy addition from the arc discharge occurs in the capillary (region 2).

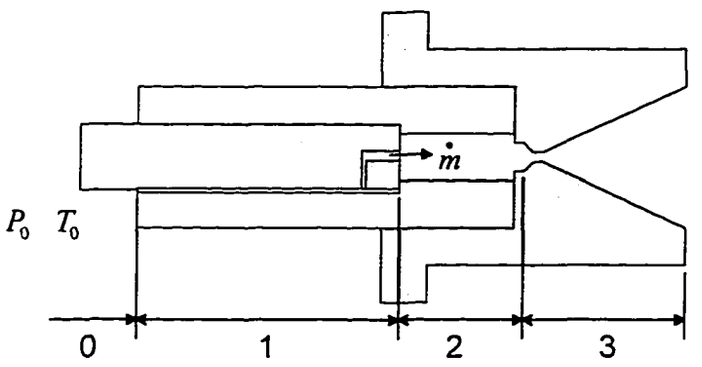

Fig. 3-1. Computational regions in the numerical model. The capillary (region 2) is the boundary condition for the nozzle (region 3).

Since the nozzle is the primary flowfield of interest, most of the computational effort is applied in region 3. The nozzle is modeled using a time-dependent finite-difference technique described in Section 3.3. The upstream boundary condition for the nozzle is the capillary. The capillary flow is modeled as a time-dependent, uniform-state, uniform-flow process, which implies that the gas conditions are spatially uniform throughout the volume. Even though a radial temperature gradient from the arc is likely to exist for a period of time after the discharge, the numerical model assumes complete mixing upstream of the nozzle so that the capillary can be represented by a single value of pressure and temperature. The upstream boundary condition for the capillary is the cathode orifice, and a single equation is used for this region. The cathode orifice boundary condition is a constant pressure, constant temperature (P_0, T_0) propellant inlet reservoir. The capillary, cathode orifice, and propellant inlet are discussed in Section 3.4.

3.3 The Nozzle Flowfield

This section describes the numerical method for the nozzle flowfield starting at the converging section. The five primary variables to be determined are the gas pressure, temperature, density, specific energy, and velocity (P, T, ρ, e, u). The three conservation equations give the three flow properties, ρ, u and e, and the two remaining flow properties, P and T, are calculated from the ideal gas law and equilibrium thermodynamics. Since the thruster is pulsed, the time-dependent terms are retained in the governing equations. The conservation equations of mass, momentum and energy for unsteady, quasi-1D flow are written in differential form,

Continuity
$$\frac{\partial \rho}{\partial t} = \frac{-1}{A}\frac{\partial}{\partial x}(\rho u A) \tag{3.1}$$

Momentum
$$\frac{\partial u}{\partial t} = -u\frac{\partial u}{\partial x} - \frac{1}{\rho}\frac{\partial P}{\partial x} - \frac{u^2}{2}\frac{4f}{D} \tag{3.2}$$

Energy
$$\frac{\partial e}{\partial t} = -u\frac{\partial e}{\partial x} - \frac{P}{\rho}\frac{\partial u}{\partial x} - \frac{P u}{\rho A}\frac{dA}{dx} + q_{FRICTION} + q_{NOZZLE} \tag{3.3}$$

In the energy equation, the $q_{FRICTION}$ term represents the conversion of kinetic energy into thermal energy due to friction. The q_{NOZZLE} term is the heat transfer from the gas to the nozzle wall. Ohmic heating in the arc and heat transfer in the capillary are incorporated in the upstream boundary condition and so do not appear in the nozzle equations. Since there are five unknowns, two additional equations are required in addition to the conservation equations. These are the ideal gas law and an equation of state for helium,

$$P = (1+\alpha)\rho R T \tag{3.4}$$

$$\frac{e}{R T} = \frac{3}{2}(1+\alpha) + 285{,}000\,\frac{\alpha}{T} \tag{3.5}$$

where R is the specific gas constant, 2077 J/kg K. The Saha equation is used to calculate the degree of ionization, α,

$$\frac{\alpha^2}{1-\alpha^2} = 1.308\times10^{-6}\, T^{5/2}\, P^{-1} \exp\left(\frac{-285{,}000}{T}\right) \tag{3.6}$$

where P is the pressure in atmospheres and T is in degrees Kelvin. For typical pulse energies investigated in this research, the bulk temperature of the gas is less than 10,000 K, and the ionization energy is less than 0.1% of the gas internal energy. Thus, axial diffusion can be neglected in the energy equation.

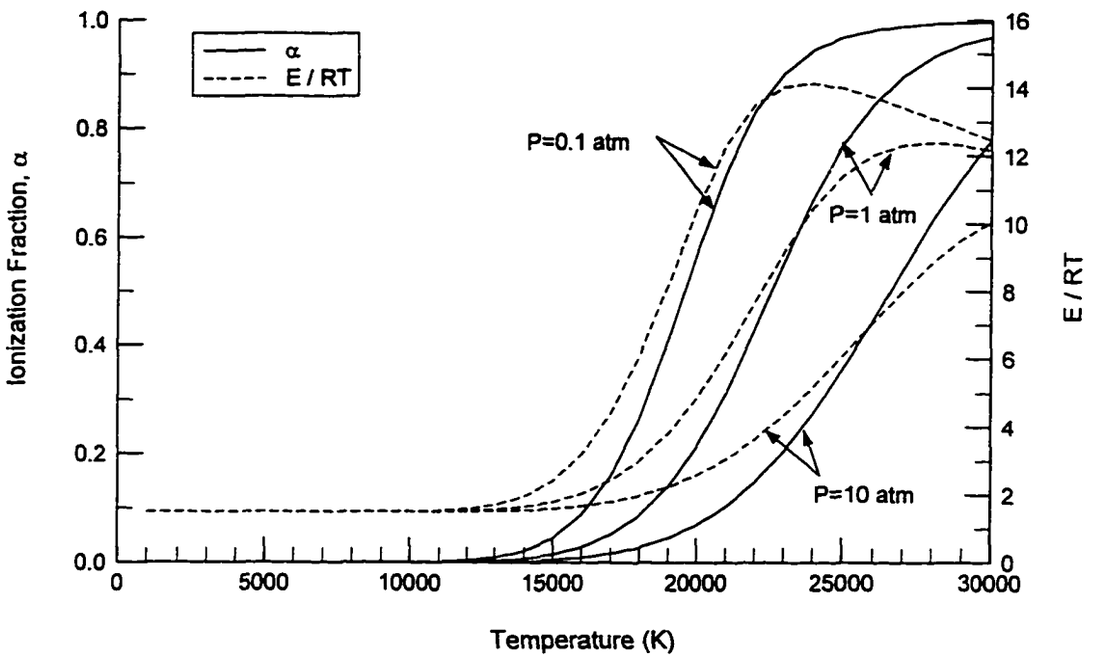

Fig. 3-2. Ionization fraction, α, and internal energy, E/RT for helium calculated from the Saha equation for three pressures, 0.1, 1, and 10 atmospheres.

The calculation of specific energy and density for a given pressure and temperature is straight-forward using Eqs. 3.4 to 3.6. However, calculating T and P from a given e and ρ is not as straight-forward because it is difficult to invert the equations into a form where P and T can be calculated directly. When this is required in the code, a Newton-Raphson procedure is employed to iterate on the thermodynamic variables until convergence to the proper pressure and temperature is achieved.

The use of equilibrium thermodynamics must be considered carefully. The gas pressure after the arc discharge is typically several atmospheres, and the

recombination time of electrons and atoms is on the order of 10^{-12} to 10^{-10} seconds. Most of the ionization energy is therefore recovered in the capillary, and the particles entering the nozzle are primarily helium atoms. Further, since helium is monatomic, the rotational and vibrational modes do not need to be considered as they do for diatomic propellants. Hence, it is reasonable to use equilibrium calculations for a pulsed arcjet using helium propellant.

For diatomic propellants such as hydrogen or simulated-hydrazine, dissociation is significant even for equilibrium conditions in the capillary, and the gas entering the nozzle is a multi-component mixture rather than a single species. At the typically low gas densities and short residence times in the nozzle, the number of collisions between particles is small, and the gas composition in the nozzle may be closer to chemically-frozen than equilibrium. The assumption of thermodynamic equilibrium may underestimate ionization and dissociation frozen flow losses substantially, and a chemically-frozen flow or finite-rate kinetic model should be used instead of the equilibrium assumption for diatomic propellants. The nozzle energy equation should be evaluated to determine if additional terms, such as mass diffusion, should be included.

3.3.1 Nozzle Friction and Nozzle Heat Transfer

While the quasi-1D model does not describe radial gradients, the overall results for thruster performance can be reasonably simulated using an appropriate friction factor and heat transfer coefficients. For fully developed laminar flow in a straight circular tube, the friction factor is often expressed as $f = 16 / \mathrm{Re}$. However, this expression for the friction factor assumes that fluid properties, including density, are constant along the length of the tube. The pulsed arcjet has a high velocity, unsteady boundary layer with temperature dependent properties, and the friction factor for steady, constant property laminar flow tends to overpredict viscous effects in the nozzle. For the pulsed arcjet model, the laminar friction factor with a temperature correction is used,[1]

$$f = \frac{16}{\mathrm{Re}} \left(\frac{T}{T_{WALL}} \right)^{m} \tag{3.7}$$

where the Reynolds number, $\mathrm{Re} = 4\dot{m}/\pi\mu D$, is calculated based on a local diameter, D, and local flow conditions. Note that the Reynolds number is time-dependent because the temperature and thus viscosity vary with time, as does the instantaneous mass flow rate. The viscosity is calculated (Appendix E) using a power law relationship,

$$\mu = 1.887\times10^{-5}\left(\frac{T}{273}\right)^{0.7} \quad [kg/m\ \mathrm{sec}] \tag{3.8}$$

An appropriate value for the exponent, m , in Eq. 3.7 is not readily available for the case of a high velocity, internal flow with variable properties in a variable area duct. A discussion by Kays and Crawford[1] suggest that for external flows, possible values for the exponent are $m = 0.12$ for laminar flow and $m = 0.5$ for turbulent flow. The Reynolds numbers in the pulsed arcjet are typically on the order of 1000 for the experiments described in Chapter 4 for helium propellant. The low Reynolds numbers together with the strong favorable pressure gradient in the nozzle would seem to imply that using the laminar flow value for m would be appropriate. However, when both values were evaluated for the pulsed arcjet, the m=0.5 value gave better comparison with the experimental data. This result could be attributed to the transient nature of the flow or possibly the variation in fluid properties along the length of the nozzle. In any case, the exponent, m, was set equal to 0.5 for all the numerical results presented in Chapter 4. A more complete analysis of the friction factor would be warranted if the experimental data were sufficient to assess the results.

The two heat transfer terms in the energy equation include 1) frictional heating and 2) heat transfer from the propellant gas to the nozzle wall. The frictional heating term is,

$$q_{FRICTION} = \frac{u^3}{2}\frac{4f}{D} \quad [W/kg] \tag{3.9}$$

Heat transfer in the nozzle is calculated using the Chilton-Colburn analogy,[2,3]

$$q_{NOZZLE} = \frac{32\ \kappa}{\rho D^2}\left(T_{WALL} - T_{AW}\right)\mathrm{Pr}^{4/3} \quad [W/kg] \tag{3.10}$$

The gas thermal conductivity used in Eq. 3.10 is calculated from a power law relationship (see Appendix E),

$$\kappa = 0.148 \left(\frac{T}{300} \right)^{0.75} \quad [W/m-K] \tag{3.11}$$

The variable T_{AW} is the adiabatic wall temperature and is calculated from,

$$T_{AW} = T + r_C \left(\frac{u^2}{2\, C_P} \right) \tag{3.12}$$

where r_c is the recovery factor,[1] set equal to the square root of the Prandtl number, $\sqrt{Pr}$.

3.3.2 Wall Temperature

The heat transfer from the gas to the nozzle and capillary walls is calculated using a constant value for the wall temperature. Spatially, the temperature can be assumed to be reasonably uniform in the nozzle material because the thermal conductivity of tungsten is roughly 100-200 times that of helium for gas temperatures below 10,000 K. Similarly, the thermal conductivity of boron nitride is 10-20 times that of the helium gas, and therefore temperature gradients along the capillary wall are assumed small.

The time-variation in the wall temperature requires a more detailed transient heat conduction analysis. The problem is similar to that of determining the surface temperature of an observation window in a shock tube, as discussed by Roberts[4] from the analytical solution of Luikov.[5] The transient heat conduction problem for two semi-infinite rods with different initial temperatures and thermal conductivity's brought into contact at t = 0 can be solved analytically. The temperature at the gas-solid interface instantaneously adjusts to a temperature T_S,

$$T_S = T_{WALL} + \frac{K_\varepsilon}{1 + K_\varepsilon} \left(T_{GAS} - T_{WALL} \right) \tag{3.13}$$

where T_{GAS} is the gas temperature, and K_ε is defined by,

$$K_{\varepsilon} = \left(\frac{\kappa_{GAS}}{\kappa_{WALL}}\right)\left(\frac{\alpha_{WALL}}{\alpha_{GAS}}\right)^{\frac{1}{2}} \tag{3.14}$$

For values of $K_{\varepsilon} << 1$, the surface temperature can be assumed to be approximately equal to the initial wall temperature. Typical values are shown in Table 3-1 below.

	Helium	Boron Nitride	Tungsten	[Units]
T	5000	300	300	[K]
κ	1.22	40	178	[W/m-K]
ρ	0.16	1900	19300	[kg/m^3]
C_P	5193	350	134	[J/kg-K]
	K_ε =	0.0062	0.0015	

Table 3-1. Material properties and K_{ε} for transient heat conduction in the capillary and nozzle. Since $K_{\varepsilon} << 1$, the surface temperature can be assumed constant during a pulse.

3.3.3 The Time-Marching Procedure

The converging-diverging nozzle is a mixed subsonic-supersonic flow problem. For steady flow, the subsonic flowfield is described by *elliptic* differential equations, and the supersonic flowfield is described by *hyperbolic* differential equations. The mixed nature of the flow can cause mathematical and numerical difficulties as the equations change from elliptic to hyperbolic across the sonic line. The general idea of the time-marching procedure is to use the unsteady equations because they are hyperbolic in time, and they can be used to avoid some of the numerical difficulties associated with mixed subsonic-supersonic flows. Time-marching solutions can also be employed for steady-flows, in which case the time-marching technique is simply a means to obtain the steady solution. For the pulsed arcjet, the time-marching technique is especially useful in simulating the time-dependent behavior of the flowfield because it includes the transient behavior of the flowfield variables.

The numerical algorithm selected for this analysis is the MacCormack predictor-corrector, which has been used successfully to study time-dependent chemically-reacting flows in nozzles.[6, 7, 8, 9] Further, the algorithm is second-order

accurate in time. At a given time, the x -derivatives are calculated using forward spatial differences, for example,

Forward Spatial Difference

$$\frac{\partial u}{\partial x} = \frac{u(x+\Delta x)-u(x)}{\Delta x} \tag{3.15}$$

The $\partial\rho/\partial t$, $\partial u/\partial t$, and $\partial e/\partial t$ time derivatives are calculated from the continuity, momentum and energy equations (Eq. 3.1 to 3.3), and predicted values for the flow properties at time, $t + \Delta t$, are calculated from the first term in a Taylor series,

Predictor step

$$\bar{u}(t+\Delta t) = u(t) + \frac{\partial u}{\partial t}\Delta t \tag{3.16}$$

These predicted values are then used to recalculate the x - derivatives with rearward spatial differences,

Rearward Spatial Difference

$$\frac{\partial \bar{u}}{\partial x} = \frac{\bar{u}(x) - \bar{u}(x-\Delta x)}{\Delta x} \tag{3.17}$$

The corrector time derivatives, $\partial\bar{\rho}/\partial$ t, $\partial\bar{u}/\partial$ t, and $\partial\bar{e}/\partial$ t, are recalculated using these rearward differences. Finally, the flow properties at the $t + \Delta t$ time step are calculated using average values for the time derivatives, for example,

Corrector step

$$u(t+\Delta t) = u(t) + \frac{1}{2}\left(\frac{\partial u}{\partial t} + \frac{\partial \bar{u}}{\partial t}\right)\Delta t \tag{3.18}$$

The numerical procedure marches forward in time, and all five flow variables are updated before starting the next time step.

3.4 Boundary and Initial Conditions

The numerical solution for the nozzle flowfield requires proper specification of two boundary conditions plus an initial condition. The governing equations require that these conditions be specified in terms of the primary variables, P, T, ρ, e, and u. However, these primary variables cannot be set arbitrarily because they are physically controlled by other inputs, such as the pulse energy, pulse rate, and capillary geometry. The nozzle upstream boundary condition is time dependent,

since the capillary conditions vary with time as the pressure and temperature decay following a pulse. This reservoir blowdown process is coupled to the nozzle via the choked flow condition in the nozzle throat.

The initial condition is complicated by the condition that for a repeatable series of pulses, the conditions in both the capillary and the nozzle at the end of one pulse must equal the conditions at the beginning of the next pulse. Starting at cold flow, the time scale for the reservoir blowdown process is slightly longer than the time between pulses, so that the conditions in the capillary do not return to the conditions for steady flow. The required upstream initial conditions that will produce a repeatable series are not known *a priori* and must be calculated as part of the solution procedure. Only the downstream boundary condition is relatively straight-forward. The numerical procedures for the boundary and initial conditions are described in Section 3.4.1 to 3.4.3 below.

3.4.1 Upstream Boundary Condition: the Capillary

The numerical solution for the nozzle begins at the entrance to the converging section, although the computational domain could also be extended to include the capillary. In this analysis, the capillary is used as a boundary condition in order to avoid possible difficulties associated with the propellant jet from the cathode orifice and the change in cross-sectional area at the cathode tip. The pulsed arcjet is modeled as a converging-diverging nozzle fed by a reservoir with a finite volume where the capillary is a reservoir with a prescribed P(t) and T(t).

Since the capillary is being used as a boundary condition, radial gradients and axial gradients in the capillary are not considered explicitly, though they are discussed qualitatively here. The flow velocities in the capillary are low subsonic (~10 m/s), and the gas pressure is likely to be nearly constant over the length and radius of the capillary, since the characteristic time scale for the capillary (length divided by sound speed, L / a) is ~1-10 μsec which is much less than the characteristic time for pressure decay, > 100 μsec. In addition, except for end effects, axial gradients in temperature are small because the ohmic heating in the arc is axially uniform. The primary non-uniformity in the capillary is the radial distribution of temperature. As will be shown in Chapter 5, the arc does not

completely fill the capillary, and radial heat conduction leads to a radial temperature profile that varies from a peak in the arc channel to a minimum at the wall. However, these radial gradients are not modeled in the quasi-1D equations, and the gas temperature profile is replaced by a propellant bulk temperature. The implicit assumption is that complete mixing of the cold gas near the walls with the hot gas in the arc channel occurs in the converging section to the nozzle.

A previous study[10] of boundary conditions for the time-marching technique showed that specifying a steady upstream pressure and temperature results in good numerical behavior and convergence to the correct steady state result. For the pulsed arcjet, the upstream boundary condition at the nozzle entrance is to set P(t) and T(t) at each time step based on reservoir conditions in the capillary. In order to determine the pressure and temperature in the capillary, the flow in the capillary is modeled as a uniform state, uniform flow thermodynamic process. The governing equations are conservation of mass and energy,

Mass
$$m_2^{t+\Delta t} = m_2^t + \left(\dot{m}_1 - \dot{m}_2\right)\Delta t \tag{3.19}$$

Energy
$$E_2^{t+\Delta t} = E_2^t + \left[\dot{m}_1\left(h_1 + \frac{v_1^2}{2}\right) - \dot{m}_2\left(h_2 + \frac{v_2^2}{2}\right) + Q_{ARC} - Q_{CAP}\right]\Delta t \tag{3.20}$$

The total mass and total energy of the propellant in the capillary are updated at each time step using these equations. The pressure and temperature are then calculated from the specific energy and density.

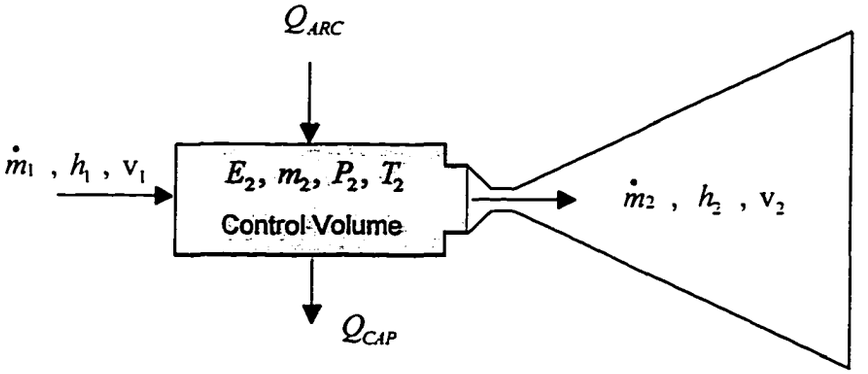

Fig. 3-3. Schematic for first law analysis of upstream boundary condition. The flow in the capillary is approximated as a uniform-state, uniform flow, time-dependent process.

The conservation equations for the capillary require specification of the mass flow and energy flux entering and exiting the capillary. The inlet mass flow to the capillary is calculated based on a pressure differential across the cathode orifice,

$$\dot{m}_1 = C_D A_1 \sqrt{\frac{2 P_1}{R T_1} \left(|P_1 - P_2| \right)} \quad [kg/s] \tag{3.21}$$

where A_1 is the minimum area of the cathode orifice, P_1 and T_1 are the upstream reservoir conditions, P_2 is the capillary pressure, and C_D is a discharge coefficient, set equal to 0.9. Note that since the capillary pressure varies with time, the instantaneous inlet mass flow also varies with time. For conditions where $P_2 > P_1$, the inlet gas flow is negative, meaning that the propellant gas is being blown back upstream through the cathode orifice.

The mass flow exiting the capillary is calculated using the equation for steady choked flow of a calorically perfect gas,

$$\dot{m}_2 = C_D \frac{A^* P_2}{\sqrt{R T_2}} \sqrt{\gamma \left(\frac{2}{\gamma + 1} \right)^{\frac{\gamma+1}{\gamma-1}}} \quad [kg/s] \tag{3.22}$$

The equation for exit mass flow rate (Eq. 3.22) is a quasi-steady approximation because this equation assumes that the mass flow rate at the inlet to the nozzle is equal to the mass flow rate at the nozzle throat. This assumption is not strictly valid for a time-dependent solution because it is based on the steady continuity equation. However, the quasi-steady approximation is used because the time scale for the pressure to equilibrate throughout the capillary is on the order of 10^{-6} seconds compared to the 10^{-3} second time scale for the pressure to decay in the capillary. Further the total volume of the converging section is less than 5% of the capillary volume.

The exit mass flow equation also assumes a sound speed for a thermally perfect gas rather than a chemically reacting gas or plasma, and includes a discharge coefficient to account for viscous effects in the throat. Still, the approximation is reasonable since at the arcjet peak temperatures, the error in the

sound speed is small. The discharge coefficient used here is a function of throat Reynolds number as described in Section 5.1.3 and Eq. 5.8.

The total energy, E_2, in the capillary is updated at each time step from the conservation of energy equation (3.20). The inlet gas temperature, T_1, is given as an input parameter, generally 300 K to match the experimental conditions. The exit gas enthalpy, h_2, is equal to the bulk enthalpy of the gas in the capillary. The last two terms in the capillary energy equation are 1) a source term due to arc heating and 2) heat transfer from the gas to the capillary walls. The arc heating term is the pulse energy added to the gas in the arc discharge. The arc heating term is calculated from Ohm's law,

$$Q_{ARC} = V_{ARC}\, I(t) \quad [watts] \tag{3.23}$$

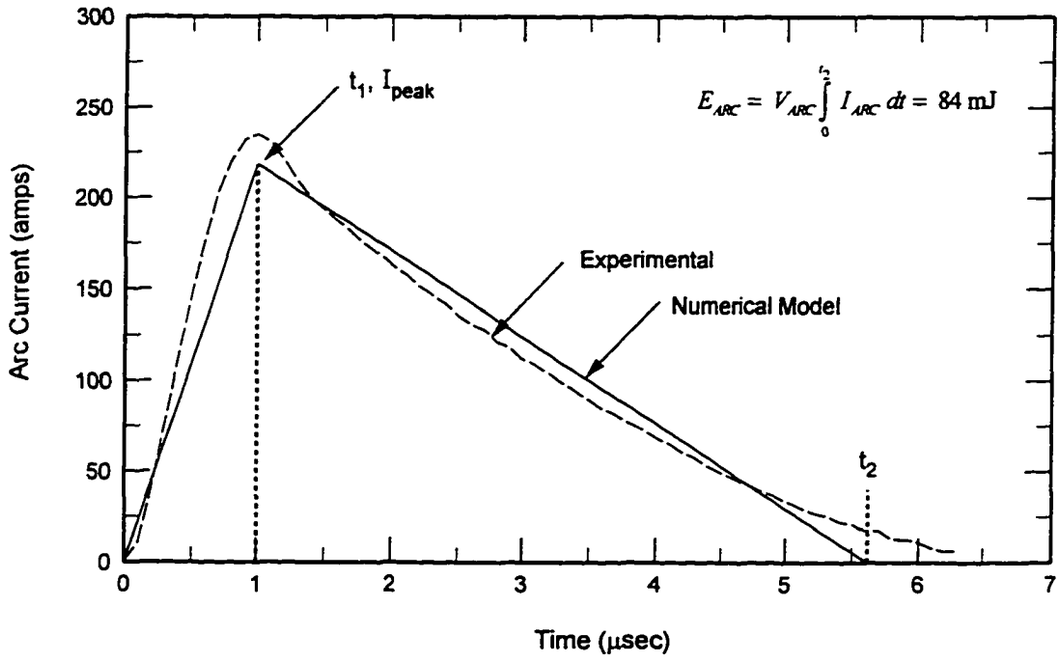

Fig. 3-4. Arc current used in the numerical model compared to experiment for an 84 mJ pulse. The arc current and voltage are used to calculate the arc heating term in the energy equation.

Though the arc heating occurs within 3-10 μsec and could be assumed instantaneous from a modeling standpoint, it is physically more accurate and also

straight-forward to use an arc heating term that varies with time. Thus a current pulse which closely approximates the experimental discharge conditions is used in the numerical analysis. The current is modeled as a linear increase from zero to a peak current within a specified rise time, typically 1 μsec, followed by a linear decrease to zero. The arc voltage is assumed to be constant, and the peak current is calculated based on the requirement that the area under the arc current curve is proportional to the pulse energy.

The required input parameters to determine I(t) are the pulse energy, arc voltage, external circuit inductance, and time to peak current. For most of the calculations presented here, only the pulse energy is varied, and the remaining variables are fixed at 100 volts, 2.9 μH, and 1 μsec for the arc voltage, circuit inductance, and time to peak current, respectively. The value of 100 volts corresponds to the arc voltage in the baseline thruster that is the subject of a parameter study in Chapter 4. The 2.9 μH inductance is selected to match the actual thruster value.

The heat transfer from the propellant gas to the capillary walls is determined using an average convection coefficient, $\bar{h}$, the capillary wall area, AWALL, and a temperature gradient based on the propellant bulk temperature and the wall temperature,

$$Q_{CAP} = \bar{h}\,(T_{GAS} - T_{WALL})\,A_{WALL} \quad [watts] \tag{3.24}$$

The heat transfer coefficient is replaced by a non-dimensional Nusselt number, defined as,

$$Nu = \frac{\bar{h}\,D}{\kappa_{GAS}} \tag{3.25}$$

When these two equations are combined, the capillary diameter drops out, and the expression for capillary heat transfer becomes,

$$Q_{CAP} = \pi\, Nu\, \kappa_{GAS}\, L\,(T_{GAS} - T_{WALL}) \quad [watts] \tag{3.26}$$

This model for calculating the capillary heat transfer represents a significant approximation in the numerical model. Capillary heat transfer is assumed to be

dominated by convection, though calculating a value for a heat transfer coefficient is not easily described by a simple flow model. For fully-developed steady laminar flow in a tube, the Nusselt number is equal to 3.66, which can be considered a lower bound for *Nu*. For fully-developed turbulent flow in a tube, the Nusselt number is a function of both the Reynolds number and Prandtl number with values up to approximately 1000.[1] The convective heat transfer in the capillary is likely to be influenced by transient effects, flow reversals, the velocity of the inlet jet, mixing regions, etc. Therefore, the Nusselt number is chosen based on the value that appears to match the trends in the experimental data. All the numerical results described here use a Nusselt number equal to 25, and *Nu* is not changed between cases.

Non-uniformities in the capillary gas are accounted for by selection of the Nusselt number. Other methods to account for non-uniformities could include using an arc radius rather than the capillary radius as the heat transfer area or defining the temperature difference based on a different peak temperature than the mass-averaged temperature, as is done here.

In addition to convection, other energy loss mechanisms in the capillary, such as radiation, recombination at the wall, sheath heating at the electrodes, which may or may not be negligible, are simply lumped into the fixed Nusselt number for the calculations. Using this fixed value for the Nusselt number gives results consistent with the experimental data over a wide range of conditions. An improved model for the capillary heat transfer which accounts for these individual energy losses could certainly be developed, though assessing the improvement to the model would require some type of experimental data to compare the results, and this data was not obtained in these experiments.

3.4.2 Downstream Boundary Condition

For the nozzle exit plane boundary condition, the flow properties are extrapolated from interior points with the restriction that the flow is supersonic. The exit plane properties cannot be extrapolated from interior points when the ambient pressure is such that subsonic conditions exist in the nozzle. Subsonic exit conditions are not investigated here, and the numerical model assumes supersonic

exit conditions. For large area ratio nozzles with low flow rates, viscous effects are large enough to decelerate the flow to a Mach number less than unity inside the nozzle. The numerical simulation did not pass through unity Mach number without becoming unstable, and in any case, these results would be invalid because extrapolating the exit plane properties from interior points is an improper boundary condition for subsonic flow. The ambient pressure is specified as an input because it appears in the thrust equation, and P_{AMB} is set equal to 5 Pa, which corresponds roughly to the background pressure in the vacuum tank when the thruster is running.

3.4.3 Initial Condition

For the $t = 0$ initial condition, the five primary variables, u, ρ, e, T, and P must be set at each grid point as well as the capillary. However, the initial conditions are not known in advance because the initial flow conditions for a series of repeatable pulses are significantly different from those based on steady flow. Determining the proper initial condition in the capillary requires a separate iterative solution for the following reason. Before the first pulse, the pressure and temperature in the capillary are established by steady choked flow at the given mass flow rate. When the first pulse occurs, increases in the gas pressure and temperature are determined by the pulse energy and the initial propellant mass. The pressure and temperature then decrease monotonically on a time scale that is slightly longer than the time between pulses. The second pulse occurs before conditions in the capillary return to the original starting conditions, such that energy addition from the second arc discharge starts at a higher initial temperature than the first discharge. The capillary flow conditions converge to a repeatable series after approximately 10-20 pulses, as illustrated in Fig. 3-5. This iterative procedure is performed solely to obtain the proper upstream initial condition on pressure and temperature at the inlet to the nozzle, $P\,(x=0,\ t=0)$ and $T\,(x=0,\ t=0)$. In the numerical calculation, the pulse energy is held constant: experimentally, the pulse energy varies during the startup series because the breakdown voltage and hence pulse energy decrease as the mass in the capillary decreases. The average propellant mass in the capillary after the series of startup pules is approximately

one half of the initial cold flow propellant mass, leading to higher peak temperatures than would be predicted if the starting series of pulses were not accounted for.

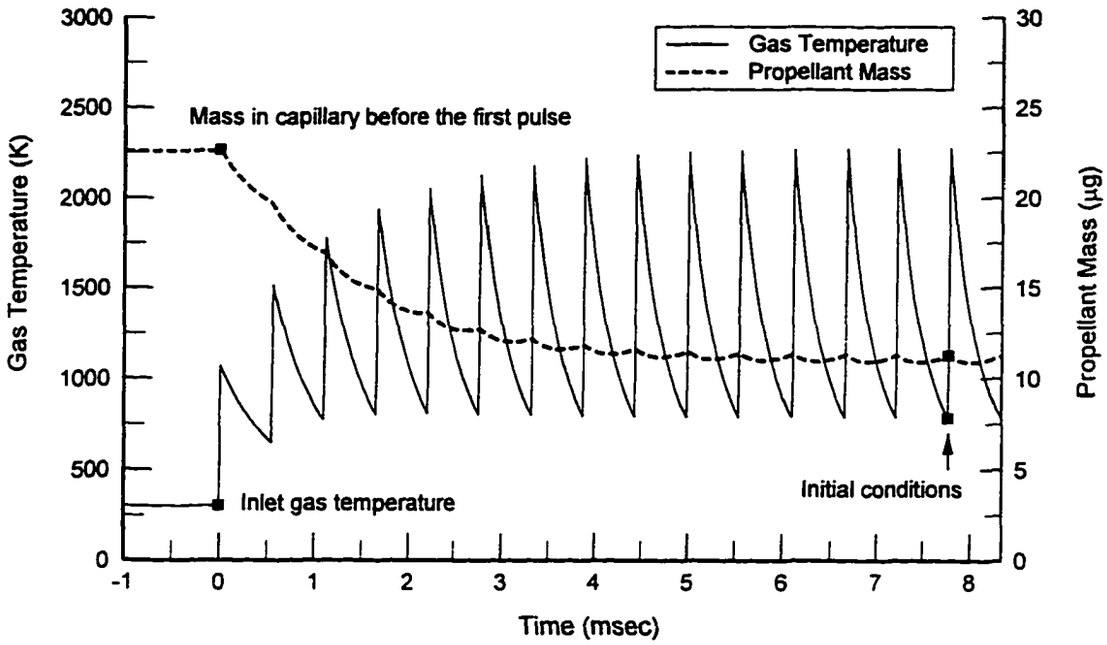

Fig. 3-5. Numerical results for the initial propellant mass and gas temperature in the capillary during a typical startup series of pulses at 1800 pps.

3.5 Equations for Thrust, Specific Impulse, and Efficiency

The thrust and impulse vary with time during an individual pulse, and calculating the time-averaged performance requires that these parameters be numerically integrated over the pulse time. The instantaneous thrust is calculated from,

$$T_{HR} = \dot{m}_E U_E + (P_E - P_{AMB}) A_E \quad [N] \tag{3.27}$$

For a time period $\tau = 1 / PPS$, the impulse "bit" per pulse is,

$$I = \int_0^{\tau} T_{HR}\, dt \quad [N-s] \tag{3.28}$$

The average specific impulse is calculated from the total impulse and the total propellant mass expended during time τ.

$$I_{SP} = \frac{I}{g\,M_P} = \frac{\int_0^\tau T_{HR}\,dt}{g\int_0^\tau \dot{m}_E\,dt} \quad [s] \tag{3.29}$$

A detailed analysis of the thruster efficiency is useful in evaluating the energy losses in the arcjet; that is, the energy that is not converted into useful thrust. For a repeatable series of pulses, the initial and final conditions are identical, and the first law of thermodynamics for the system can be written as,

$$Q_{ARC} + \int \dot{m}_1\left(h_1 + \frac{v_1^2}{2}\right)dt = \int \frac{1}{2}\dot{m}_E\,U_E^2\,dt + \int \dot{m}_E\,h_E\,dt + Q_{CAP} + Q_{NOZ} \tag{3.30}$$

The terms on the left hand side of the equation represent the total enthalpy of the gas entering the system plus the energy transferred to the propellant by the arc. The terms on the right hand side of the equation are the kinetic and internal energy leaving the system and heat transfer across the system boundary.

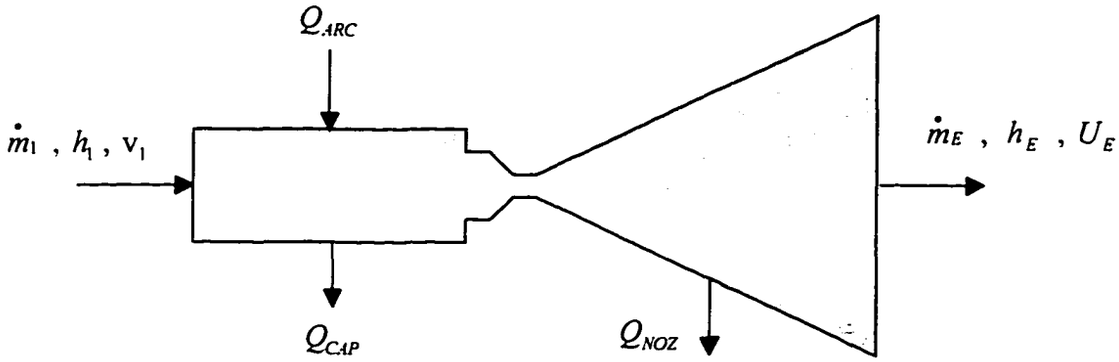

Fig. 3-6. Schematic diagram for first law analysis of energy losses. The control volume includes both the capillary and the nozzle.

In a conical nozzle, the velocity vector of the gas is axial only along the centerline, while along the nozzle wall, the velocity vector is at the nozzle half angle. For an ideal conical nozzle, the thrust is reduced by a factor ½(1+cos α).[11] The kinetic energy term is separated into axial and radial components,

$$\int \frac{1}{2}\dot{m}U_E^2\,dt = \frac{1+\cos\alpha}{2}\int \frac{1}{2}\dot{m}U_E^2\,dt + \frac{1-\cos\alpha}{2}\int \frac{1}{2}\dot{m}U_E^2\,dt \tag{3.31}$$

where the first term on the right hand side is the kinetic energy that contributes to thrust and the second term is a flow divergence loss.

The internal energy term can also be separated into two terms: a pressure term that contributes to thrust plus a frozen flow loss. The first term accounts for the (P_E - P_{AMB})A_E term in the thrust equation, and the second term represents the internal energy remaining in the gas that is not converted into kinetic energy.

$$\int \dot{m}_E h_E \, dt = \int \dot{m}_E \frac{P_E}{\rho_E} \, dt + \int \dot{m}_E e_E \, dt \tag{3.32}$$

Finally, the heat transfer losses include the heat transfer from the propellant gas to the walls in both the capillary, Q_{CAP}, and the nozzle, Q_{NOZ}. The total thrust efficiency is calculated from the following:

$$\eta = \frac{\frac{1+\cos\alpha}{2} \int \frac{1}{2} \dot{m}_E U_E^2 \, dt + \int \dot{m}_E \frac{P_E}{\rho_E} \, dt}{Q_{ARC} + \int \dot{m}_I \left(h_I + \frac{V_I^2}{2} \right) dt} \tag{3.33}$$

This expression reduces to the thrust efficiency equation in section 1.1.2 for steady flow. The individual terms representing the divergence loss, frozen flow loss, and heat transfer can also be calculated using the above equations.

3.6 Grid Spacing, Stability, and Numerical Accuracy

3.6.1 Grid Spacing

The grid geometry used in the numerical analysis consists of three parts: a 45 degree half angle conical converging section, a throat region with a constant radius of curvature (R_t = 2 mm), and a conical diverging section. Geometric variables that may be specified as inputs are the nozzle half angles, throat diameter, radius of curvature, and area ratio. The grid points have equal axial spacing, and the number of grid points may be specified as an input parameter. For most calculations, 50 grid points are used. A few calculations with 100 grid points and 200 grid points were performed to verify grid independence. For a sample

calculation, the differences between the 50 and 200 grid point results were 0.28 seconds in specific impulse, and the change in thrust efficiency was 0.15%.

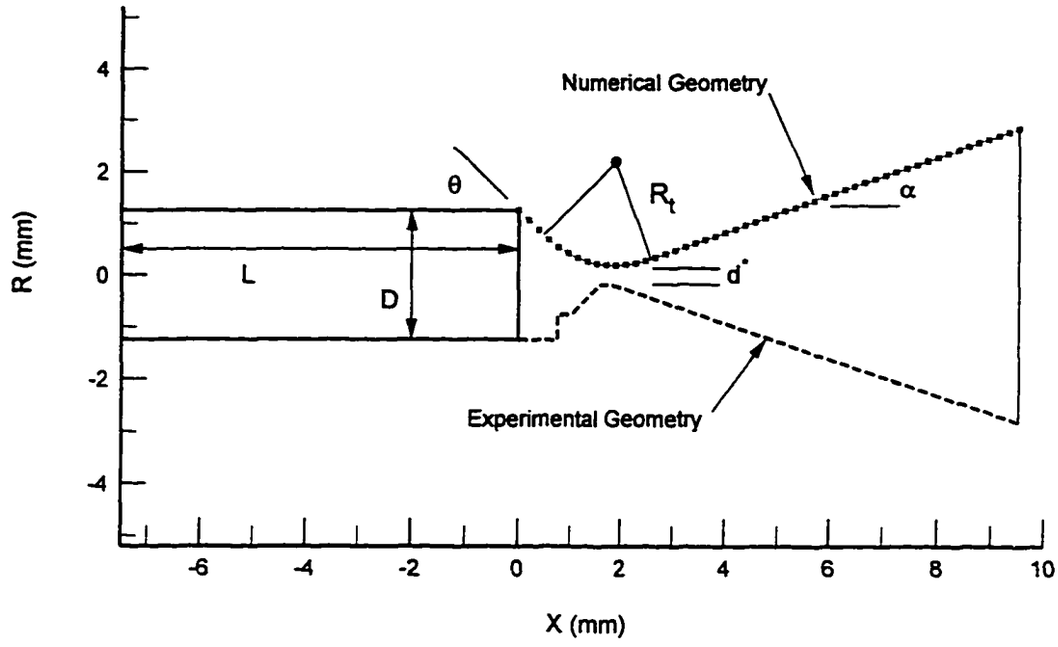

Fig. 3-7. Example of the computational domain and grid geometry with 50 points and equal spacing used in the numerical model.

3.6.2 Stability Restrictions

The time-marching solution calculates the flowfield variables, u, ρ, e, T, and P at each spatial point in the nozzle at each time step. The size of the time step is limited by the stability of the numerical calculation. The CFL condition[12] (Courant, Friedrichs, Lewy) is used to calculate the size of the time step from the following equation,

$$\Delta t = CFL \frac{\Delta x}{(u+a)} \tag{3.34}$$

At each time step, a time step size is calculated at each spatial location, and then the minimum value of Δt is selected for the next time step. The CFL number is set equal to 0.8 for all calculations. Typical time steps are approximately 15-20 nsec, or 2 x 10^4 time steps for a single pulse at 3000 pulses per second.

3.6.3 Numerical Accuracy

Two checks of numerical accuracy are examined for each calculation. First, global conservation of mass and energy are checked at each time step, as shown in Fig. 3-8. Global conservation of mass and energy in the numerical model using 100 grid points.. The maximum errors in mass (~0.5 %) and energy (~0.15 %) occur early in the pulse, but these errors cancel out quickly and do not propagate through the calculation. The reason that the errors peak during the pulse and then drop significantly was not studied. For a complete cycle, conservation of mass is satisfied within less than 0.1% and conservation of energy within 0.01% for 50 grid points. For a calculation with 200 grid points, the conservation of mass is improved by a factor of ten, though conservation of energy is only slightly better.

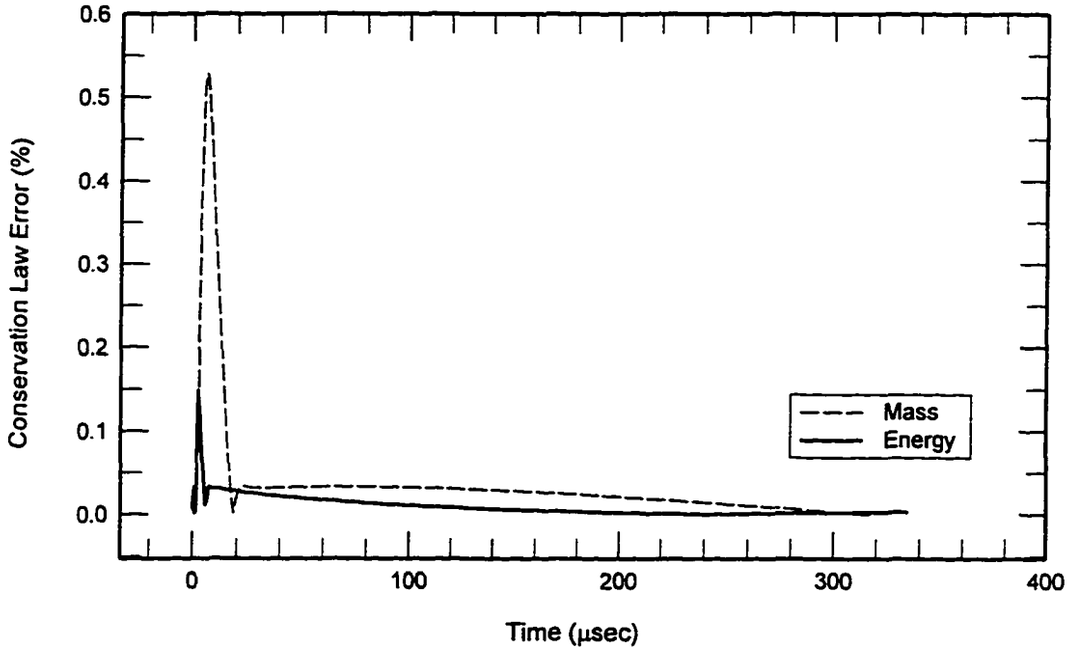

Fig. 3-8. Global conservation of mass and energy in the numerical model using 100 grid points.

The second check on numerical accuracy involves a comparison of the mass and energy in the system at both the beginning and end of the calculation. These values should be identical in order to represent a series of identical pulses. Typically, the errors between the initial and final states are within 1.5% to 2.0% for

mass and 0.5% to 1.0% for energy regardless of the number of gridpoints. The accuracy of the initial condition could be improved by additional iteration between the initial condition calculation and the time-marching procedure. However, the achieved accuracy was determined to be sufficient for assessing the pulsed arcjet performance trends.

3.7 Key Variables for a Typical Pulse

The numerical model gives the capillary and nozzle flow conditions at each grid point at each time step. A few of the important variables are shown in the plots below as an example of the pulsed arcjet flow conditions.

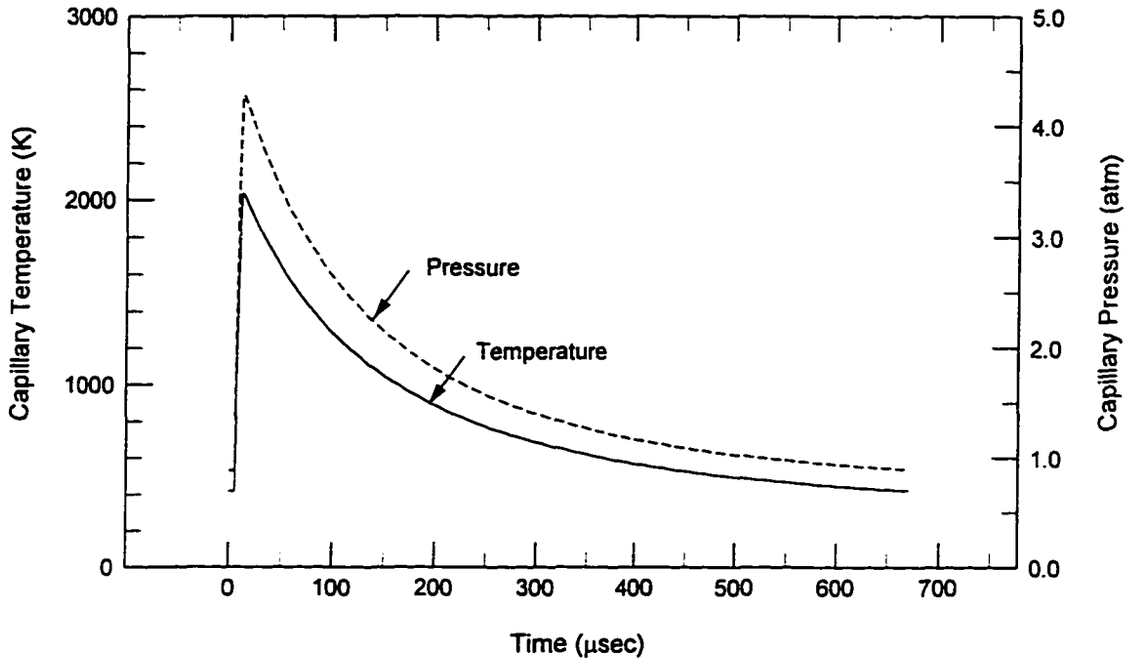

Fig. 3-9. Capillary temperature and pressure for an 80 mJ pulse at 1500 pps. The conditions are the end of the pulse are equal to the initial conditions.

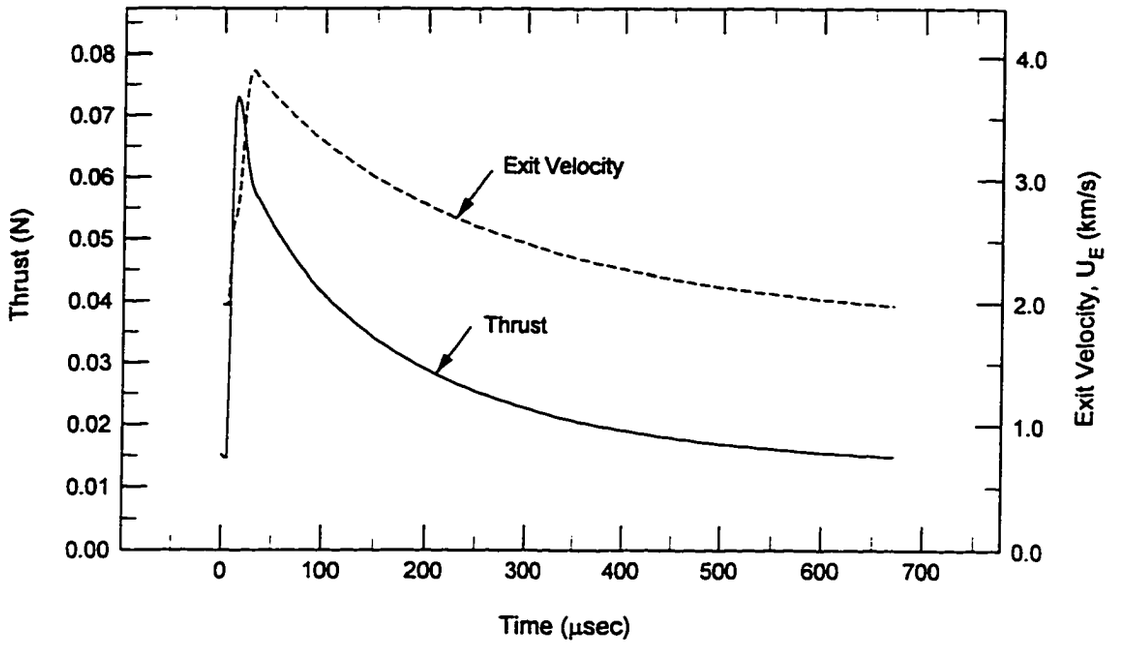

Fig. 3-10. Thrust and exit velocity for an 80 mJ pulse at 1500 pps.

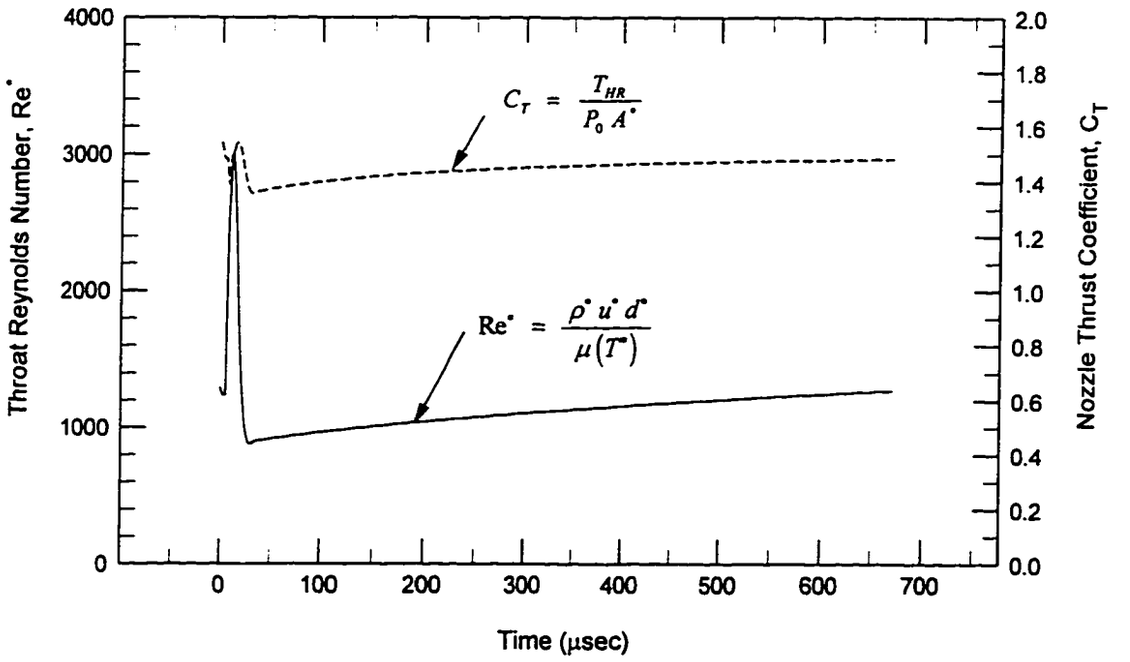

Fig. 3-11. Reynolds number based on throat diameter and nozzle thrust coefficient for an 80 mJ pulse at 1500 pps.

References

[1] Kays, W. M., and Crawford, M. E., "Convective Heat Transfer High Velocities," *Convective Heat and Mass Transfer*, McGraw Hill, New York, 1980.

[2] Incropera, F. P., and DeWitt, D. P., "Introduction to Convection," *Fundamentals of Heat Transfer*, John Wiley and Sons, New York, 1981.

[3] Beans, E. W., "Nozzle Design Using Generalized One-Dimensional Flow," *Journal of Propulsion and Power*, Vol. 8, No. 4, pp. 917-920, 1991.

[4] Robert, T., *Shock Tube Ignition and Combustion of Aluminum/Magnesium Alloy Particles in Oxygen at High Pressure*, Ph.D. Thesis, University of Illinois at Urbana-Champaign, 1993.

[5] Luikov, A. V., "Boundary Conditions of the Fourth Kind," *Analytical Heat Diffusion Theory*, (J. P. Harnett, Ed.), Academic Press, New York, 1968.

[6] Anderson, J. D., "The Time-Marching Technique: with Application to Supersonic Blunt Bodies and Nozzles," *Modern Compressible Flow*, McGraw-Hill, Inc., New York, 1990.

[7] Anderson, J. D., "A Time-Dependent Analysis for Vibrational and Chemical Nonequilibrium Nozzle Flows," *AIAA Journal*, Vol. 8, No. 3., pp. 545-550, 1970.

[8] Anderson, J. D., "Time-Dependent Solutions of Nonequilibrium Nozzle Flows - A Sequel," *AIAA Journal*, Vol. 8, No. 12, pp. 2280-2282, 1970.

[9] Vamos, J. S., and Anderson, J. D., "Time-Dependent Analysis of Nonequilibrium Nozzle Flows with Complex Chemistry," *Journal of Spacecraft and Rockets*, Vol. 10, No. 4, pp. 225-226, 1973.

[10] Griffin, M. D., and Anderson, J. D., "On the Application of Boundary Conditions to Time Dependent Computations for Quasi One-Dimensional Fluid Flows," *Computers and Fluids*, Vol. 5, pp. 127-137, 1977.

[11] Hill, P. and Peterson, C., "Chemical Rocket Thrust Chambers," *Mechanics and Thermodynamics of Propulsion*, 2nd Edition, Addison-Wesley Publishing Company, Inc., Massachusetts, 1992.

[12] Anderson, D. A., Tannehill, J. C., and Pletcher, R. H., "Fundamentals of Finite-Difference Methods," *Computational Fluid Mechanics and Heat Transfer*, Hemisphere Publishing Corporation, New York, 1984.

4. Performance of the Pulsed Arcjet

This chapter describes the experimental and numerical results for a pulsed arcjet operating with helium propellant. The first half of the chapter describes the general operating characteristics and thermal steady state performance. The second half summarizes the results of a numerical study of the design variables and discusses the energy loss mechanisms in the pulsed arcjet. A total of ~20 hours of run time were accumulated on the pulsed arcjet during the performance testing, and the total pulse count was on the order of 10^8 pulses. Total energy processed by the thruster during the entire experimental study was 10^6 to 10^7 joules.

4.1 Cold Flow Measurements.

The experimental specific impulse for steady flow of room temperature helium propellant is shown in Fig. 4-1. compared with numerical results. Even though the numerical model uses a time-marching technique, the model can be applied to steady flows because it converges to the steady flow result when steady boundary conditions are specified, that is, the pulse energy is set to zero. The comparison of the numerical and experimental specific impulse is good, considering that friction is accounted for numerically using a simple laminar friction factor.

The specific impulse decreases at low Reynolds numbers due to viscous effects in the nozzle.[1, 2] At throat Reynolds numbers below approximately 500 (see Fig. 4-2), the numerical model indicates that the exit Mach number goes subsonic for large area ratios. The flow does not have a shock, but instead the gas decelerates in a viscous, shockless transition. Physically, the directed kinetic energy of the gas particles is transferred back into random thermal energy by viscous dissipation, and this translates to an increase in the gas static temperature. For Re = 600, the gas temperature decreases to a minimum 1.5 mm downstream from the nozzle throat and then increases. At a distance corresponding to the exit plane of a 230:1 area ratio nozzle, the flow has decelerated down to nearly sonic speed. Detailed measurements in a 66:1 area ratio conical nozzle with room temperature nitrogen have been obtained in an electron beam experiment by Rothe[3] that show similar results inside low Reynolds number nozzles.

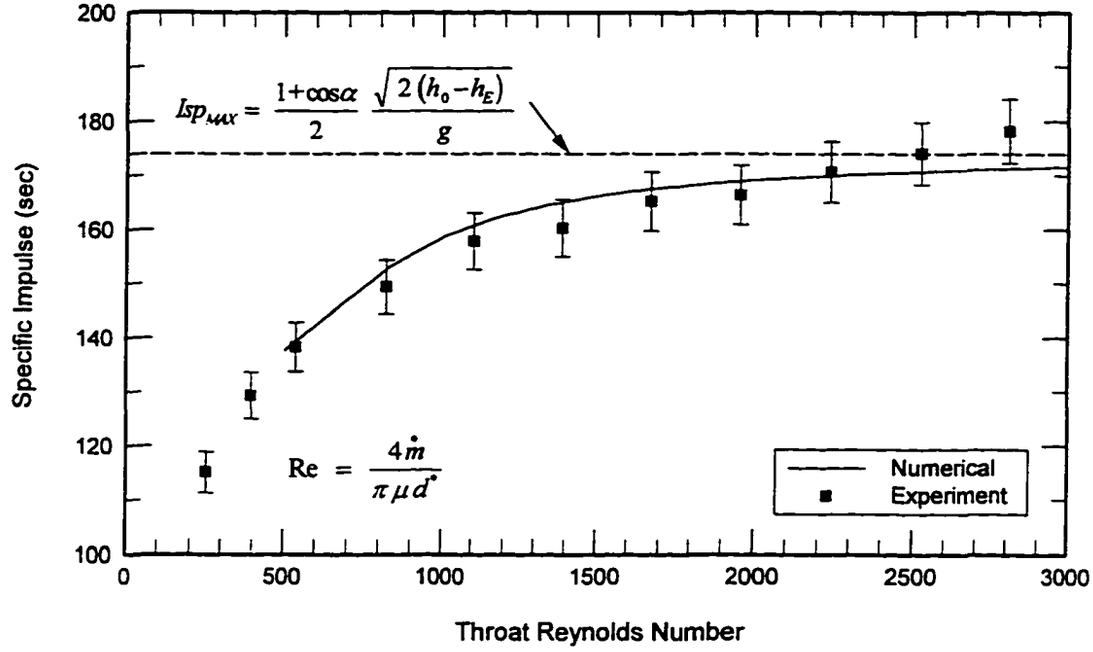

Fig. 4-1. Experimental versus numerical results with helium propellant at room temperature. The I_{SP} decreases at low *Re* due to viscous effects in the 230:1 nozzle.

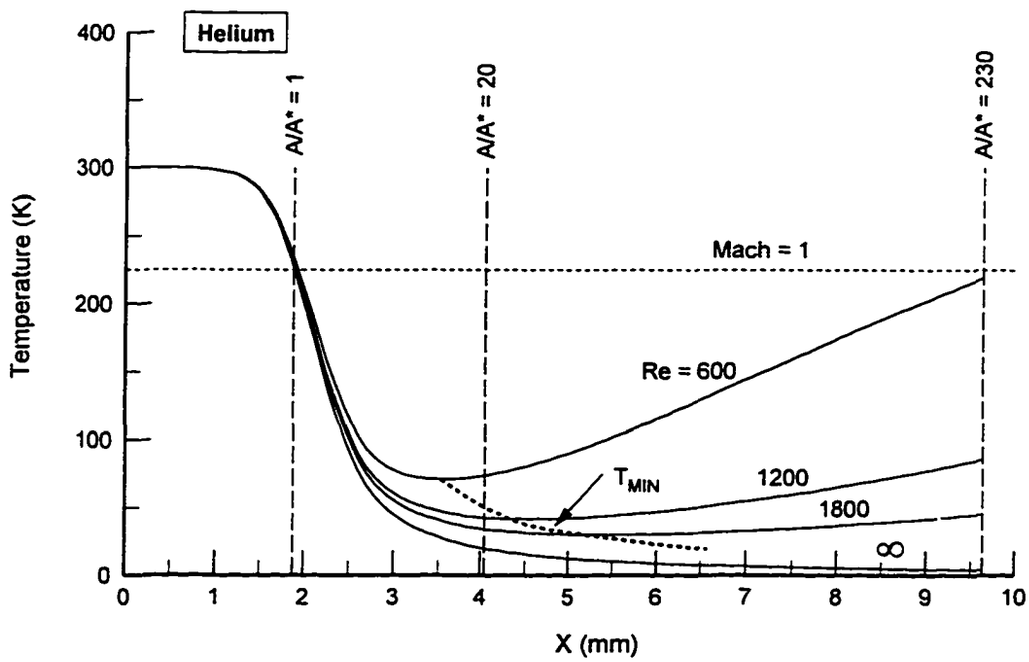

Fig. 4-2. Gas temperature versus axial location for different values of throat Reynolds number, from the quasi-1D numerical model. Throat diameter = 0.38 mm. Nozzle divergent half angle = 45 degrees, convergent half angle = 20 degrees.

4.2 General Operating Characteristics

The pulsed arcjet thrust, mass flow rate, voltage and pulse rate are measured throughout the duration of each performance test. The derived quantities of specific impulse, input power, and efficiency are calculated from these measurements using the following equations with the associated experimental uncertainties (see Section 2.6);

$$I_{SP} = \frac{T_{HR}}{g\dot{m}} \pm 3.3\ \% \tag{4.1}$$

$$P = \frac{1}{2} C V_B^2 PPS \pm 4.1\ \% \tag{4.2}$$

$$\eta = \frac{I_{SP_{HOT}}^2}{I_{SP_{COLD}}^2 + \frac{2P}{g^2 \dot{m}}} \pm 6.2\ \% \tag{4.3}$$

Fig. 4-3 shows data from a typical run. Since the mass flow rate is fixed, the I_{SP} is directly proportional to the thrust, and only the I_{SP} is plotted. The test procedure is to allow the mass flow rate to reach steady state with room temperature gas, which takes approximately 1-2 minutes, before applying power. In the first several seconds after power is applied, the thrust increases immediately with a proportional increase in I_{SP} of 10-60 seconds. This immediate jump in thrust is discussed in detail in Section 4.5, and is a useful measurement by itself because it allows the effects of different design parameters to be distinguished from the thermal characteristics of the arcjet. Following the initial increase, the thrust and specific impulse rise gradually as the arcjet heats up to steady-state temperature. The gradual thrust increase is related to the heat transfer characteristics and thermal design of the arcjet. With the thermal design of the NASA 1-kW arcjet, the pulsed arcjet requires a full 10-12 minutes to reach steady state at low power. A temperature measurement from a thermocouple mounted on the arcjet nozzle (Fig. 4-4) shows the time response of nozzle temperature corresponding to the thrust measurement (Fig. 4-3).

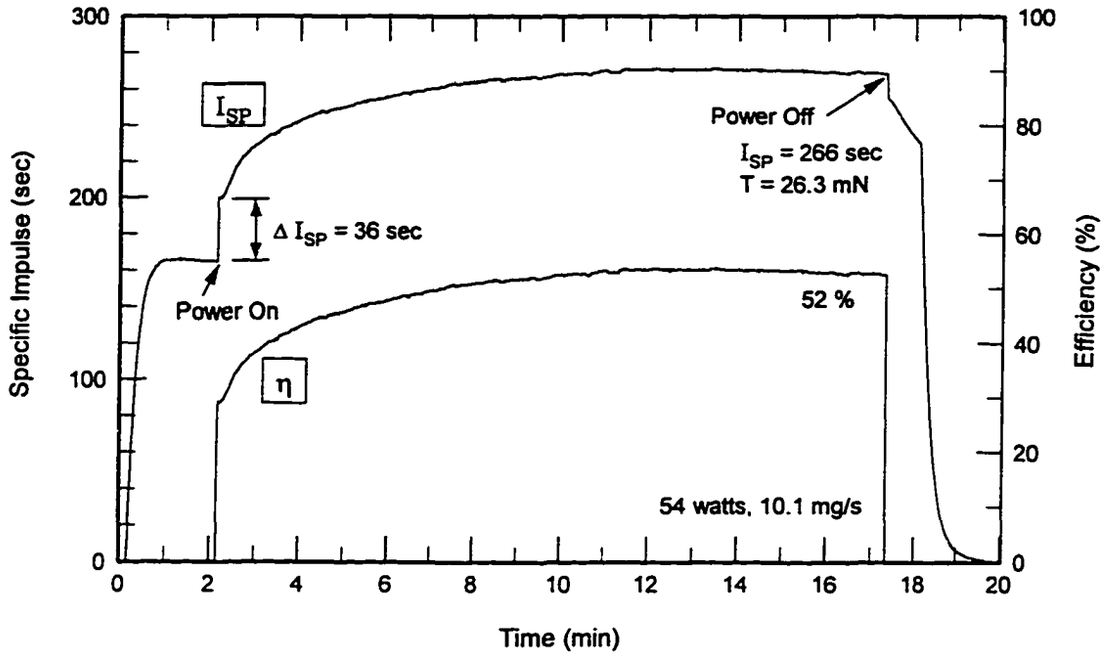

Fig. 4-3. Specific impulse and efficiency during a typical performance test. The initial thrust increase is followed by a gradual rise related to the pulsed arcjet thermal design.

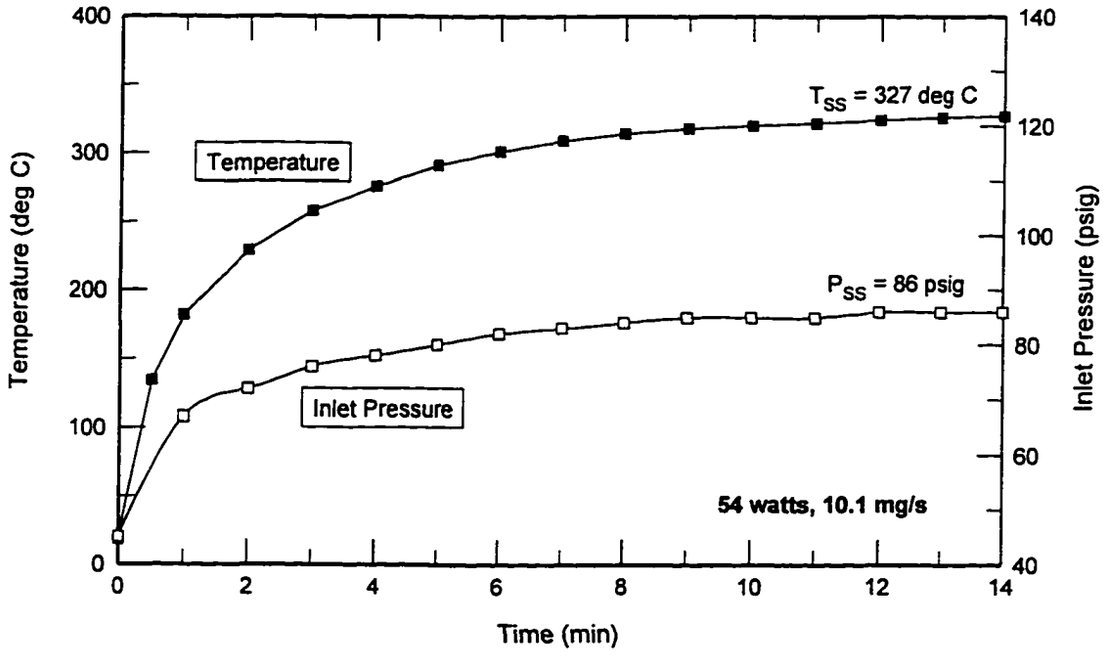

Fig. 4-4. Nozzle surface temperature and propellant inlet pressure during thruster warm-up to steady state at 54 watts.

The pulse rate and breakdown voltage are recorded during each performance run, as shown in Fig. 4-5. The pulse rate is maintained approximately constant during the duration of the test because it is set externally with the power suppy control circuit. The breakdown voltage decreases gradually during the first several minutes because the breakdown voltage depends on the gas number density in the capillary, which decreases as the thruster heats up. The data suggest a ~4 minute heatup for the capillary, versus 10-12 minutes for the nozzle. The decrease in breakdown voltage also causes a gradual decrease in the input power during warm-up. For the test shown in Fig. 4-5, the input power starts initially at 82 watts but decreases to 54 watts at steady state.

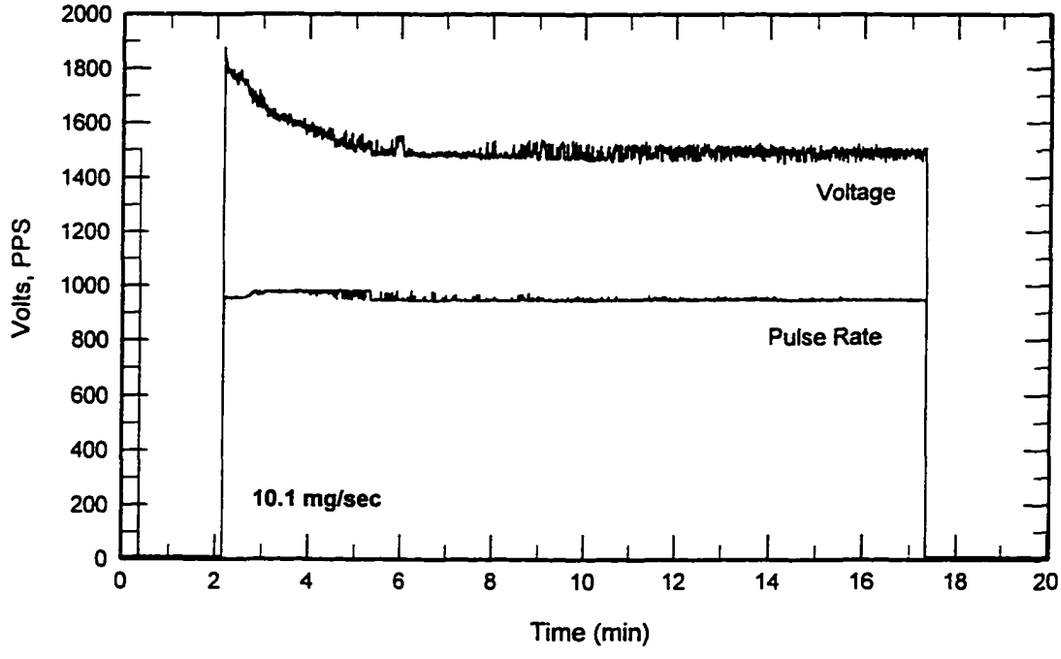

Fig. 4-5. Pulse rate and breakdown voltage during thruster operation. The pulse rate is held constant by the control circuitry. The breakdown voltage and thus input power decrease as the thruster heats up.

The design of the propellant feed system also influences the time required to reach steady state. Though the response time of the Unit Instruments mass flow controller is measured in seconds, a time lag (~1 minute) is introduced by the volume of feed system tubing between the flow controller and the arcjet. This time

lag has implications during thruster operation because the inlet pressure to maintain a specified mass flow rate increases as the thruster heats up. The time to steady state was adequate for the performance tests, though the propellant feed system and thruster response time could be improved by installation of appropriate flow control devices to isolate the effect of downstream pressure on the mass flow.

4.3 Measured Specific Impulse and Thrust Efficiency

Pulsed arcjet performance results are shown in Fig. 4-6 and Fig. 4-7 for helium propellant at two flow rates, 6.6 mg/sec and 10.1 mg/sec, and two nozzle area ratios, 20 and 230. The tests with the 20:1 nozzle were performed with a 7.5 mm long by 2.5 mm diameter capillary, while the tests with the 230:1 nozzle were run with a 12.5 mm long by 2.5 mm diameter capillary. At each of these four cases, the pulse rate is varied through 5-6 settings between 550 and 2630 pps for a total of 22 steady-state performance measurements (Table 4-1).

L (mm)	D (mm)	A/A*	m (mg/s)	V_B (volts)	PPS (pps)	Power (watts)	$P/\dot{m}$ (MJ/kg)	I_{SP} (sec)	η (%)
7.5	2.5	20	6.63	1270	582	23.9	3.61	213	46
7.5	2.5	20	6.63	1245	1002	39.6	5.97	239	39
7.5	2.5	20	6.63	1060	1551	44.4	6.70	257	40
7.5	2.5	20	6.63	1160	1880	64.5	9.73	278	34
7.5	2.5	20	6.63	1020	2192	58.2	8.77	275	37
7.5	2.5	20	6.63	1040	2630	72.5	10.94	293	34
7.5	2.5	20	10.10	2300	550	74.2	7.35	277	43
7.5	2.5	20	10.10	1490	950	53.8	5.32	266	52
7.5	2.5	20	10.10	1660	1420	99.8	9.88	300	39
7.5	2.5	20	10.10	1360	1840	86.8	8.59	289	41
7.5	2.5	20	10.10	1500	2070	118.8	11.76	313	36
7.5	2.5	20	10.10	1270	2545	104.7	10.36	305	38
12.5	2.5	230	6.63	1330	578	26.1	3.93	218	44
12.5	2.5	230	6.63	1280	1000	41.8	6.30	236	37
12.5	2.5	230	6.63	1150	1500	50.6	7.63	256	37
12.5	2.5	230	6.63	970	1800	43.2	6.51	260	40
12.5	2.5	230	6.63	1050	2200	61.9	9.33	276	36
12.5	2.5	230	10.10	1480	572	31.9	3.16	231	57
12.5	2.5	230	10.10	1380	980	47.6	4.71	253	50
12.5	2.5	230	10.10	1150	1850	62.4	6.18	280	42
12.5	2.5	230	10.10	1100	2200	67.9	6.72	295	43
12.5	2.5	230	10.10	1050	2600	73.1	7.24	296	38

Table 4-1. Pulsed arcjet performance at thermal steady state.

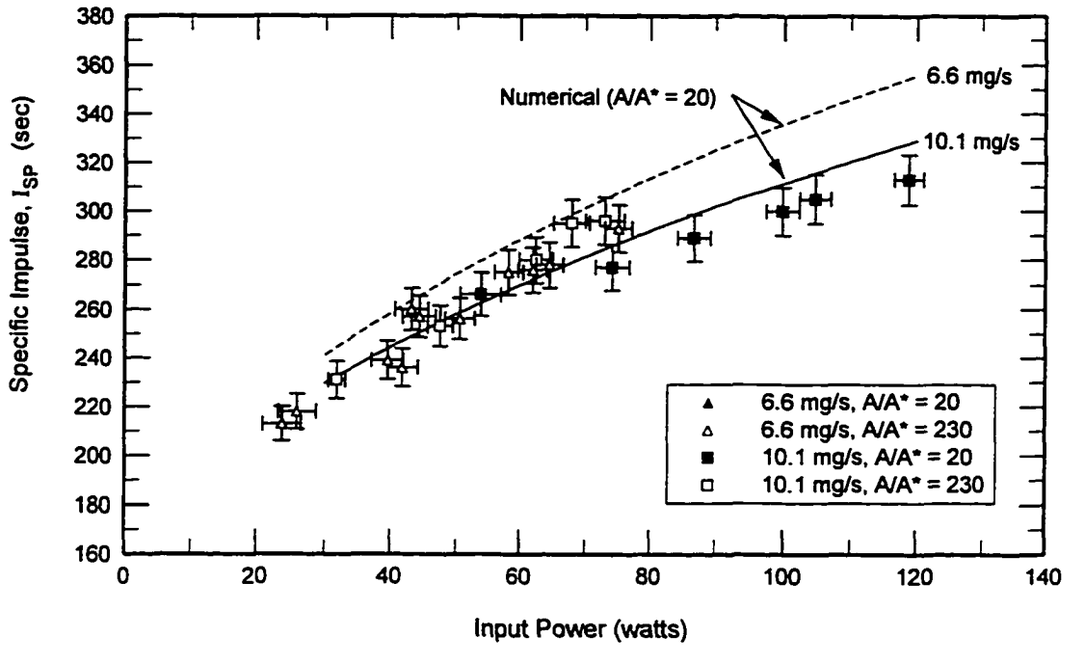

Fig. 4-6. Specific impulse versus input power for helium at two flow rates (6.6 mg/sec and 10.1 mg/sec) and two nozzle area ratios (20 and 230).

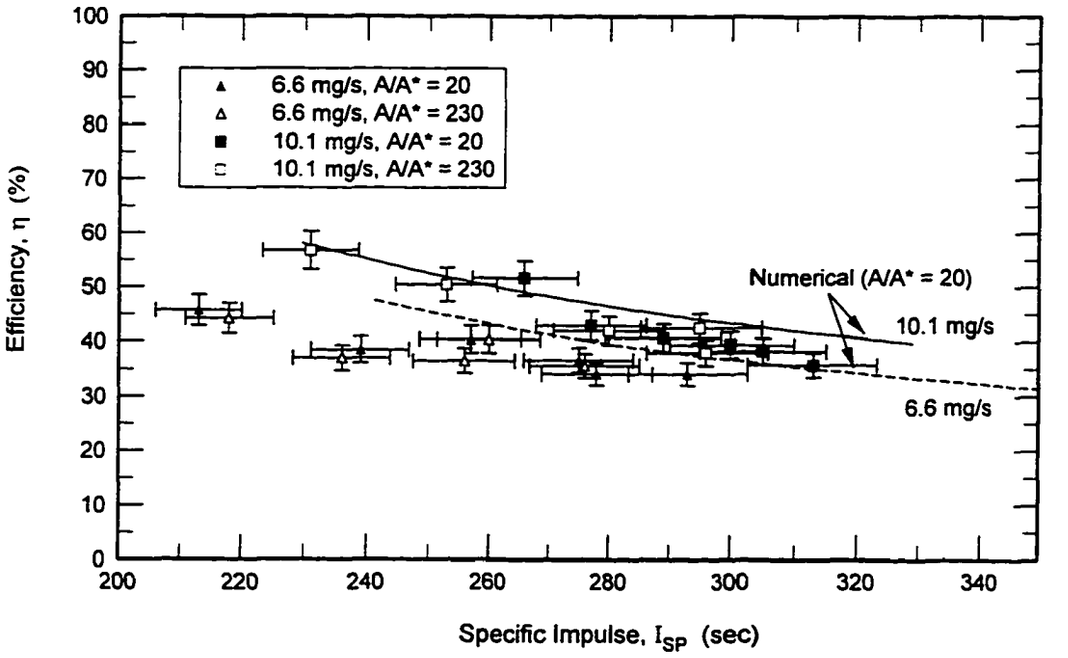

Fig. 4-7. Thrust efficiency versus specific impulse for helium. Increasing the mass flow rate shifts the performance curves upward.

The experimental data for I_{SP} follow approximately a single curve when plotted versus input power (Fig. 4-6), and differences due to mass flow rate and nozzle area ratio are within the experimental error. The solid and dashed lines in the graphs are the performance values predicted by the numerical model, which generally follow the experimental trends. The numerical results for the two nozzles are quantitatively similar at these conditions, and only the results for the 20:1 nozzle are shown. The numerical results indicate that decreasing the mass flow rate from 10 mg/sec to 6.6 mg/sec at fixed power level improves the I_{SP} by 5-10 seconds. The trend is reasonable because the average enthalpy of the gas is higher at the lower mass flow rate.

In Fig. 4-7 both the experimental data and numerical results show an upward shift in efficiency at higher flow rate. This trend is also a characteristic of other electrothermal devices, such as dc arcjets, and is generally attributed to frozen flow loss. However, for the pulsed arcjet running on helium propellant, the ionization losses are small. The efficiencies appear to be independent of area ratio, so the increase in I_{SP} at higher mass flow rates is not attributable to viscous effects. The efficiency trends are due to the heat transfer characteristics of the pulsed arcjet, where these energy losses are primarily in the capillary. The agreement of the numerical model with the experimental data is dependent on the value of the Nusselt number selected to calculate the heat transfer in the capillary. The sensitivity of the numerical results to the Nusselt number is shown in Fig. 4-8.

The mean thrust at thermal steady state depends on the nozzle temperature, and the nozzle temperature is coupled to the mass flow rate. Evaluating the sensitivity of I_{SP} due to mass flow rate from the experimental data is difficult because the mass flow rate trends are masked by the larger influence of the nozzle temperature. The numerical model is used to evaluate these effects independently, since the mass flow rate and wall temperature are specified as input parameters. When comparing the numerical model to the experimental data, an empirical relationship is used for the wall temperature boundary condition (Fig. 4-9). The nozzle temperature was obtained from a thermocouple measurement at thermal steady state. The data indicate that the wall temperature depends on the specific energy rather than the input power.

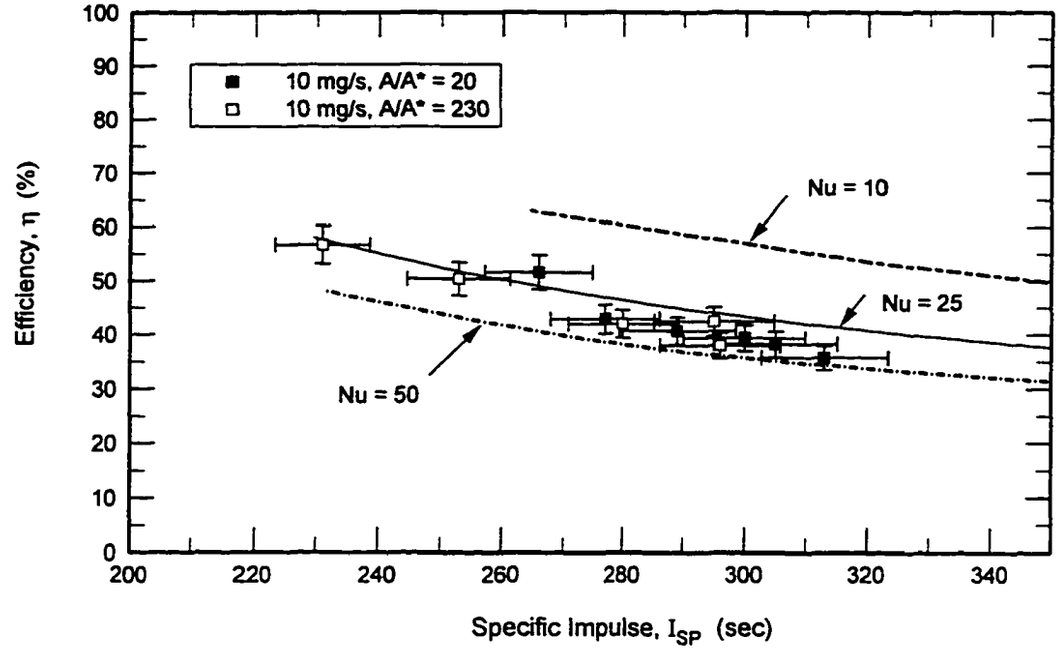

Fig. 4-8. Sensitivity of the numerical results to Nusselt number. Selecting Nu = 25 gives good agreement with the experimental data.

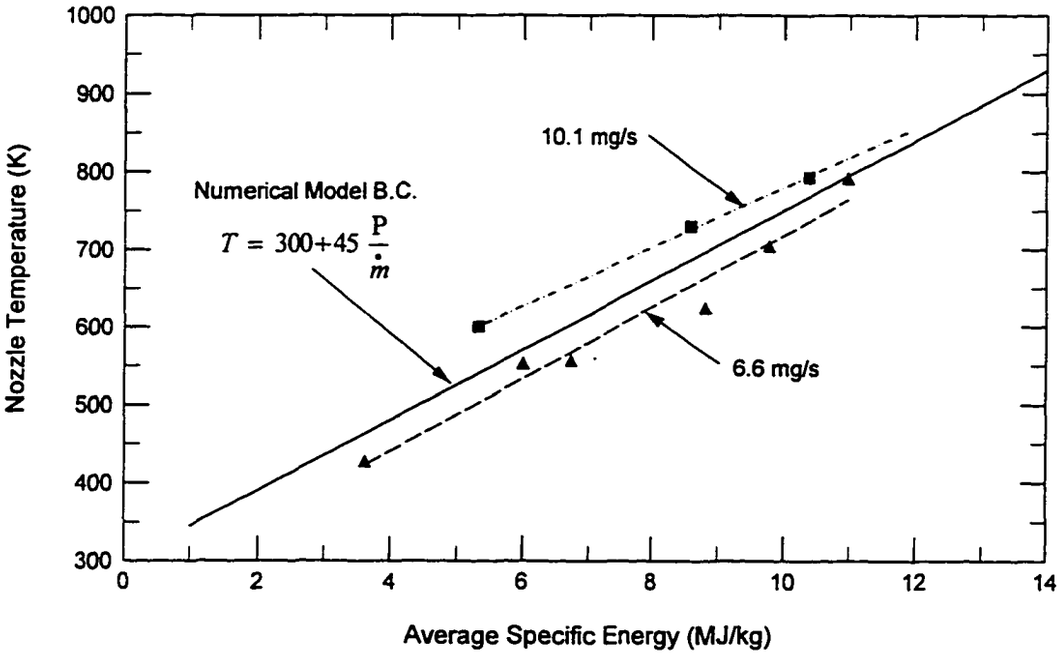

Fig. 4-9. Steady-state surface temperature of the 20:1 area ratio nozzle. The linear curve fit is used as a boundary condition in the numerical model.

4.4 Distribution of Energy Losses

The output from the numerical model includes a breakout of the individual energy losses from the categories described in Section 3.5. A typical distribution is shown in Fig. 4-10 for an 80 mJ pulse at 1500 pps. The dashed line represents the total input energy, which includes the internal energy of the inlet gas. For this case, the combined losses of heat transfer in the nozzle, frozen flow and divergence losses are only 1.5 + 4.6 = 6.1% of the total input energy. Capillary heat transfer is by far the dominant loss mechanism, accounting for more than half the total input energy. Clearly, this indicates that additional work on improving the pulsed arcjet performance should focus on decreasing the heat transfer in the subsonic region.

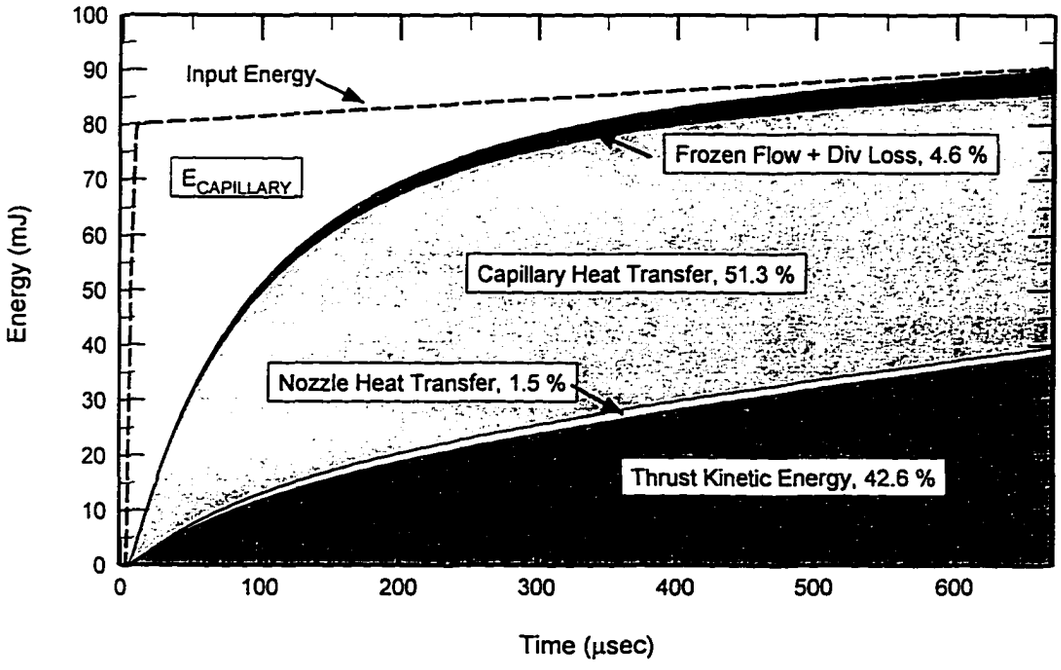

Fig. 4-10. Distribution of energy losses for an 80 mJ pulse at 1500 pps. Heat transfer losses in the capillary account for more than half the energy.

4.5 Efficiency with Cold Wall Boundary Conditions

A general operating characteristic of the pulsed arcjet is that applying power to the thruster produces an immediate thrust increase due to direct arc heating, followed by a further increase due to wall heating. As the thruster heats up, heat transfer losses from the gas to the capillary and nozzle walls decrease, and the

performance improves. The thermal design of the arcjet has a large effect on the overall thruster performance, but it is useful to separate the effect of wall temperature in order to evaluate other variables experimentally. This can be done by examining the magnitude of the initial thrust increase under different operating conditions. The initial thrust increase is shown in the "Power On' point in Fig. 4-3.

In the first set of tests, eight different arcjet configurations were evaluated at a fixed mass flow rate (6.6 mg/sec) to examine the effects of the parameters L, D, A/A* and capacitance (or pulse energy). In the second set of tests, five mass flow rates were tested with a fixed arcjet configuration. For each run, the thruster was operated for approximately 5-10 seconds, and the power was then turned off to keep the thruster close to the initial ambient temperature. The change in thrust and specific impulse was measured, and an equivalent efficiency was calculated from,

$$\eta = \frac{\left(Isp_{COLD} + \frac{\Delta T_{HR}}{g\dot{m}} \right)^2}{Isp_{COLD}^2 + \left(\frac{2P}{g^2 \dot{m}} \right)} \tag{4.4}$$

The above expression is derived from Eq. 4.3, where I_{SPHOT} is replaced by $I_{SPCOLD} + \Delta I_{SP}$. The experimental data for the first set of tests at a fixed mass flow rate are shown in Fig. 4-11. The efficiencies approximately follow a single curve when plotted versus input power, and the effects of the four design variables (area ratio, capacitance, capillary length and diameter) are relatively unimportant. For example, doubling the pulse energy by changing the capacitor from 0.05 μF to 0.10 μF while keeping input power constant does not produce a significant change in the cold wall efficiency. The thrust efficiencies for the pulsed arcjet at thermal steady state are shown on the same plot for comparison. The large upward shift in efficiency from the cold wall condition to thermal steady state shows the dominant effect of wall temperature on the arcjet performance.

In the second set of tests, the arcjet used a 7.5 x 2.5 mm capillary and the 0.05 μF capacitor, and both nozzles were tested. At each mass flow rate (4.92, 6.64, 8.35, 10.1, and 11.8 mg/sec), thrust measurements were obtained over a series of

eight pulse rates for a total of 80 test conditions. The five cold wall efficiency curves are shown in Fig. 4-12. At a given power level, the efficiency increases with increasing mass flow rate, while the effect of nozzle area ratio is negligible. These trends indicate that frictional effects for these conditions are minor compared to the influence of heat transfer.

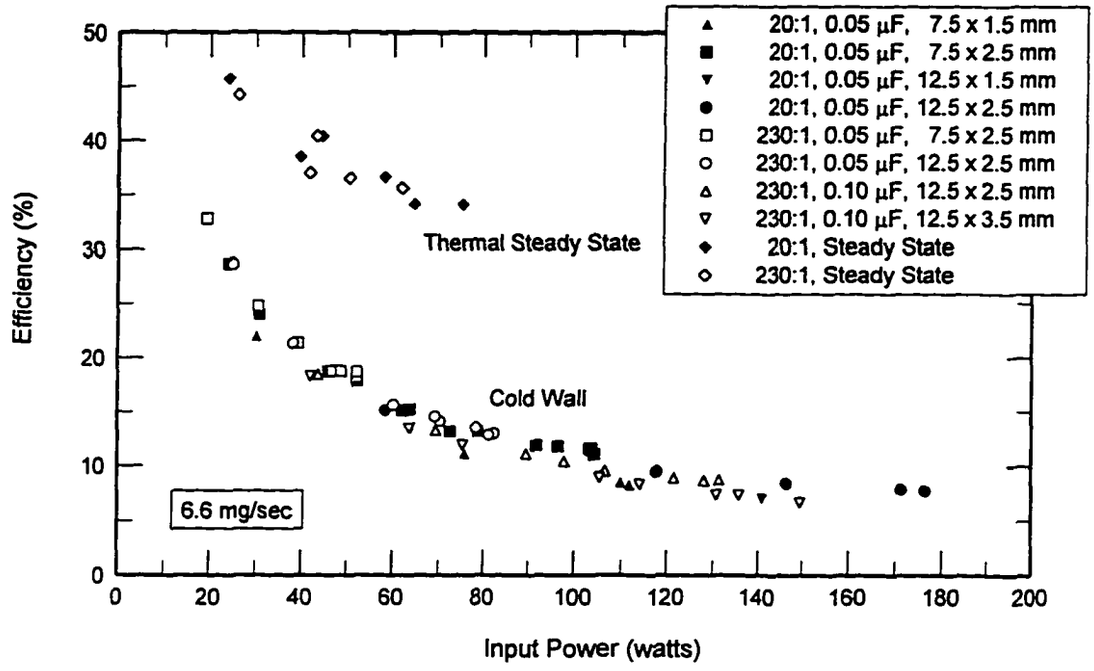

Fig. 4-11. Pulsed arcjet efficiency with cold wall boundary conditions compared to thermal steady state. The cold wall efficiency is primarily a function of input power.

Experimental efficiencies for conventional dc arcjets are often plotted versus the specific energy, rather than input power because a series of curves at different mass flow rates tends to collapse to a single curve when plotted versus specific energy. This is convenient because two variables, power and mass flow rate, can be replaced by a single variable, specific energy. In the dc arcjet, the specific energy is closely related to the average propellant enthalpy, which is in turn related to the gas temperature. In the pulsed arcjet, the gas properties vary continuously during an individual pulse. The parameter $P/\dot{m}$ is therefore an average specific energy that is not as directly related to the propellant enthalpy and gas temperature; however, when this substitution is applied to the pulsed arcjet data, the efficiency curves also collapse to a single curve (Fig. 4-13).

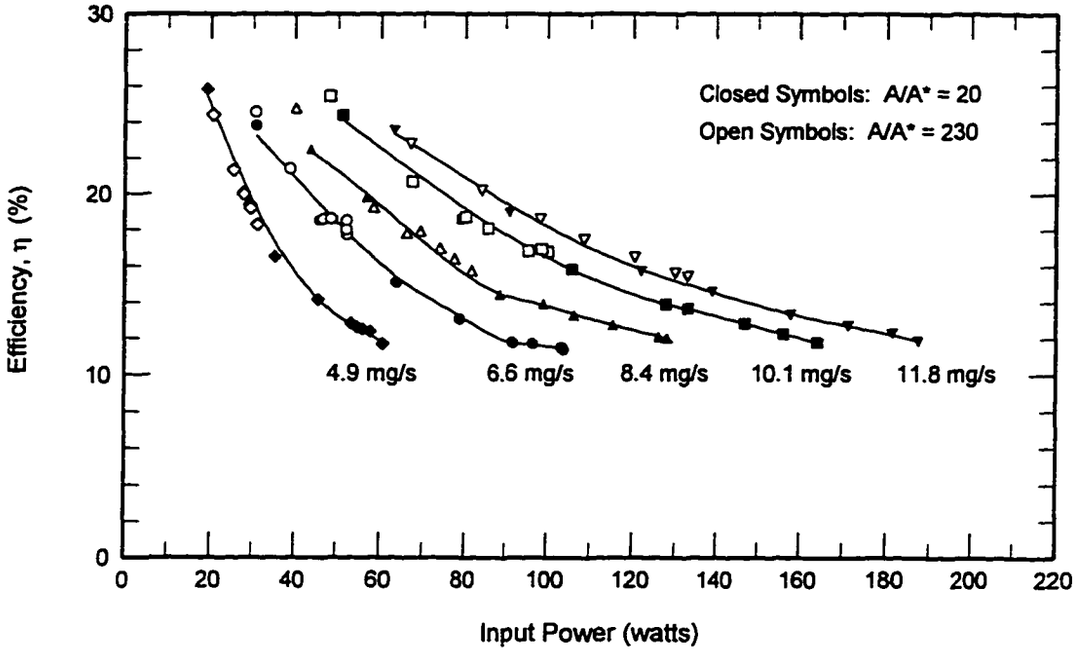

Fig. 4-12. Pulsed arcjet efficiency versus input power showing the effect of mass flow rate. The effect of area ratio on efficiency is negligible at these operating conditions.

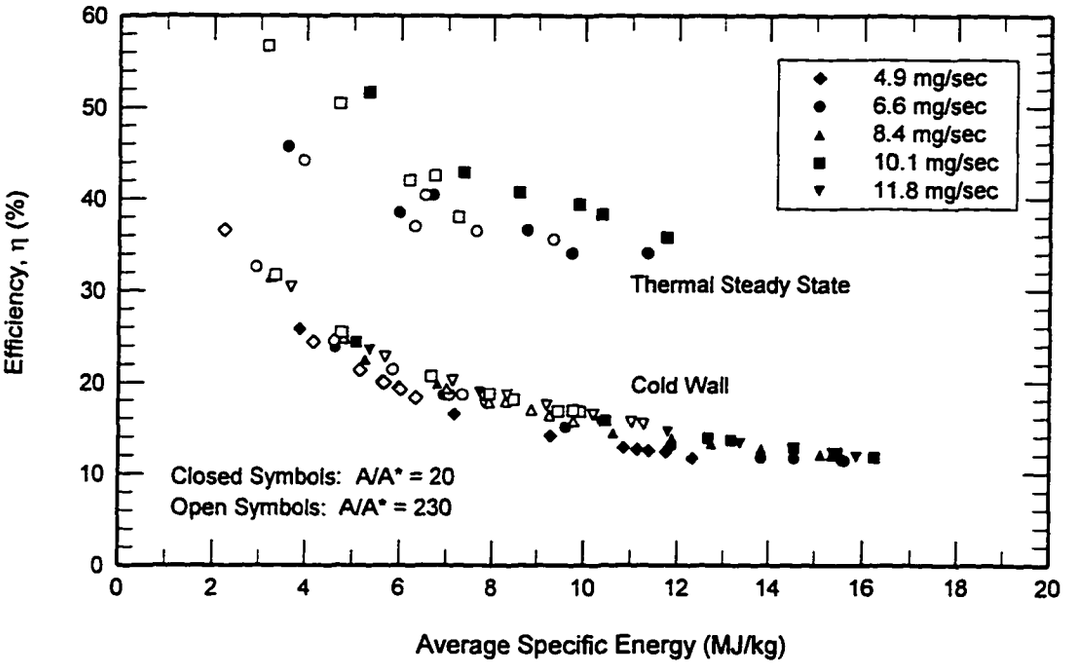

Fig. 4-13. The cold wall efficiencies from Fig. 4-12 collapse to a single curve when plotted versus the average specific energy and are independent of area ratio.

4.5.1 Numerical Results for Cold Wall Efficiency

The results from the numerical model can be compared to the experimental data for cold wall efficiency with a minor correction to the experimental data. The cold efficiencies shown in Fig. 4-11 to Fig. 4-13 are calculated from Eq. 4.4 assuming that the mass flow rate in the pulsed arcjet is equal to the setting of the Unit Instruments flow controller. However, the mass flow through the thruster is established by the pressure in the propellant feedline just upstream of the cathode orifice. The propellant feed pressure that is established by the flow controllers for cold flow is less than the feed pressure required when the thruster is running. At the switch-on of power, a time lag is introduced by the feed system volume such that the actual mass flow rate is less than the flow controller setting during a transient period after power is applied. Thus, the calculation of the experimental cold wall efficiency must be made with a corrected mass flow rate. The numerical model itself does not require a correction because the mass flow is calculated based on the pressure difference across the cathode orifice.

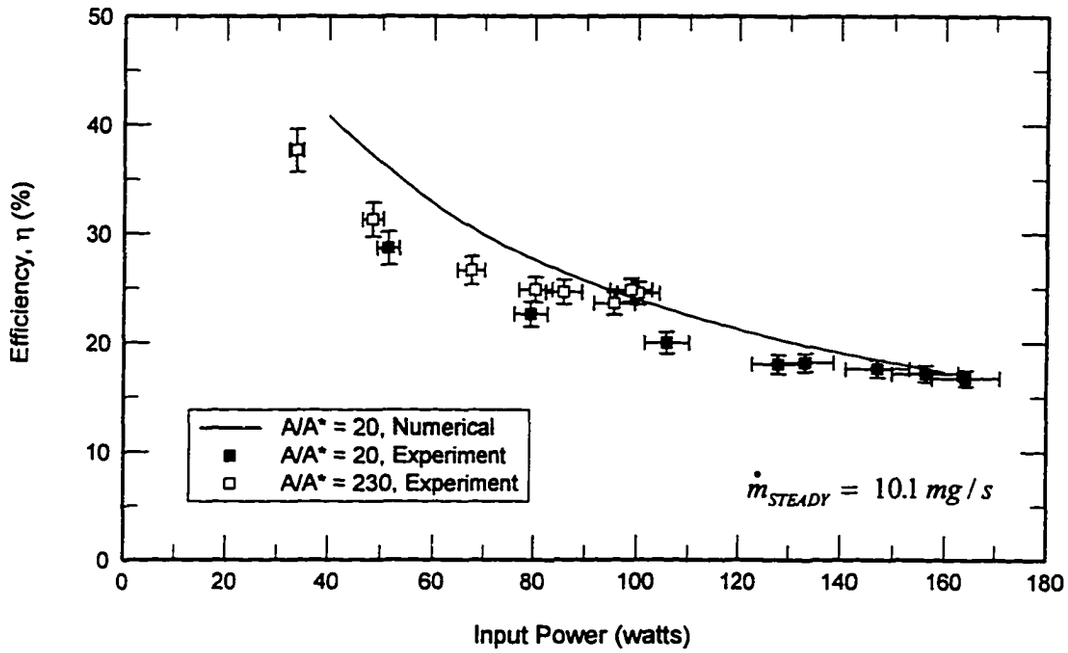

Fig. 4-14. Comparison of the corrected experimental cold wall efficiency compared with the numerical model. The efficiency is independent of area ratio.

The numerical model is used to determine a correction to the experimental data. For the data shown in Fig. 4-14, the mass flow rate used to calculate the cold wall efficiency is,

$$\dot{m}_{CORRECTED} = 9.345 - 9.96\times10^{-4}(PPS) + 9.71\times10^{-8}(PPS)^2 \quad [kg/s] \quad (4.5)$$

Equation 4.6 is only applicable to this particular case, and a general expression for the mass flow correction has not been developed. The corrected mass flow rates are approximately 10-30 percent lower than the original steady mass flow rate.

4.6 The Effect of Pulse Rate on Breakdown Voltage

An additional consideration in designing a pulsed arcjet involves the dependence of the breakdown voltage on pulse rate. If the time between pulses is much greater than the characteristic reservoir blowdown time for the capillary, the breakdown voltage is independent of the pulse rate. However, at the operating conditions tested, the pulse rate is slightly faster than the reservoir blowdown time, and the pressure and number density in the capillary do not have time to return to their initial steady flow states before the next pulse occurs. This situation is reflected in the experimental data (Fig. 4-15), where the breakdown voltage decreases as the pulse frequency is increased. The numerical model also correctly predicts this variation of breakdown voltage with pulse rate. The calculation is straight-forward: from the pressure and temperature at the beginning of a pulse, the model calculates the number density, allowing the theoretical breakdown voltage to be calculated from the Paschen curve for helium for plane parallel electrodes.

The numerical results match the experimental data extremely well, as shown in Fig. 4-14 for mass flow rates of 6.6 and 10.1 mg/sec. The agreement indicates that voltage breakdown is not affected by the dielectric wall of the capillary. The decrease in breakdown voltage with pulse rate has an effect on the input power to the thruster. If the pulse rate did not affect the breakdown voltage, doubling the pulse rate would also double the input power. For the experiment, the input power increase (Fig. 4-16) is less than a factor of two because of the accompanying decrease in breakdown voltage.

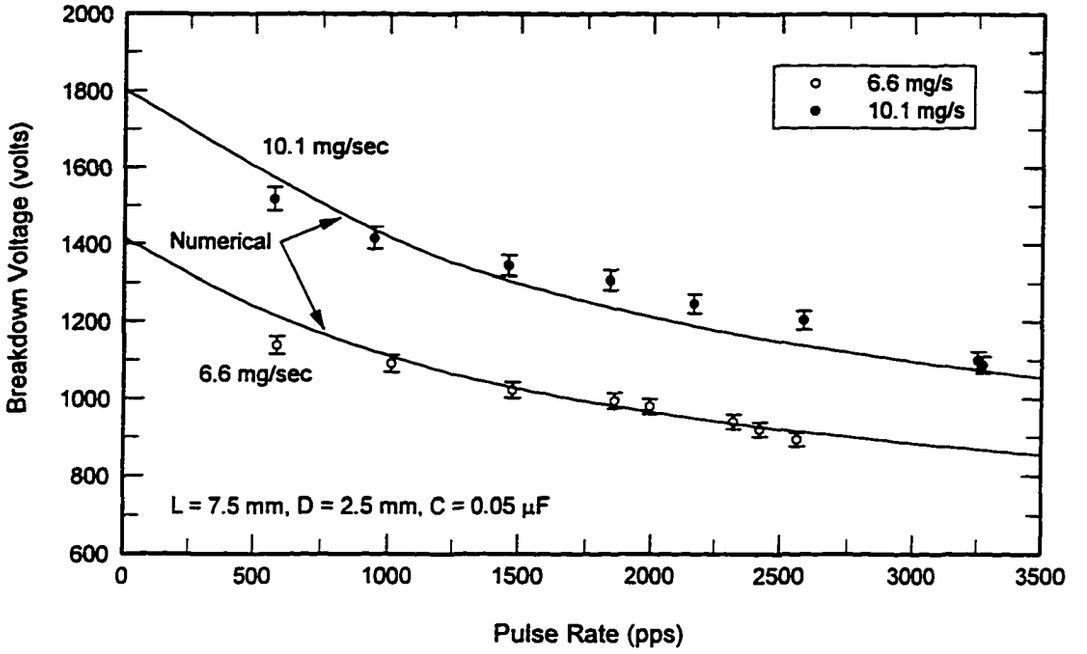

Fig. 4-15. Breakdown voltage for a range of pulse rates. The numerical model gives the calculated breakdown voltage from Eq. 5.4.

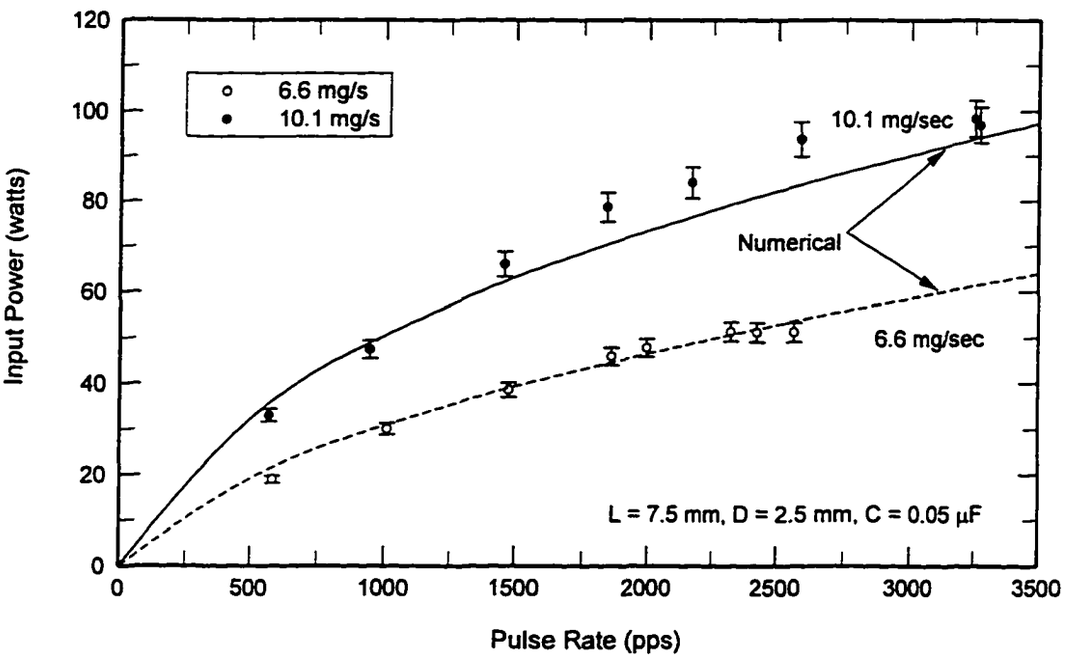

Fig. 4-16. Effect of pulse rate on input power. Input power does not increase linearly with pulse rate because the breakdown voltage decreases simultaneously.

4.7 Single Probe Measurement

The pulsed arcjet exhaust flow was investigated by placing relatively simple diagnostic single probes in the arcjet plume. The results of this experiment (Fig. 4-17) show that the electron number density in the plume is high enough to produce a strong readable signal on the probes. The first probe, located 1 mm from the exit plane of the 230:1 nozzle and approximately 7.8 mm downstream of the capillary, shows a signal beginning ~3 μsec after the start of the arc discharge. The second probe, located 17 mm downstream from the first probe, also provided a relatively clean signal. The peaks of the two probe signals can be used to estimate the flow velocity, which is 7100 m/s in this case. This measurement was performed primarily to demonstrate the feasibility of using single probes in the pulsed arcjet plume. A considerable amount of experimental refinement and analysis would be required to produce useful time-of-flight data or quantitative data on electron number density.

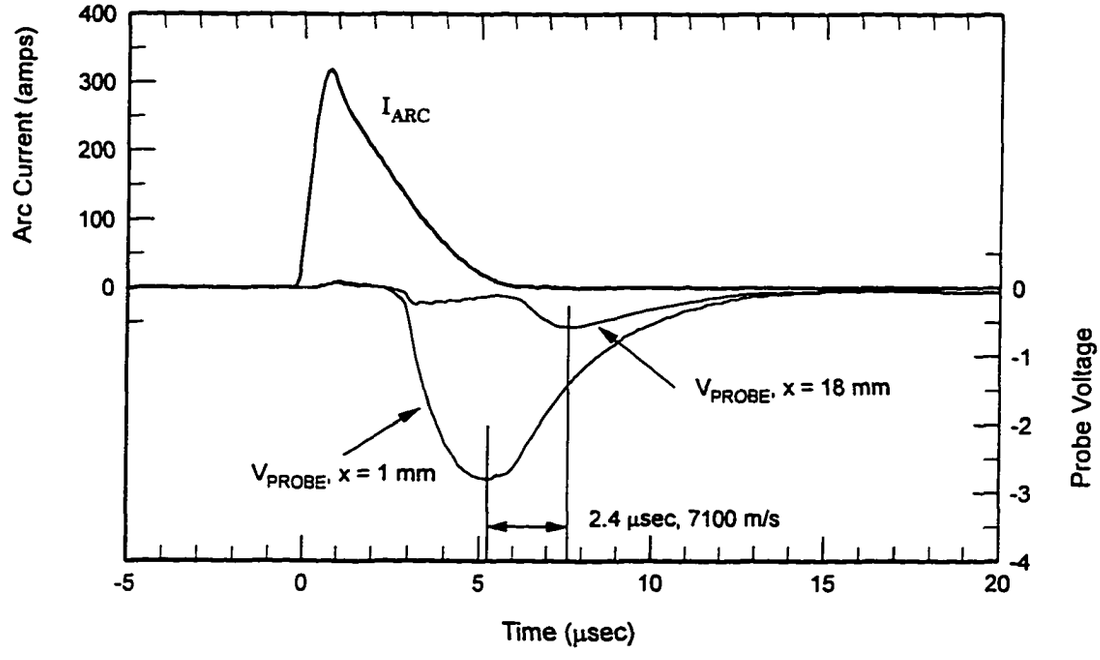

Fig. 4-17. Experimental probe voltage for two single probes located 1.7 cm apart. The signal peaks indicate an approximate flow velocity of 7100 m/s.

4.8 Numerical Study of Design Parameters

The numerical model is used to investigate the effects of the individual thruster design variables. The performance of a baseline thruster geometry and operating point is calculated, and then different design inputs are changed individually to compare the change in specific impulse and thrust efficiency. The 6 design variables and 5 operating point variables are listed in Table 4-2 along with their initial values and the baseline performance.

Baseline	Nozzle area ratio	A/A*	20	
Design	Nozzle half angle	α	20	[deg]
Variables	Capillary length	L	7.5	[mm]
	Capillary diameter	D	2.5	[mm]
	Throat diameter	d*	0.38	[mm]
	Circuit external inductance	L_{EXT}	2.9	[μH]
Operating	Mass flow rate	$\dot{m}$	10	[mg/s]
Conditions	Pulse rate	PPS	3000	[pps]
	Pulse energy	E	40	[mJ]
	Wall temperature	T_{WALL}	1000	[deg K]
	Inlet gas temperature	T_{GAS}	300	[deg K]
Calculated	Specific impulse	I_{SP}	346	[sec]
Performance	Efficiency	η	43.4	[%]

Table 4-2. Baseline parameters for numerical study of pulsed arcjet performance.

4.8.1 Nozzle Parameters

Under certain conditions, viscous effects in the pulsed arcjet can be important. The cold flow results show that friction can significantly decelerate the flow at low Reynolds numbers for large area ratio nozzles. The pulsed arcjet performance is calculated with the numerical model for three nozzle area ratios (4, 20, and 230) and two nozzle half angles (20, 30 degrees) over a range of specific energies. The specific energy is varied by setting the input power constant at 120 watts and changing the propellant flow rate. At constant power, the average specific energy various roughly with the inverse of the throat Reynolds number, so

that increasing the specific energy can be expected to increase viscous effects in the nozzle.

Numerical results are shown in Fig. 4-18 and Fig. 4-19. For specific energies less than approximately 10 MJ/kg, the I_{SP} is highest for the 230:1 nozzle, with a gain of 10-15 seconds over the 4:1 nozzle. Viscous losses are relatively low in this regime, and the performance improves with larger area ratios due to the additional expansion of the gas. The specific impulses for the 20:1 and 230:1 nozzles are similar at low specific energy. This result is consistent with the steady state experimental results where the specific energies are less than 11 MJ/kg, and the I_{SP} is similar for the two nozzles. The numerical results indicate that the specific impulse for the 230:1 nozzle decreases rapidly due to viscous effects at specific energies above 10 MJ/kg, with the exit Mach number decreasing to unity at 18 MJ/kg. As shown in Fig. 4-18, the 20:1 nozzle maintains the best I_{SP} between 11 and 33 MJ/kg. The 4:1 nozzle suffers a performance penalty below 33 MJ/kg because the gas is not fully expanded. For a given power level - in this case 120 watts - the I_{SP} versus specific energy plot can be used to determine the optimum value of the mass flow rate, and the efficiency versus I_{SP} plot can be used to select the optimum nozzle design based on tradeoffs between specific impulse and thrust efficiency.

The two nozzle half angles investigated numerically are 20 degrees and 30 degrees, both for the 230:1 nozzle. At high Reynolds numbers with low friction, the 20 degree nozzle has a higher specific impulse than the 30 degree nozzle due to lower divergence loss, where the cosine loss factor is 3.0% compared to 6.7%. As the specific energy increases, viscous losses become more pronounced, and the 30 degree nozzle gives higher specific impulse because viscous effects outweigh the flow divergence penalty. The 30 degree half angle nozzle has a higher specific impulse for specific energies above 15 MJ/kg.

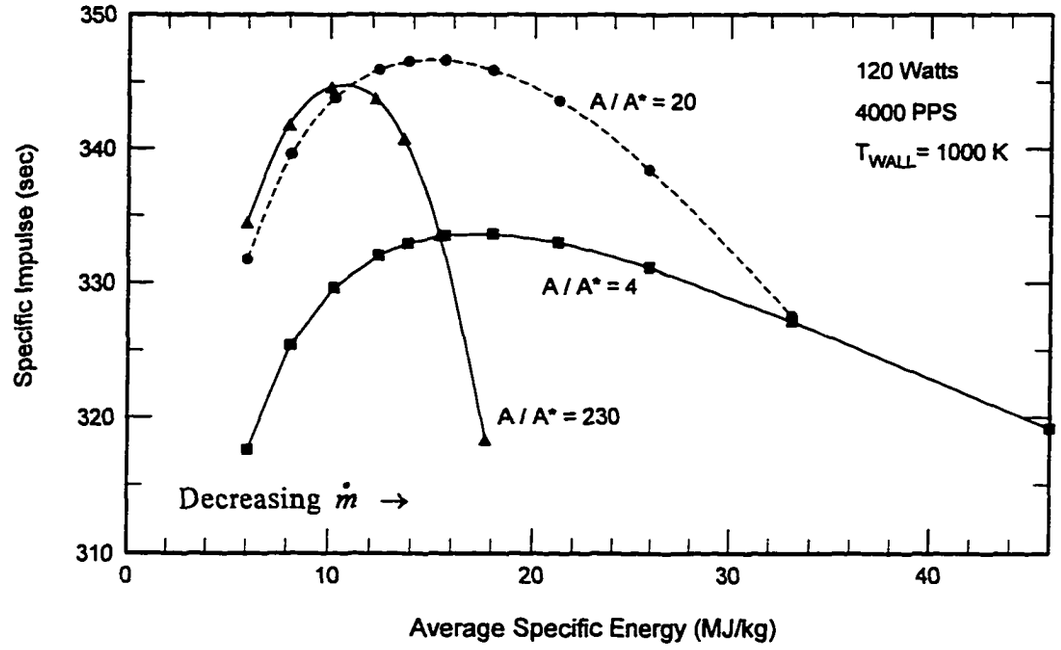

Fig. 4-18. Specific impulse versus average specific energy for three nozzle area ratios.

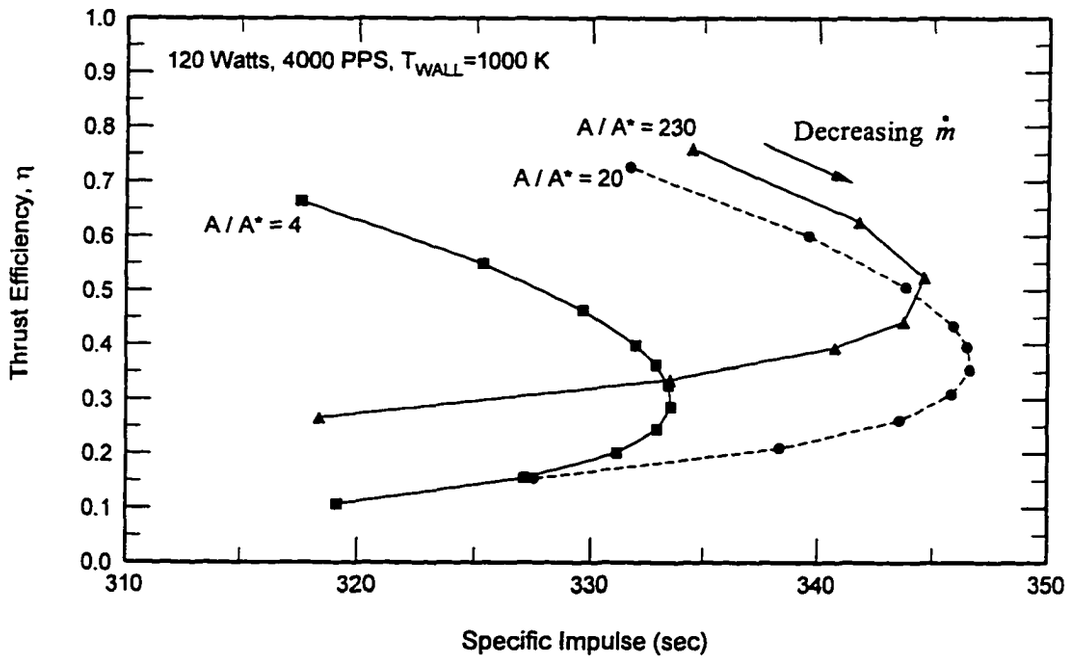

Fig. 4-19. Thrust efficiency versus average specific energy for three nozzle area ratios.

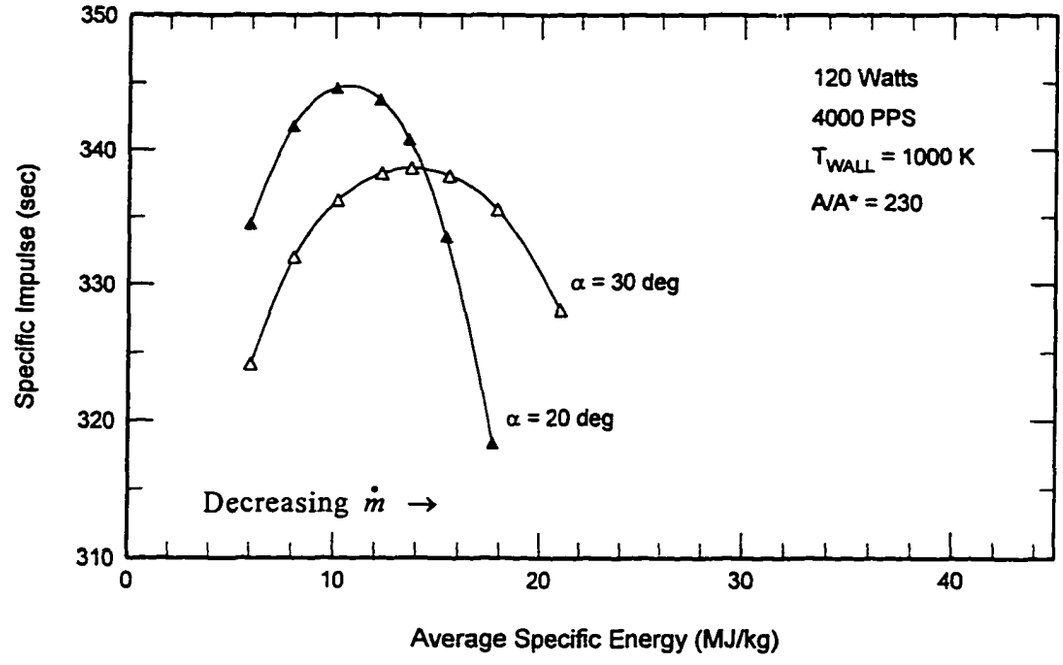

Fig. 4-20. Specific impulse versus average specific energy for two nozzle half angles. The performance results are a tradeoff between flow divergence loss and viscous loss.

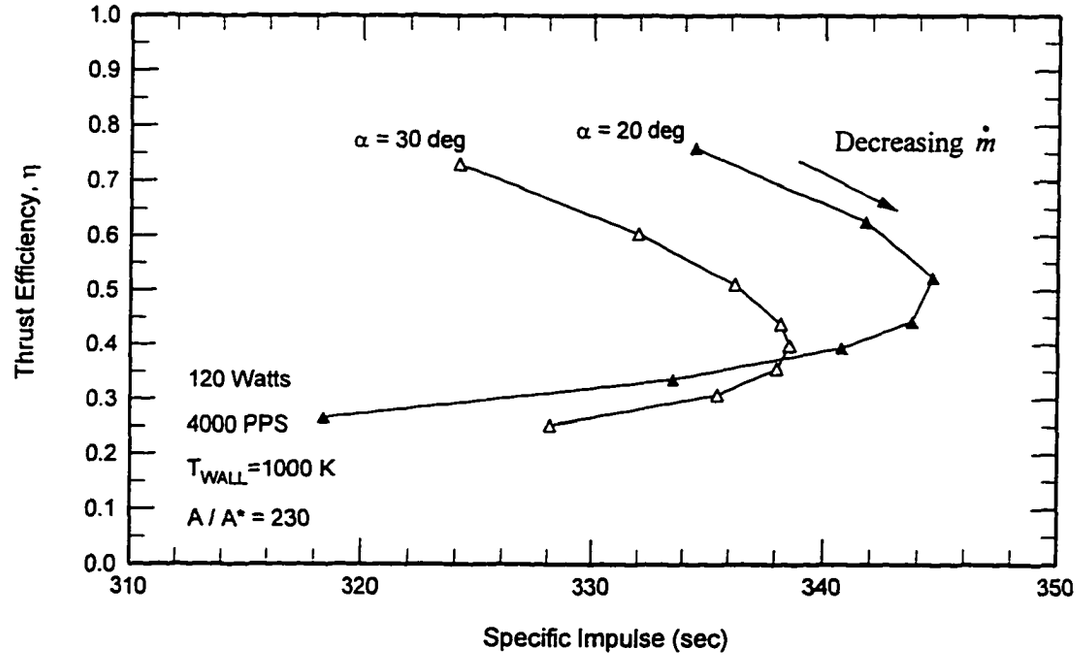

Fig. 4-21. Thrust efficiency versus specific impulse for two nozzle half angles.

4.8.2 Capillary Geometry, Throat Area, and Circuit Inductance

Both the steady state performance data and the cold wall efficiency data show minimal impact on arcjet performance related to changes in capillary length and diameter. The effects of nozzle throat diameter and circuit inductance were not investigated experimentally. These four design variables are studied numerically, and the results are shown in Table 4-3 and Fig. 4-22. These cases are at a fixed power of 120 watts, 10 mg/sec mass flow rate, and a 1000 K wall temperature.

The numerical results for the capillary length show a small improvement in performance for short capillaries, where the I_{SP} increases 18 seconds by decreasing the capillary length from 12.5 mm to 5.0 mm. The smaller surface area inside the shorter capillary reduces the heat transfer loss, and hence, both the I_{SP} and efficiency improve. The capillary diameter has a smaller impact on the arcjet performance than the capillary length. The maximum range of specific impulse and efficiency are only 7 seconds and 1 percent, respectively. Interestingly, the capillary diameter exhibits a maximum I_{SP} for capillary diameters of approximately 2.5 to 3.0 mm, within the range explored experimentally. The numerical model indicates that the pulsed arcjet performance is relatively insensitive to nozzle throat diameter, though the tradeoff between reservoir blowdown time and heat transfer time appears to favor smaller throat diameters somewhat.

Numerically, the circuit inductance was varied over two orders of magnitude (2.9 μH, 29 μH and 290 μH) with changes in the pulse width from 6.3 μsec to 50 μsec. The corresponding peak powers are 18.4 kW, 5.4 kW, and 1.7 kW. As shown in Fig. 4-22, the peak thrust decreases as the energy addition to the propellant is distributed over a longer time period. The total impulse is basically unchanged for a two order of magnitude change in the circuit inductance, a factor of eight change in the pulse time, and a factor of eleven change in the peak power. Further, since the total impulse is unchanged, both the specific impulse and the efficiency also remain unchanged. While the circuit inductance is an important parameter with regard to the external circuit efficiency (see Chapter 5), it is not a critical parameter for the pulsed arcjet performance. In addition, an apparent conclusion from this analysis is that high peak power levels are neither an advantage nor a disadvantage of the pulsed arcjet under these conditions.

L (mm)	D (mm)	d* (mm)	I_{SP} (sec)	η (%)
7.5	2.5	0.38	345.1	43.4
5.0	2.5	0.38	+8.7	+2.5
10.0	2.5	0.38	-5.8	-1.5
12.5	2.5	0.38	-9.9	-2.6
7.5	1.5	0.38	-6.5	-0.7
7.5	2.0	0.38	-2.2	-0.2
7.5	3.0	0.38	+0.1	+0.2
7.5	3.5	0.38	-0.1	+0.4
7.5	2.5	0.30	+1.4	+0.6
7.5	2.5	0.45	-3.5	-0.7
7.5	2.5	0.52	-6.8	-1.5
7.5	2.5	0.60	-11.1	-2.3

Table 4-3. Effect of capillary parameters and nozzle throat diameter compared to the baseline arcjet performance at 120 watts.

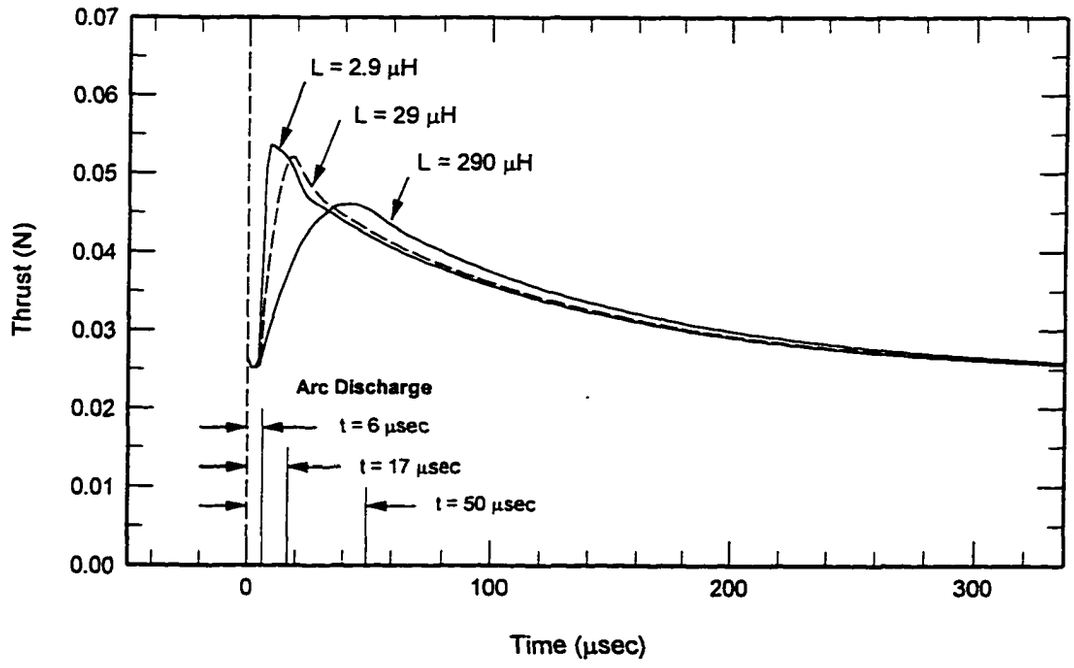

Fig. 4-22. The circuit inductance changes the magnitude and time of the peak thrust, but has negligible influence on the impulse bit.

Inductance (μH)	Peak Thrust (mN)	Arc time (μsec)	Impulse-Bit (μN-sec)
2.9	53.6	6.3	10.96
29	52.1	16.7	10.97
290	46.1	49.7	11.00

Table 4-4. Impulse-bit for three values of circuit inductance, L = 2.9, 29, and 290 μH.

4.8.3 Pulse Rate and Pulse Energy

One question with regard to the pulsed arcjet operating point is whether the performance is better with high pulse rates and low pulse energies or with low pulse rates and high pulse energies. The performance is calculated with the numerical model for 120 watts input power and 12 MJ/kg average specific energy comparing 80 mJ pulses at 1500 pps versus 40 mJ pulses at 3000 pps. The peak thrust is 81 mN for the 80 mJ pulse compared to 54 mN for the 40 mJ pulse, but the integrals under the two thrust curves, i.e. the impulse bits, differ by less than 1 percent, as shown in Fig. 4-23.

A second question involves the scaling relationship of input power on arcjet performance. Numerical results are shown in Fig. 4-24 for power levels in the range of 50 to 300 watts under two operating scenarios. In the first scenario, the pulse energy is fixed at 50 mJ for pulse rates of 1000, 2000, 3000, 4000, 5000, and 6000 pulses-per-second. In the second scenario, the pulse rate is fixed at 4000 pps, and the pulse energy is set to 12.5, 25, 37.5, 50, 67.5, and 75 mJ. The wall temperature is constant at 1000 K, and the mass flow rate is set to keep the average specific energy constant at 12 MJ/kg. The results indicate that the performance scales significantly with input power and mass flow rate at fixed specific energy. At the low power end, operating at 4000 pps with 12.5 mJ pulse energy provides a few additional seconds in I_{SP} over the case with 1000 pps and 50 mJ pulse energy, though this is a fairly small improvement.

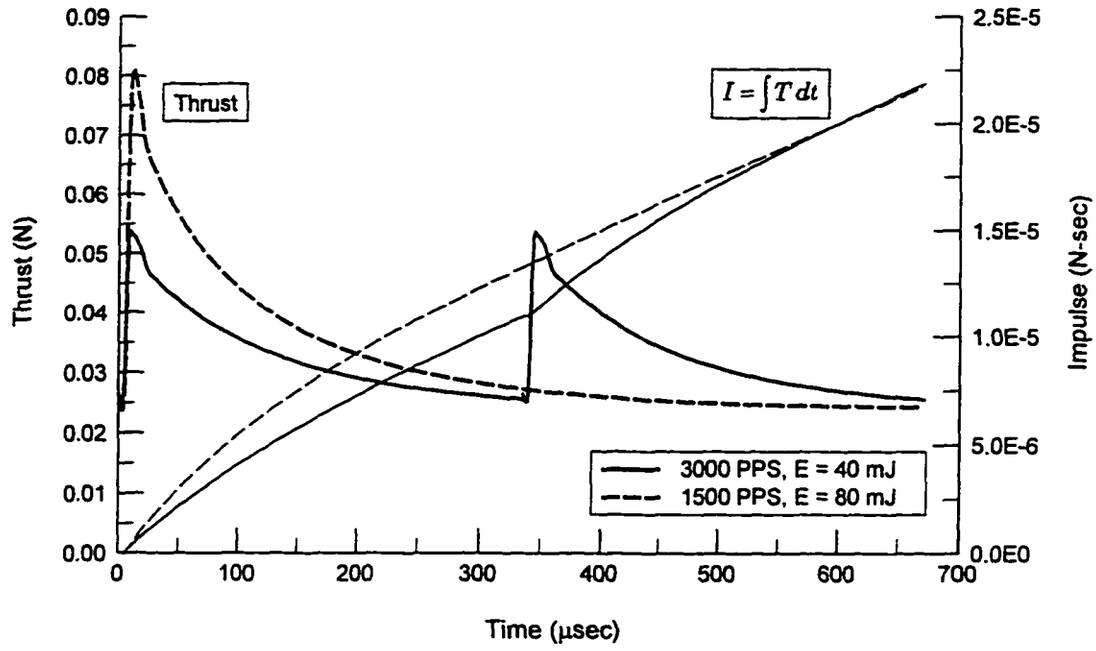

Fig. 4-23. Thrust and total impulse at 1500 pps compared to 3000 pps at the same input power (120 W). The difference in total impulse is within 1 percent over the 666 μs interval.

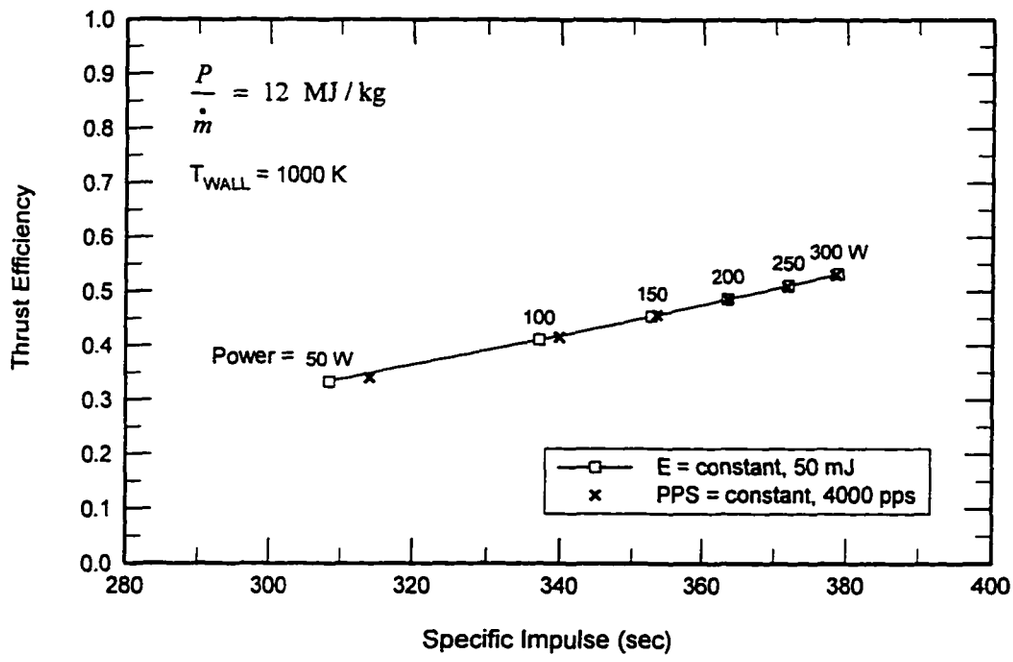

Fig. 4-24. The pulsed arcjet performance scales nearly linearly with input power from 50 to 300 watts. The overall performance is insensitive to the pulse rate and pulse energy.

4.8.4 Wall Temperature and Inlet Gas Temperature

The experimental results indicate that pulsed arcjet performance depends strongly on the wall temperature. The numerical model indicates that an increase of more than 100 seconds I_{SP} can be achieved by improving the arcjet thermal design. The capillary and nozzle wall temperatures are varied from 400 K to 1400 K for a fixed input power of 120 watts and fixed mass flow rate of 10 mg/sec. Two types of boundary condition are used for the temperature of the inlet gas. In the first analysis, the propellant gas is assumed to enter the capillary at 300 K with no regenerative heating from heated surfaces such as the cathode. The second analysis assumes ideal regenerative heating where the propellant gas entered the capillary at the same temperature as the nozzle and capillary walls.

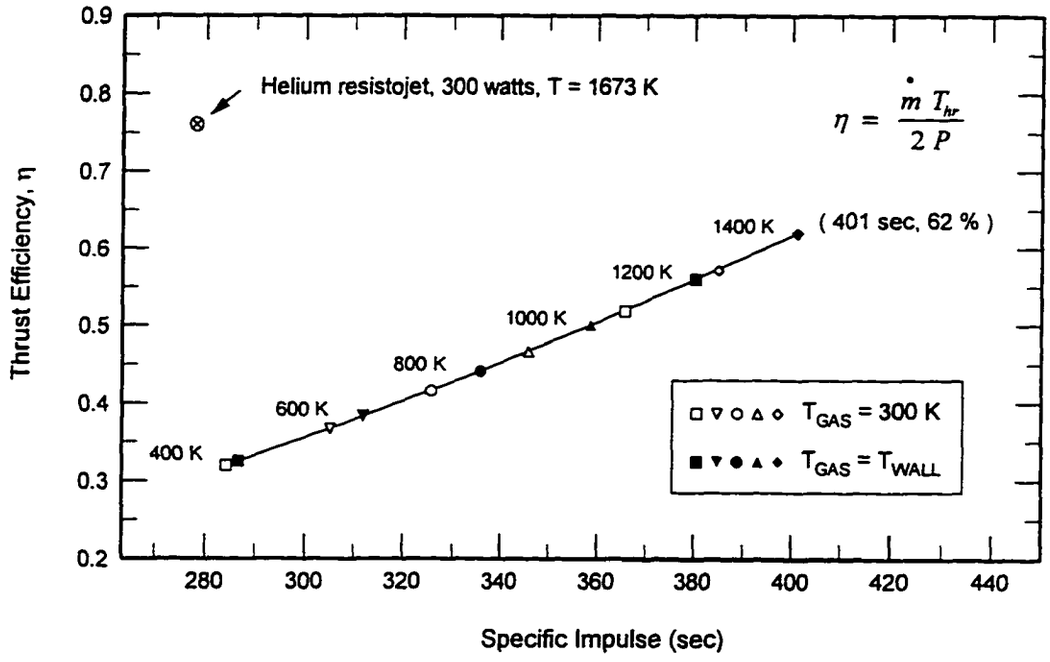

Fig. 4-25. The thermal design of the pulsed arcjet is important because the performance is sensitive to wall temperature. Regenerative heating of the inlet propellant gas can increase the I_{SP} up to 15 seconds.

The specific impulse is found to increase nearly linearly from 285 seconds at a 400 K wall temperature up to 401 seconds with a wall temperature of 1400 K. For comparison, a laboratory model resistojet operating at 300 watts with a 1673 K heater temperature operates at 278 seconds.[4] With an optimized thermal design,

the pulsed arcjet has the potential to achieve higher Isp's than the resistojet, though at a slightly lower efficiency. Both the Isp and efficiency can be improved somewhat by using regenerative heating in the propellant flow path inside the arcjet. At 1400 K wall temperature, the maximum gain from regenerative heating is 15 seconds and 5 percent for the Isp and efficiency, respectively.

4.9 Relative importance of the design parameters on arcjet performance

The sensitivities of the arcjet performance to individual input parameters are evaluated using the numerical model. Each design variable is changed by ± 20% from its baseline value, and the changes in Isp and efficiency are calculated with the numerical model. The normalized results are shown in Fig. 4-26. For example, a 1% change in the input power produces a 0.11% in Isp and a 0.25% change in efficiency. The geometric variables (L, D, A/A*, d*, α) and the wall temperature (T_{WALL}) are evaluated at 120 watts and 10 mg/sec. At fixed power, the pulse rate and the pulse energy vary inversely with each other, so the sensitivity of the two parameters is identical. The power is varied at a fixed specific energy, $P/\dot{m}$=12 mJ/kg.

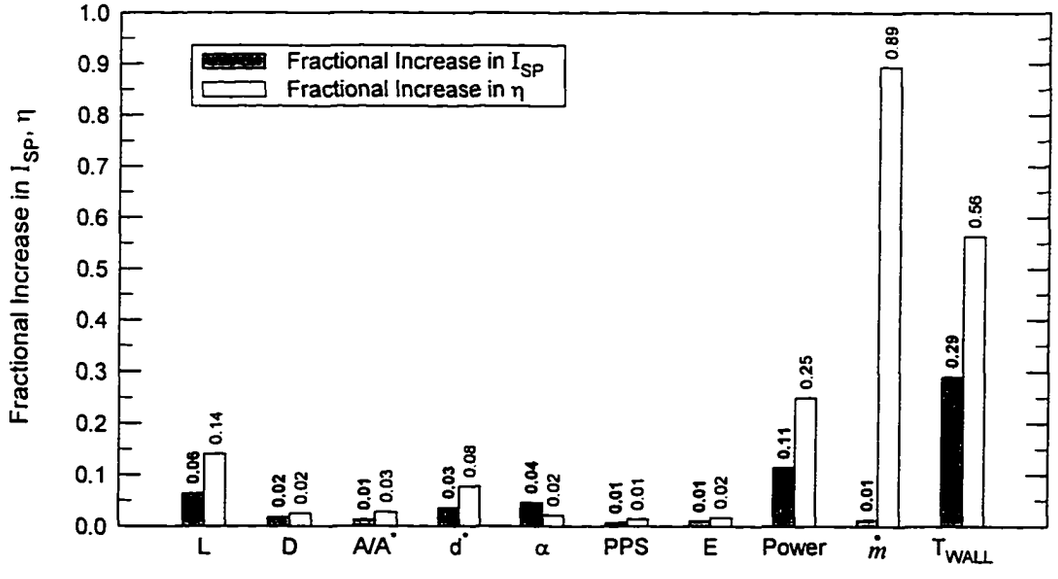

Fig. 4-26. Relative effect of the input parameters on arcjet performance. Wall temperature, input power, and mass flow rate are the dominant variables.

The mass flow rate is the most sensitive parameter affecting the thrust efficiency, and both input power and wall temperature greatly influence both I_{SP} and efficiency. The geometric variables have a relatively minor impact on the performance. The combination of pulse rate and pulse energy has the least effect, which is a non-intuitive result because of the wide range of peak temperatures.

4.10 Transient Behavior During the Arc Discharge.

The output from the numerical model includes the transient behavior of the flowfield variables. For example, the thrust, capillary pressure and exit Mach number during the first 10 μsec for a 5 μsec arc discharge are shown in Fig. 4-27. The pressure increases smoothly to its peak value, which occurs at the end of the arc energy addition. The thrust is calculated from the exit velocity rather than by integrating the pressure over the nozzle interior surface, and so is not truly a transient thrust calculation. These transient results from the numerical model could potentially be used to compare experimental data from single probes in the arcjet plume discussed in the Section 4.7.

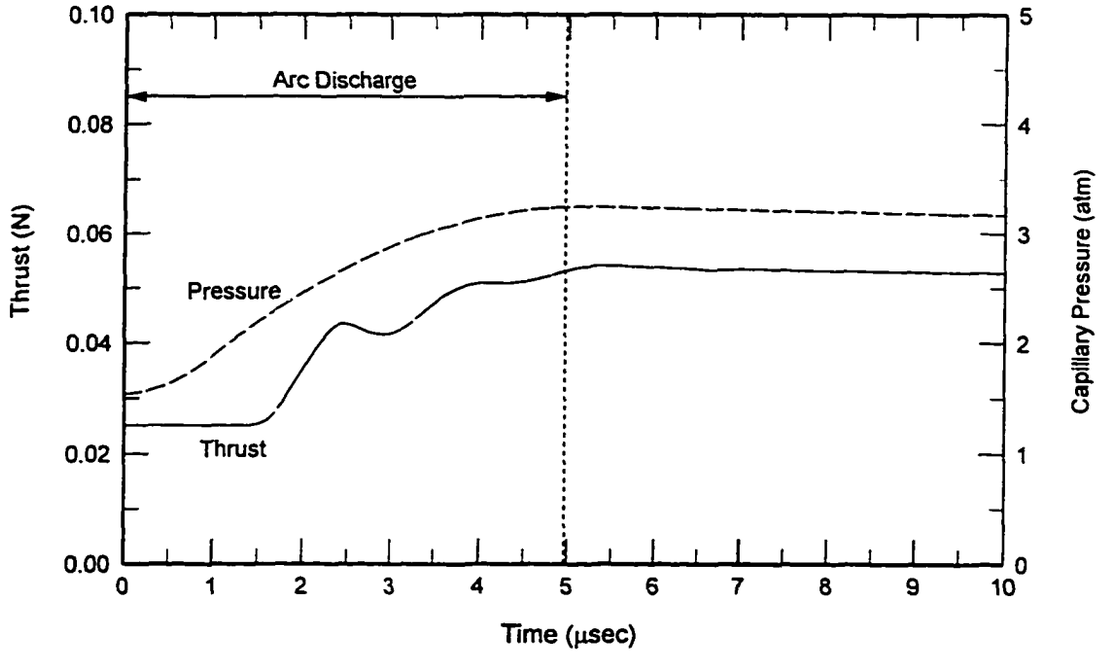

Fig. 4-27. Thrust, and capillary pressure during the first 10 μsec for a 5 μsec arc discharge.

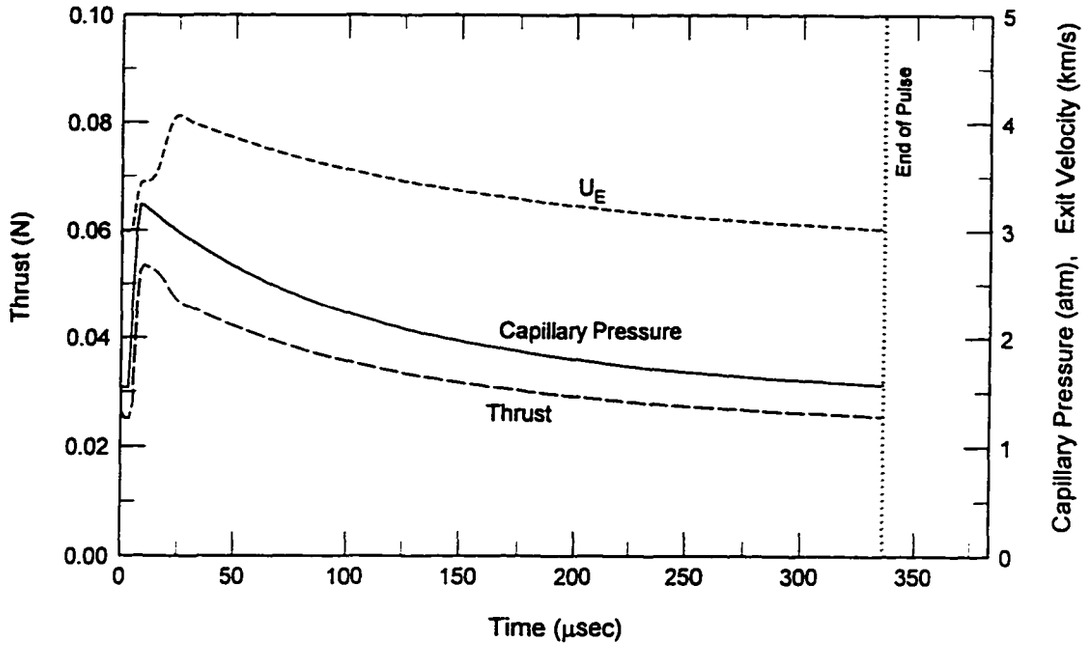

Fig. 4-28. Thrust, capillary pressure, and exhaust velocity during the entire pulse.

References

[1] Grisnik, S. P., Smith, T. A., and Saltz, L. E., "Experimental Study of Low Reynolds Number Nozzles," AIAA Paper 87-0992, 1987.

[2] Murch, C. K., Broadwell, J. E., Silver, A. H., and Marcisz, T. J., "Performance Losses in Low-Reynolds-Number Nozzles," *Journal of Spacecraft and Rockets*, Vol. 5, No. 9, pp. 1090-1094, 1968.

[3] Rothe, D. E., "Electron-Beam Studies of Viscous Flow in Supersonic Nozzles," *AIAA Journal*, Vol. 9, No. 5, pp. 804-811, 1971.

[4] Morren, W. E., Whalen, M. V., and Sovey, J. S., "Performance and Endurance Tests of a Laboratory Model Multipropellant Resistojet," *Journal of Propulsion and Power*, Vol. 6, No. 1, pp. 18-27, 1990.

5. *The Breakdown Voltage and the Arc Current*

A detailed study of the pulsed arcjet would be incomplete without a discussion of two critical parameters: the breakdown voltage and the arc current. The breakdown voltage characteristics of the particular propellant determine the pulse energy and together with the pulse rate establishes the input power. The thruster operating voltage can be reasonably predicted from the Paschen curve for helium, as described in the first part of this chapter. The shape of the arc current pulse determines the efficiency of the energy transfer from the storage capacitor to the propellant. The circuit transfer efficiency directly affects the overall arcjet performance. The arc current is also likely to be an important parameter for the long term erosion characteristics of the electrodes and for capacitor life. The arc current is discussed in the second part of this chapter.

5.1 The Townsend Breakdown Criteria and Paschen's Law

During thruster operation, the external power supply ramps up the voltage on the storage capacitor until electrical breakdown of the gas occurs at a critical value of the electric field, initiating the arc discharge. Breakdown is characterized by a transition from the gas being a poor conductor, with $R_{ARC} > 1\ M\Omega$, to a good conductor with $R_{ARC} \sim 1\ \Omega$. The electrical breakdown of gases is a fairly extensive subject, and only a basic discussion is included here.

On a macroscopic level, the breakdown voltage depends on the nature of the gas (pressure, molecular weight) as well as the material and surface conditions of the electrodes. From a microscopic perspective, the breakdown mechanism is controlled by particle collisions in the gas. A free electron in the gas will be accelerated by an applied electric field until it collides with another particle. If the electric field is strong enough, free electrons will have enough energy to undergo ionizing collisions, creating additional free electrons in what is called an electron avalanche. The onset of breakdown is extremely rapid because the production of electrons is exponential. In most gases at moderates pressures, up to a few atmospheres at ambient temperatures, the breakdown voltage for plane parallel

electrodes and no insulator breakdown effects can be predicted from the Townsend breakdown criteria,[1]

$$\left(\frac{\omega}{\alpha}\right)\left[\ \exp\ (\alpha d)-1\ \right]=1 \tag{5.1}$$

The variable α is the Townsend primary ionization coefficient, which represents the average number of ionizing collisions made by an electron as it travels one unit length along the electric field. The parameter ω / α is known as the generalized secondary ionization coefficient, which represents the number of secondary electrons produced per primary ionization. It is the sum of a number of individual secondary processes, such as electron-ion emission and photoemission, though these individual processes are generally combined into an effective coefficient, γ. The coefficient γ depends on the emission properties, surface conditions and material of the cathode. In general, γ is on the order of 0.1 to 0.01.[1,2]

Experimentally, the breakdown voltages for many gases are found to obey a similarity condition in which the primary and secondary ionization coefficients are functions of the ratio E/n, or equivalently V_B/nd, where n is the gas number density, and d is the separation distance between the electrodes.

$$\frac{\alpha}{n} = \Phi\left(\frac{V_B}{nd}\right) \quad \text{and} \quad \frac{\omega}{\alpha} = \Psi\left(\frac{V_B}{nd}\right) \tag{5.2}$$

Substituting these relationships into the Townsend breakdown criteria gives,

$$\Psi\left(\frac{V_B}{nd}\right)\left\{\ \exp\left[\ \Phi\left(\frac{V_B}{nd}\right)nd\ \right]-1\ \right\} = 1 \tag{5.3}$$

The similarity rule, $V_B = f(nd)$, is commonly known as Paschen's law, which states that the breakdown voltage is function of the single combined parameter, nd.

A simple expression for the breakdown voltage can be obtained using experimental values of α/n for helium from a compilation of electron swarm data from Dutton,[3] as shown in Fig. 5-1. Substituting a curve fit for α/n into the breakdown criteria (Eq. 5.1) gives an expression for the breakdown voltage in helium,

$$V_B = \frac{68.9 \times 10^{-17}\, nd}{\ln\left(\dfrac{15.2 \times 10^{-18}\, nd}{\ln\,(1/\gamma)}\right)} \tag{5.4}$$

where nd is expressed in cm^{-2}. The variable, γ, in the above equation is an alternative form of the second ionization coefficient,

$$\frac{1}{\gamma} = 1 + \frac{1}{\omega/\alpha} \tag{5.5}$$

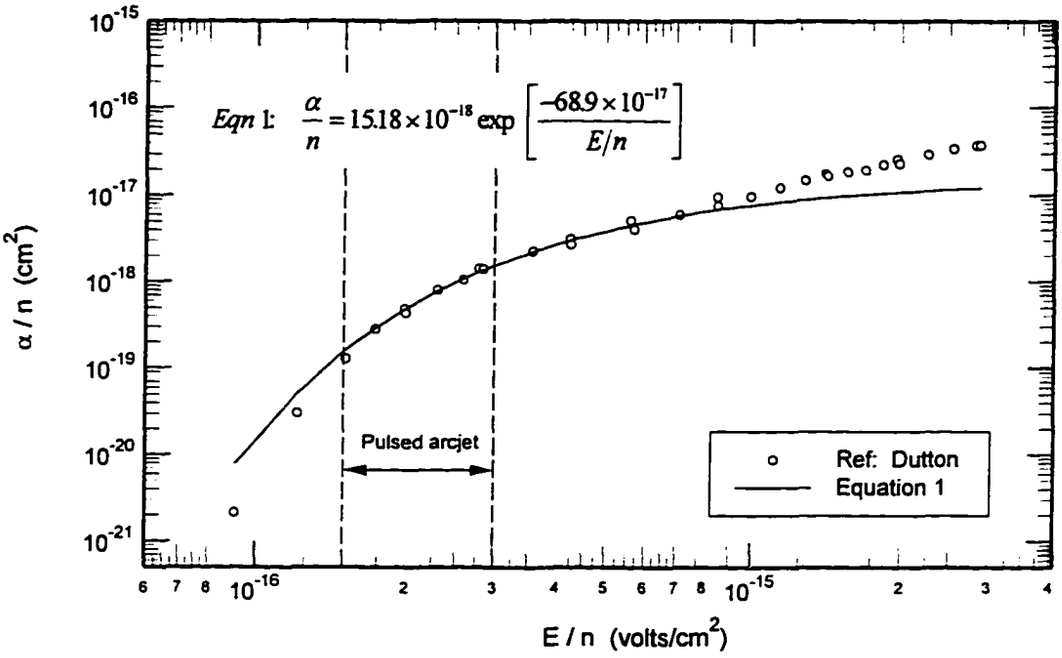

Fig. 5-1. The Townsend first ionization coefficient, α/n, for helium from the electron swarm data of Dutton.[3]

5.1.1 Experimental Results for Breakdown Voltage

Breakdown voltages for helium were measured for several pulsed arcjet geometry's and compared to Eq. 5.4. The breakdown measurements were made prior to the steady state performance tests with the arcjet in its operating configuration. The only difference was that the breakdown voltage tests were run at very low pulse rates (< 5 pps) so that the pressure in the capillary would return to its initial cold flow value, and the gas could be assumed to be at room

temperature. The breakdown voltage was measured by integrating the capacitor charging current (see Appendix B-3). The number density is calculated from the ideal gas law, $P = nkT$, in which the pressure is determined from the mass flow rate. At each value of *nd*, 3 to 5 breakdown voltage measurements are recorded, and the error bars in Fig. 5-2 represent the lowest and highest data points.

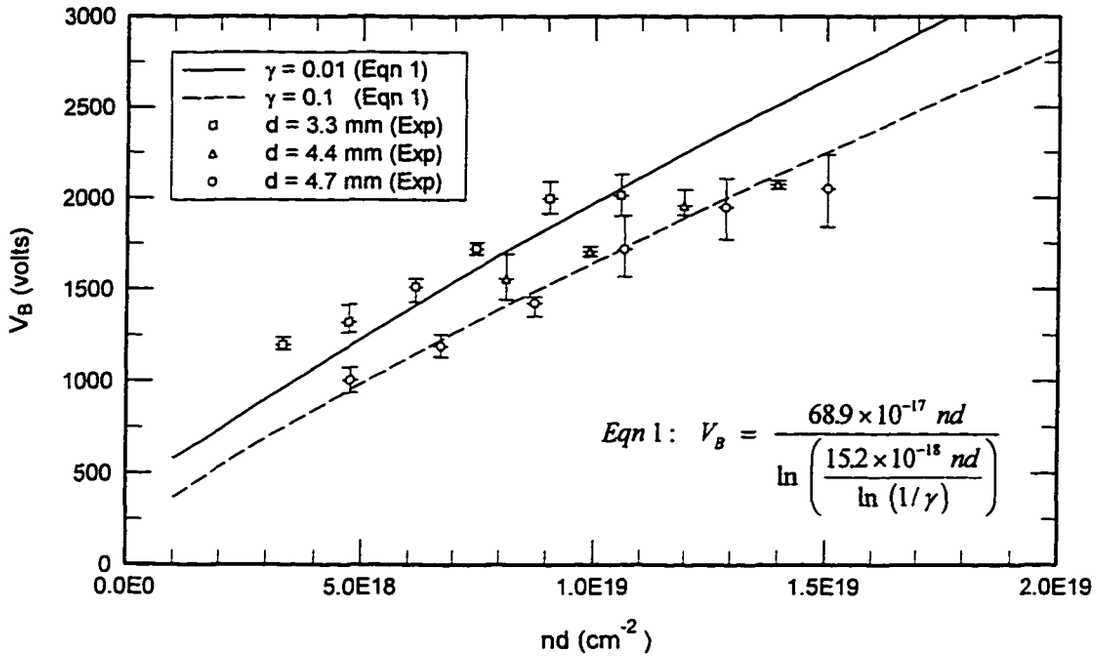

Fig. 5-2. Experimental breakdown voltage in helium for 3 values of the electrode separation distance, compared to Paschen's law.

5.1.2 Breakdown Distance, d

The prediction of electrical breakdown is assumed to follow Paschen's law, even though a number of complicating factors exist in the pulsed arcjet. These factors include the non-uniform electric field between the electrodes and the presence of the boron nitride insulator, which has a dielectric constant of approximately 4. The sharp corners on the electrodes and surface charges on the insulator could potentially affect breakdown as well. A detailed electrostatic analysis is beyond the scope of this research, and electrical breakdown is simply correlated using the breakdown distance, *d* as shown in Fig. 5-3, for evaluating the parameter *nd*.

In general, breakdown processes are studied in a uniform field between parallel electrodes, and the electrode separation distance is the same as the arc length, $d = L$. The electric field and the voltage are simply related, $V = Ed$. For the particular geometry used in the pulsed arcjet described here, the electric field between the electrodes is not uniform due to the electrode geometry and the boron nitride dielectric, and $d \neq L$. Since the important quantity in predicting electrical breakdown is the field strength rather than the voltage, the electric field at the cathode is estimated using the minimum distance, d, between the electrodes, even though this distance is through the capillary wall. When plotted using d, the breakdown voltage follows Paschen's law with much better agreement than using the arc length, L.

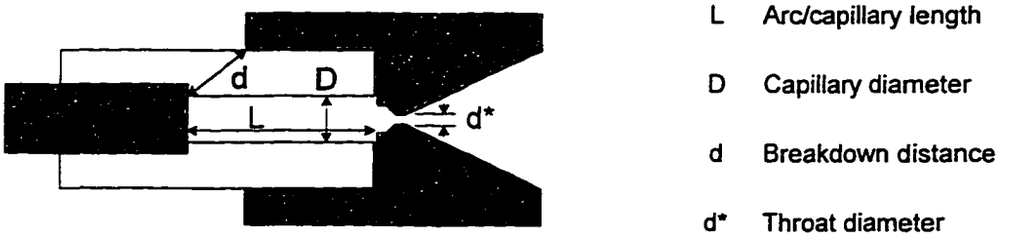

Fig. 5-3. Definition of length variables for the electrode and capillary geometry. The experimental data for breakdown voltage are correlated using the length *d*.

Utilizing the self-breakdown voltage to initiate the arc discharge eliminates the need for a separate sparking circuit. However, this technique couples the breakdown voltage to the mass flow rate through the gas number density. This coupling places additional restrictions on the thruster operation because the input power and the mass flow rate cannot be specified independently. In addition, for electrode configurations in which d is identical to the arc length, $d = L$, the gas peak temperatures tend to be relatively high, even for helium, which breaks down at relatively low voltages.

A potential solution to the problem of excessive peak temperature is to decouple the breakdown distance from the arc length by intensifying the field strength at the cathode. The results of a calculation shown in Fig. 5-4 illustrate the effect of decreasing the breakdown distance on the voltage and peak temperature

for a fixed capillary length and volume. By decreasing the breakdown distance from 7.5 mm to 3.3 mm, the breakdown voltage in helium decreases from 2530 volts to 1350 volts with an accompanying decrease in peak gas temperature from 9330 K to 2880 K. For this plot, values for number density, capacitance, and capillary diameter are 2.32 x 10^{19} cm^{-3}, 0.05 μF, and 2.5 mm, respectively. The experimental data from the breakdown tests appear to demonstrate this approach.

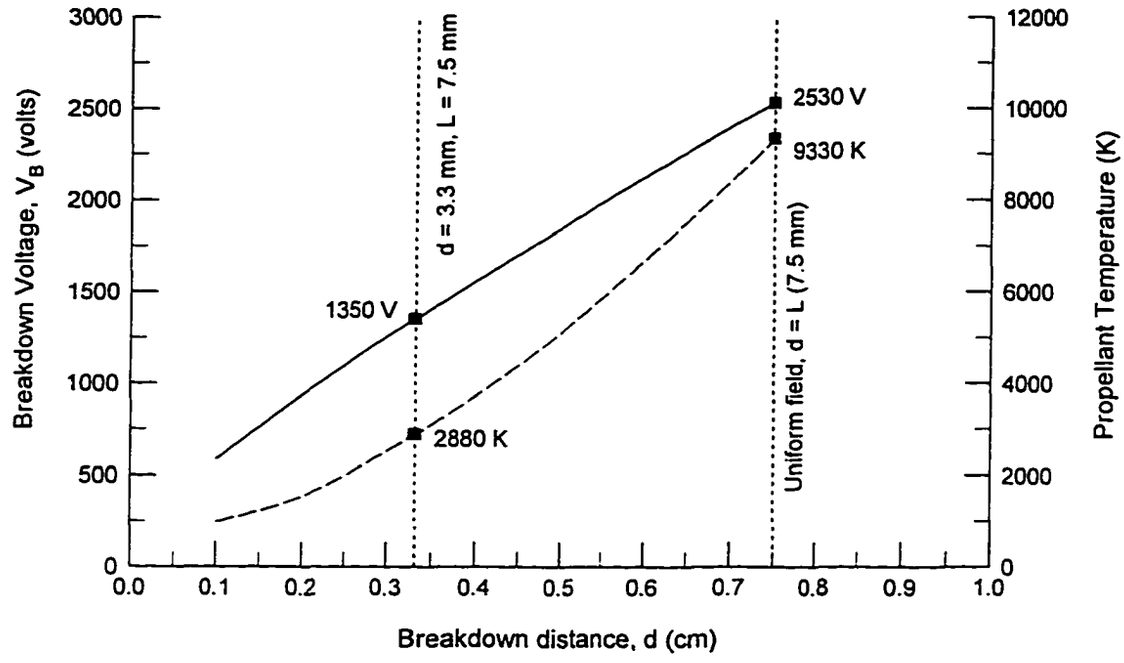

Fig. 5-4. The electrode separation distance, *d*, can be decoupled from the arc length, *L*, producing a large change in the breakdown voltage and gas peak temperature.

The Paschen curves for diatomic gases, such as simulated-hydrazine, are higher and steeper than for helium, resulting in high peak temperatures and large dissociation frozen flow losses when the breakdown distance is the same as the arc length. It is somewhat counter-intuitive that the breakdown of helium occurs at much lower electric fields than for molecular gases such as hydrogen and nitrogen, even though the ionization energy in helium (24.58 eV) is much higher than for molecular hydrogen (13.6 eV) or nitrogen (14.5 eV). The explanation is given concisely by Meek and Craggs:[1] "In molecular gases, electrons lose energy in exciting the molecules to low-energy states, and consequently have a high

probability of ionizing only when the electric field strength is high enough to give an electron the full ionization energy within a single free path. In the inert gases, such energy losses do not occur, and the ionization energy may be built up in the course of several elastic collisions. Thus ionization, and consequently breakdown, is achieved relatively easily in the inert gases in spite of their high ionization energies."

5.1.3 Experimental Measurement of Number Density, n

The number densities used in Fig. 5-2 were obtained from the ideal gas law, where the pressure is calculated from the mass flow rate set by the flow controllers rather than from direct measurement. For isentropic flow of a calorically perfect gas in a nozzle, the mass flow rate for choked flow can be calculated from the inlet total conditions and the nozzle throat area,

$$\dot{m}_{IDEAL} = \frac{P_0 A^*}{\sqrt{R T_0}} \sqrt{\gamma \left(\frac{2}{\gamma+1}\right)^{\frac{\gamma+1}{\gamma-1}}} \quad [kg/s] \tag{5.6}$$

For typical flow conditions in the pulsed arcjet, viscous boundary layer effects are not negligible, so that the actual mass flow rate is less than the ideal mass flow for a given inlet pressure. Equivalently, the experimental inlet total pressure is higher than the ideal total pressure at a given mass flow rate. Therefore, to determine the capillary pressure from a given mass flow rate requires a correction factor in terms of a discharge coefficient, defined as the ratio of the actual mass flow rate to the ideal flow rate,

$$C_D = \frac{\dot{m}_{ACTUAL}}{\dot{m}_{IDEAL}} \tag{5.7}$$

The propellant inlet pressure is measured with a Wallace & Tiernan vacuum gauge for steady state flow with room temperature helium (298 K). The discharge coefficient, C_D, is plotted versus Reynolds number in Fig. 5-5 where the solid line in the graph is a polynomial curve fit to the experimental data.

$$C_D = 0.304 + 1.53\times10^{-3} Re - 1.75\times10^{-6} Re^2 + 9.30\times10^{-10} Re^3 - 1.82\times10^{-13} Re^4 \tag{5.8}$$

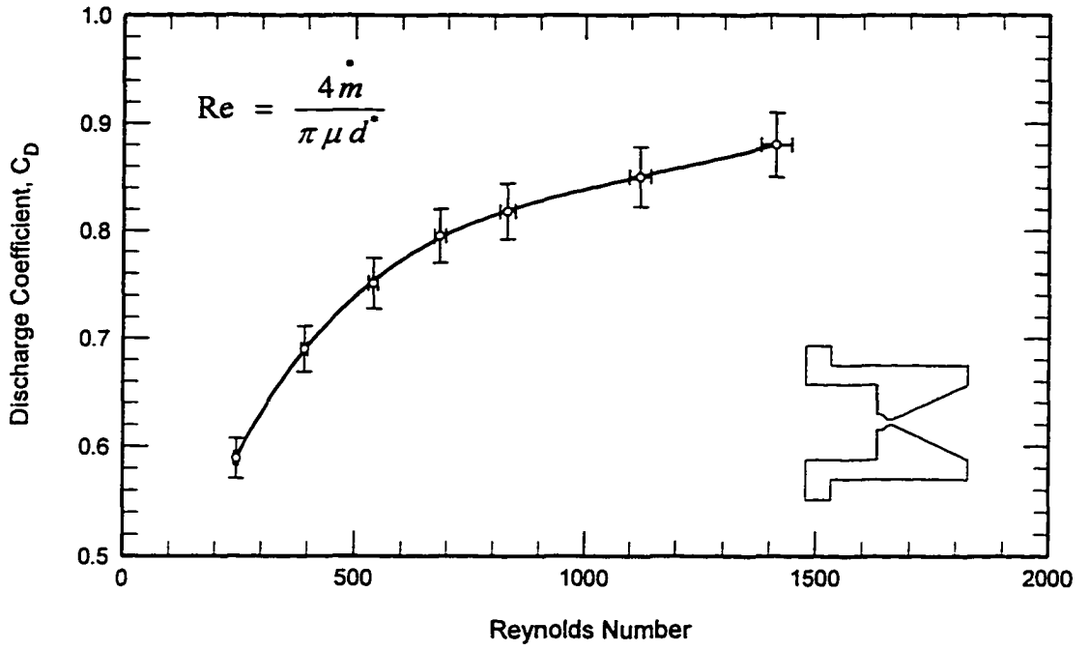

Fig. 5-5. Nozzle discharge coefficient versus Reynolds number measured in a steady flow experiment with room temperature helium.

The objective of the breakdown tests was to examine V_B as close as possible to operating conditions and cannot be considered precise breakdown measurements for a number of reasons. First, the electrodes were not cleaned or conditioned, but were simply used 'as is' from previous tests. Second, the pressure and number density have relatively large experimental uncertainty, since they were obtained indirectly through the mass flow rate rather than direct measurement. Third, the breakdown voltage could have been influenced by additional factors such as the presence of the capillary wall, impurities in the gas, the non-uniform electric field between the electrodes, and the non-zero propellant flow velocity. These variables would need to be eliminated in a precision breakdown voltage experiment.

5.2 Arc Current and Arc Column Model

The magnitude and shape of the current pulse are important for several reasons. The current pulse shape affects the amount of energy transferred to the propellant gas compared to the energy lost in the external circuit, and these losses

directly affect the total arcjet efficiency. In addition, the shape of the current pulse is likely to be an important parameter for the long term erosion characteristics of the electrodes and capacitor life. On the other hand, the shape of the current pulse has only a minor effect on the gas dynamics of the flow because the arc discharge occurs on a time scale much shorter than the time between pulses. As described in Chapter 4, the thrust performance is essentially independent of the rate of energy input to the gas, i.e. the *peak* power, which is on the order of 10-40 kW during the arc discharge, and depends to a much greater extent on the *average* input power.

The arc current is measured experimentally, and the data are compared with the arc currents predicted from a simple analytical model and a commercial software code called PSPICE.[4] The arc column characteristics, including arc temperature and arc radius, are approximated using a channel model. These results are discussed in the following sections.

5.2.1 Analytical Model

The time-development of the arc current is established by the design of the pulse forming electrical circuit and the characteristics of the arc resistance. The arcjet electrical circuit in Figure 2-5 is discussed here for two cases, with and without the diode. The arcjet circuit was modified to include the diode and the Brooks coil when preliminary tests indicated high parasitic losses in the capacitor.[5] The equations and sample calculations are included for both cases.

Without the diode, the circuit behaves similar to (but not exactly as) a simple LCR circuit, and the circuit equation can be written,

$$V_B - \frac{1}{C}\int_0^t I\,dt - (L_{EXT} + L_{ARC})\frac{dI}{dt} - \left(R_{EXT} + \frac{dL_{ARC}}{dt}\right)I - R_{ARC}I = 0 \qquad (5.9)$$

Equation 5-8 can be solved analytically provided that a relationship for the arc resistance, R_{ARC}, is known. However, the difficulty in solving the circuit equation arises from the fact that the arc resistance is not known *a priori* but depends on the rate of energy input to the gas, i.e. the current, $R_{ARC}(t) = f(I(t))$. The key to accurately modeling the arc current is in determining the form of the arc resistance. A number of models for predicting the resistance in a transient arc

discharge can be found in the literature.[6, 7, 8, 9, 10] A review of the more well-known formulations is given by Engel.[11] The model that appears to work well for the pulsed arcjet is to assume that the arc resistance varies inversely with the arc current, or that the voltage drop across the arc is constant during the pulse.

$$R_{ARC}(t) = \frac{V_{ARC}}{I(t)} \quad \text{with} \quad V_{ARC} = \text{constant} \tag{5.10}$$

The arc inductance, L_{ARC}, is ~ 10 nH and can be neglected compared to the 2.9 μH external circuit inductance. Replacing the arc resistance, R_{ARC} with V_{ARC} / I, the circuit equation can be solved analytically for the current. The equations for calculating the current have been developed by Robiscoe,[12, 13, 14] and are included in Appendix D.

In the circuit with the diode, the arc current is evaluated by examining the circuit equation in two parts. During the first part, the arc current increases from zero to the peak current in approximately 1 μsec. Current does not flow through the diode, and the equations for both circuits are identical,.

$$I(t) = V_0 \sqrt{\frac{C}{L_{EXT}}} \exp\left(\frac{-R_{EXT}\, t}{2\, L_{EXT}}\right) \sin\left(t\sqrt{\frac{1}{L_{EXT} C}}\right) \tag{5.11}$$

where V_0 is equal to the breakdown voltage minus the arc voltage, V_B - V_{ARC}.

During the initial current rise, the arc current increases from zero to a maximum, and the voltage on the capacitor decreases from V_B to zero. Only 10-20 percent of the initial stored energy is transferred to the propellant in the first half cycle, and the remaining energy is temporarily stored in the magnetic field of the circuit inductance, $E = ½\, L_{EXT}\, I^2$. After the time of peak current, the capacitor is essentially removed from the circuit, and current flows through the diode return loop. The circuit equation is,

$$L_{EXT}\frac{dI}{dt} - V_{ARC} - V_{DIODE} - V_{EXT} = 0 \tag{5.12}$$

where V_{ARC} is the voltage drop across the arc, V_{DIODE} is the voltage drop in the diode (~2-3 volts), and V_{EXT} is the voltage drop associated with the external circuit resistance at high frequency.

A comparison of the calculated currents for the circuit with and without the diode is shown in Fig. 5-6. Without the diode, the circuit is underdamped, resulting in large current reversals in the capacitor. The calculations correctly reproduce the finite number of oscillations that have been observed in experimental data.[5] With the diode, the current decreases linearly from its maximum to zero without current reversals in the arc.

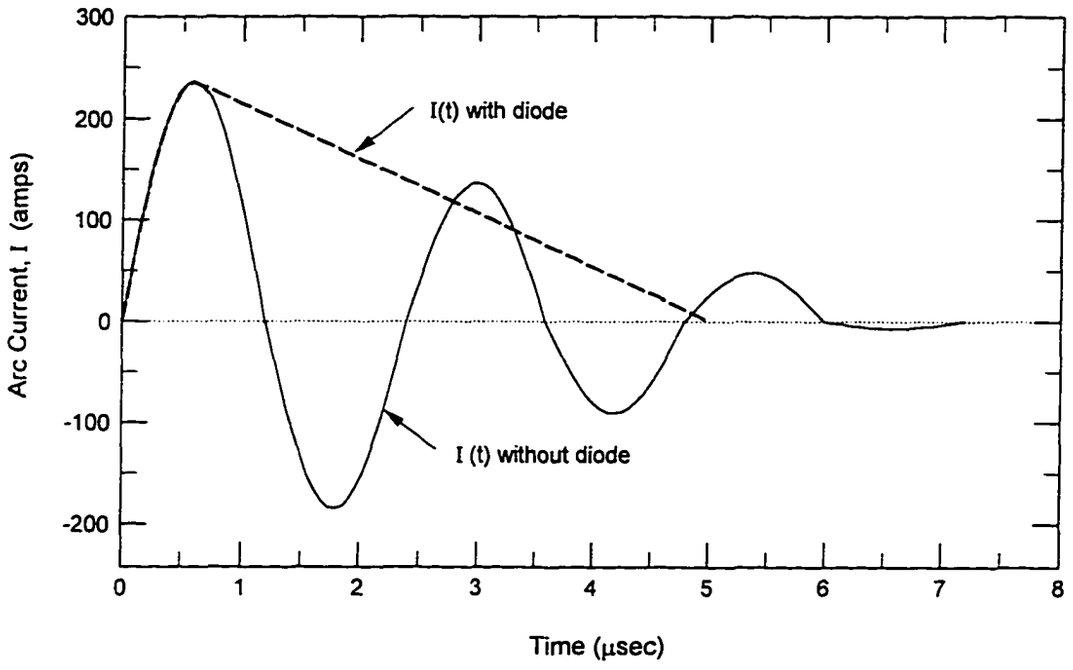

Fig. 5-6. Comparison of the calculated arc current for the circuit with and without the diode. Without the diode, the circuit is underdamped with large current reversals.

5.2.2 PSPICE Numerical Model

The simple analytical model represented by Eqs. 5.11 and 5.12 assumes an ideal capacitor and neglects the effects of finite inductance present in a real capacitor. The capacitor inductance can affect the shape of the discharge pulse and the overall circuit efficiency, and an appropriate value is used in a more detailed numerical analysis of the complete circuit with the PSPICE computer code. The

internal inductances of the capacitors are measured experimentally (see Appendix B-4) and are 45 nH and 110 nH for the 0.05 μF and 0.10 μF units, respectively. In addition to the arc current, the PSPICE code gives results for the current in the capacitor and the diode, as shown in Fig. 5-7. The finite inductance associated with the capacitor side of the diode loop causes the minor current oscillations, or ringing, in the capacitor current as well as the inductive 'kick' in the diode current. The magnitude of these secondary oscillations increase with the inductance on the capacitor side of the circuit, so it is desirable to closely couple the diode and the capacitor to minimize the inductance in that part of the circuit.

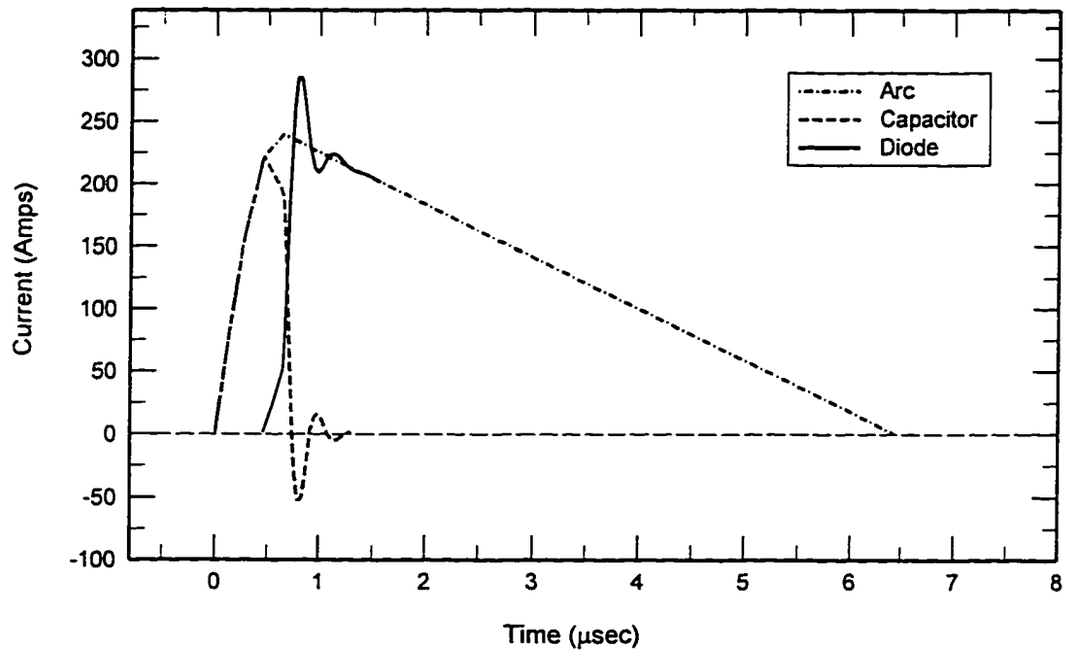

Fig. 5-7. Currents in the circuit calculated with the PSPICE code. The oscillations in the capacitor and diode currents are due to non-zero inductance in the capacitor.

5.2.3 Experimental Results for Arc Current

In the analytical models, the breakdown voltage, arc voltage, and external resistance during the first half cycle are obtained from experimental data. The breakdown voltage is measured directly, and the other two variables are obtained from curve fits to the arc current data. The calculated results are compared to data for a typical pulse in Fig. 5-8. The analytical model and the PSPICE calculation

closely match the experimental data with some deviations near the current peak and at the end of the pulse. The middle section of the current trace is linear, partially justifying the initial assumption of constant arc voltage.

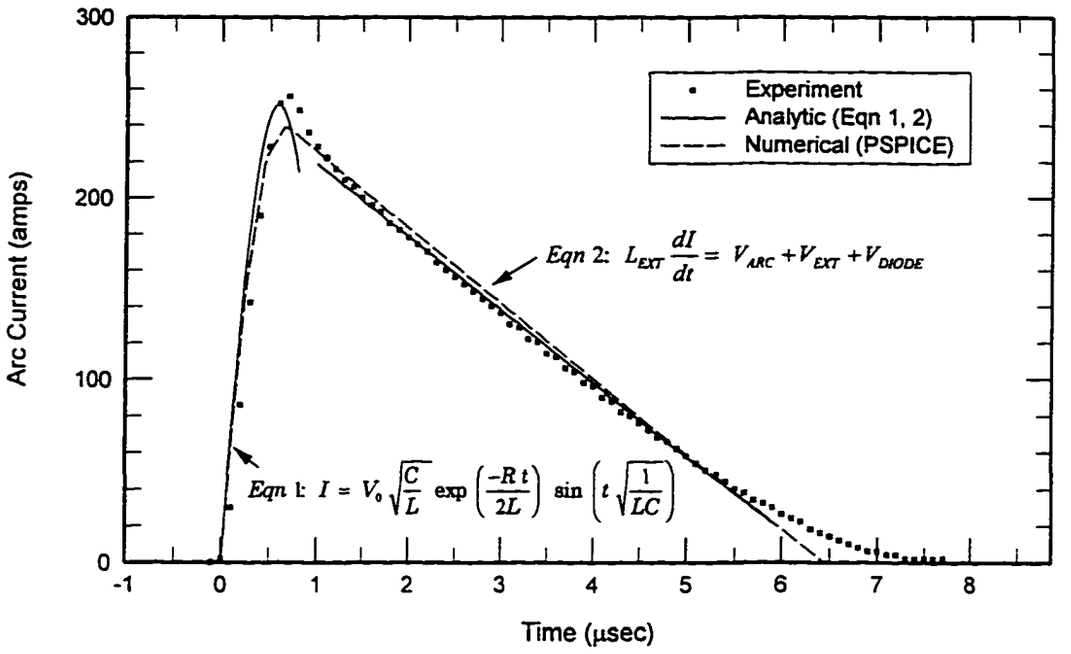

Fig. 5-8. Comparison of experimental arc current with the analytical solution and the PSPICE code.

The repeatability of the discharge current is shown in Fig. 5-9 for 19 measurements. For this test, the current was recorded at approximately 15 second intervals with the thruster running at low pulse rate (<5 pps). The values for the peak current ranged from a low of 274 amps to a high value of 328 amps with a 303 amp average. These variations in the peak current are due to shot-to-shot variations in the breakdown voltage. Since only 10-20 percent of the initial stored energy is dissipated during the first half cycle, the peak current is roughly proportional to the breakdown voltage,

$$\frac{1}{2}L_{EXT}\,I^2 \approx \frac{1}{2}C\,V_B^2 \tag{5.13}$$

and Fig. 5-9 is basically a measure of the breakdown voltage repeatability at low pulse rates.

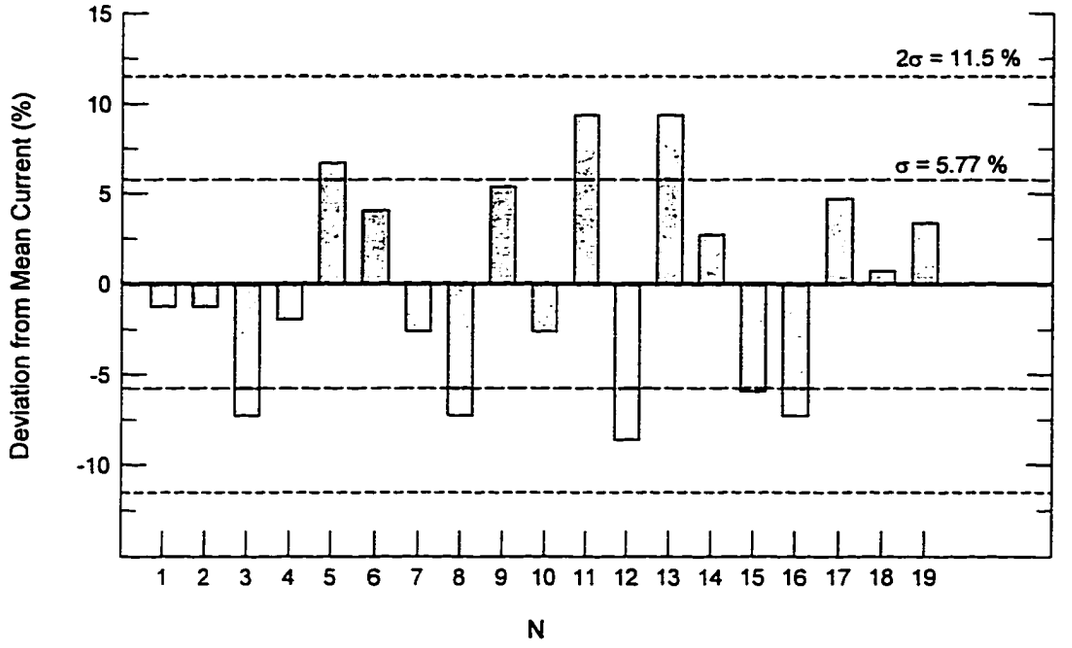

Fig. 5-9. Variation in the arc peak current measured at 15 second intervals. The deviation from the mean current corresponds to deviations in the breakdown voltage.

5.3 Arc Voltage and Resistance

The assumption of constant arc voltage turns out to be quite good, so that the arc voltage can be obtained experimentally from the slope of the current trace in its linear region. A measurement of the arc voltage using a high voltage probe was attempted; however, the transmission line from the arcjet to the probe located outside the vacuum tank introduced high frequency oscillations in the discharge current.

5.3.1 Experimental Results for Arc Voltage

Arc voltages are shown in Fig. 5-10 for four pulsed arcjet configurations. Each data point represents the average of 3-5 measurements, and the error bars represent the highest and lowest values recorded. Several trends are observed in the data. The arc voltage increases with increasing capillary pressure, increasing arc length, and decreasing capillary diameter. These trends are intuitive, since they correspond to the voltage drop in a typical conductor, in which the resistance is

proportional to the conductor length and inversely proportional to cross sectional area.

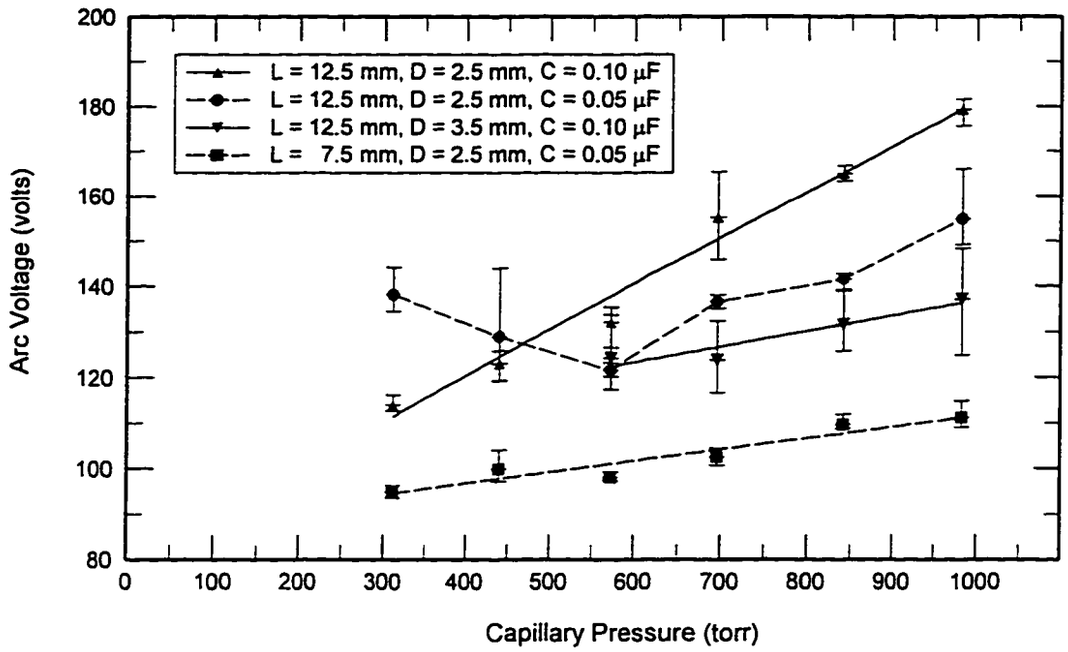

Fig. 5-10. Voltage drop in the arc for four arcjet configurations. The arc voltage increases linearly with the initial gas pressure in the capillary.

5.3.2 The Channel Model for the Arc Column

The transient arc resistance can be estimated from Ohm's law and the experimental values for arc voltage and current. However, this is insufficient information to calculate the arc temperature because the arc radius is not known. Making an assumption that the arc radius is equal to the capillary radius gives results that are not self-consistent. This assumption is not valid for the pulsed arcjet because the pulse energies in these experiments are too low to produce an arc column that fills the capillary entirely. An approach that calculates the arc radius is needed.

It is well known that arcs tend to run at constant voltage, and these experimental results follow that condition closely. The Steenbeck minimum principle,[15] or principle of minimum power, is a method for arc columns that fits most experimental data quite well. However, according to Raizer,[16] this principle is

not implied by the fundamental laws of physics, and further, this assumption is a supplementary principle that is not needed to calculate the behavior of the arc column. The approximation called the channel model, also suggested by Steenbeck, gives self-consistent results for an arc column. A discussion as well as the derivation of the equations is given by Raizer, though a brief summary and the final equations are given below.

In the channel approximation, the arc is assumed to have a constant temperature and electrical conductivity across the arc radius, r_0, which is less than the tube, or capillary, radius, R. Energy is transferred to the arc by ohmic heating and then is transported radially outward by heat conduction. The energy balance in the channel is given by

$$\frac{1}{r}\frac{d}{dr}r\left(\kappa\frac{dT}{dr}\right) + \sigma(T)E^2 = 0 \qquad (5.14)$$

This equation is called the Elenbaas-Heller equation for steady arcs. Strictly speaking, the transient arc discharge requires a time-dependent term in the energy equation. However, if the arc radius is very small, the energy in the discharge is transported radially outward on a time-scale that is rapid compared to the discharge time. Hence, using this equation 'as is' is essentially a quasi-steady approximation. Of course, an improvement to this analysis would include the time-dependent energy terms as well as energy losses due to radiation.

The electrical conductivity is approximated with an exponential curve fit that is valid at arc temperatures,

$$\sigma(T_m) = C\exp\left(\frac{-I_{EFF}}{2\,k_B\,T_m}\right) \quad [ohm-cm]^{-1} \qquad (5.15)$$

For helium, the constants in the electrical conductivity are $C = 620$ (Ohm-cm)$^{-1}$ and $I_{EFF} = 5.63$ eV, which is an effective ionization potential. The constants, C and I_{EFF}, are from a curve fit to the Spitzer conductivity (see Appendix E).

The thermal conductivity, κ [W/m-K], is approximated by an exponential function (see Appendix E),

$$\kappa = 0.41\exp\left(\frac{T_m}{6330}\right) \qquad (5.16)$$

The equations for the arc temperature, radius, and electric field are as follows:

$$T_m = \frac{I_{EFF} / k_B}{\ln\left(8 \pi^2 \kappa C k_B T_m^2 / I_{EFF}\right) - 2 \ln\left(I / R\right)} \tag{5.17}$$

$$\left(\frac{r_0}{R}\right)^2 = \frac{\sigma}{C} \tag{5.18}$$

$$E = \frac{8 \pi \kappa k_B T_m}{I_{EFF}} \frac{1}{I} \tag{5.19}$$

These equations allow the arc column characteristics to be calculated for a specified arc current, *I*. The experimental data for a pulse are used to calculate the arc voltage. The calculated arc voltage (Fig. 5-11) is relatively constant and agrees well with the value obtained from the slope of the current trace. The arc resistance (Fig. 5-12) decreases to a minimum within 1 μsec to ~ 600 mΩ and then increases monotonically. The calculated arc channel radius ranges from 0.3 to 0.6 mm in the 2.5 mm diameter capillary, representing 6 to 23 percent of the total capillary volume. At higher pulse energies where the arc fills the capillary, a wall-confined arc model may need to be applied rather than the channel model equations.

These results appear reasonable, though confirming the calculated results for the arc temperature and radius by independent measurement would be a difficult experiment and was not performed. The quasi-steady channel model seems to describe the transient discharge approximately and gives self-consistent results, though certainly more accurate calculations and experiments are possible than those described here.

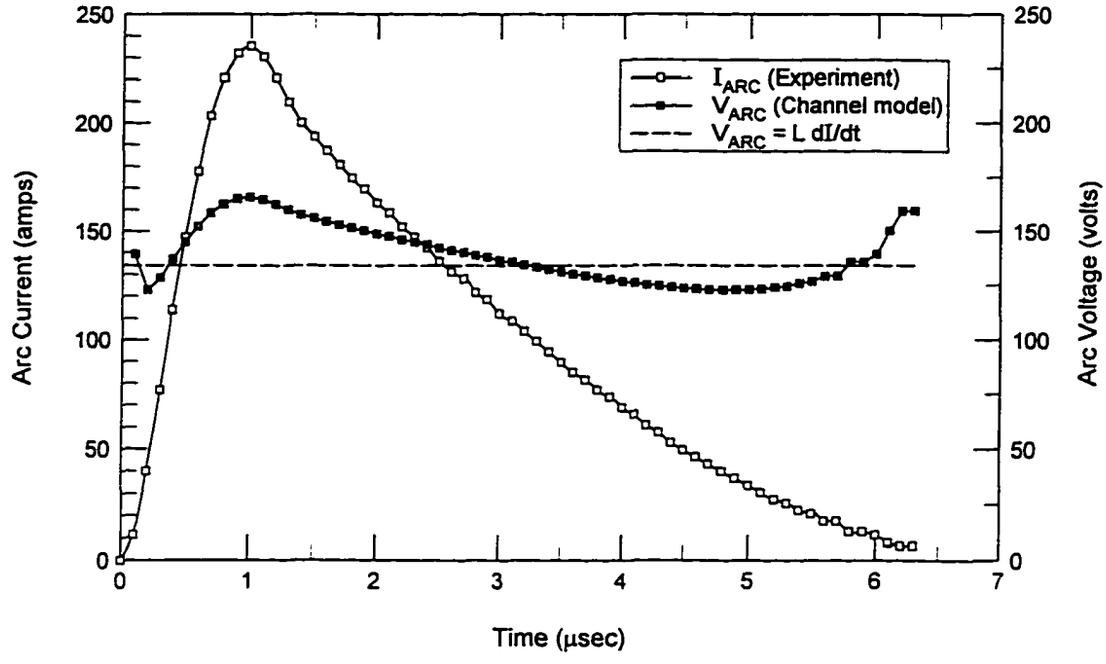

Fig. 5-11. Arc voltage calculated using the channel model and experimental data for arc current. The channel model agrees closely with the constant arc voltage approximation.

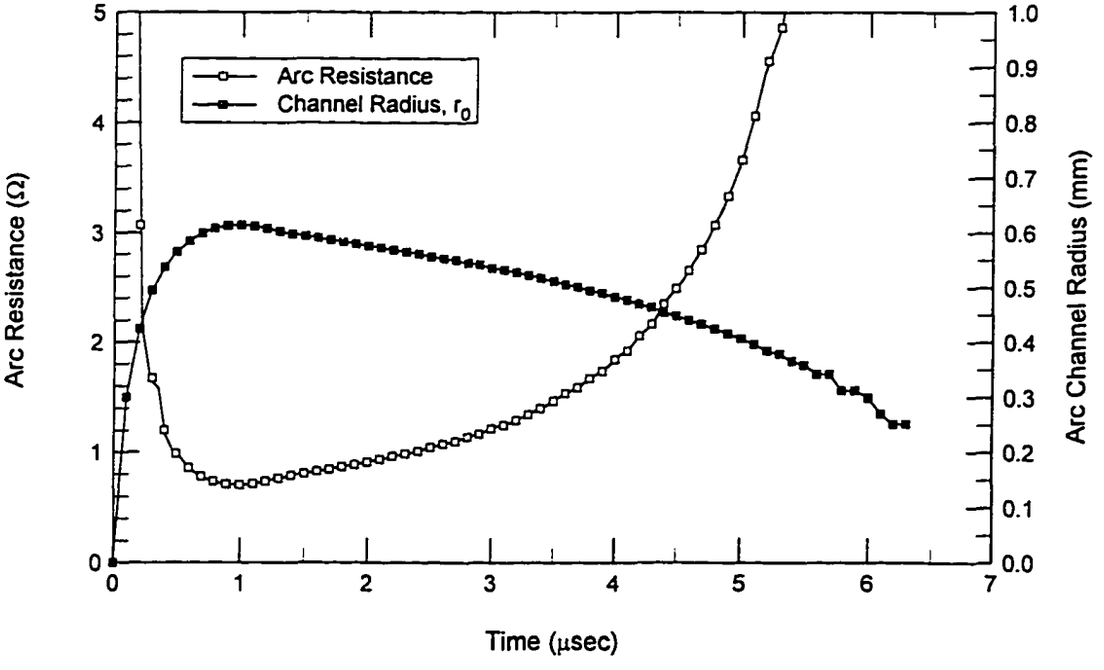

Fig. 5-12. Arc resistance and channel radius from the channel model. The arc occupies 6 to 23 percent of the total capillary volume in the 2.5 mm diameter capillary.

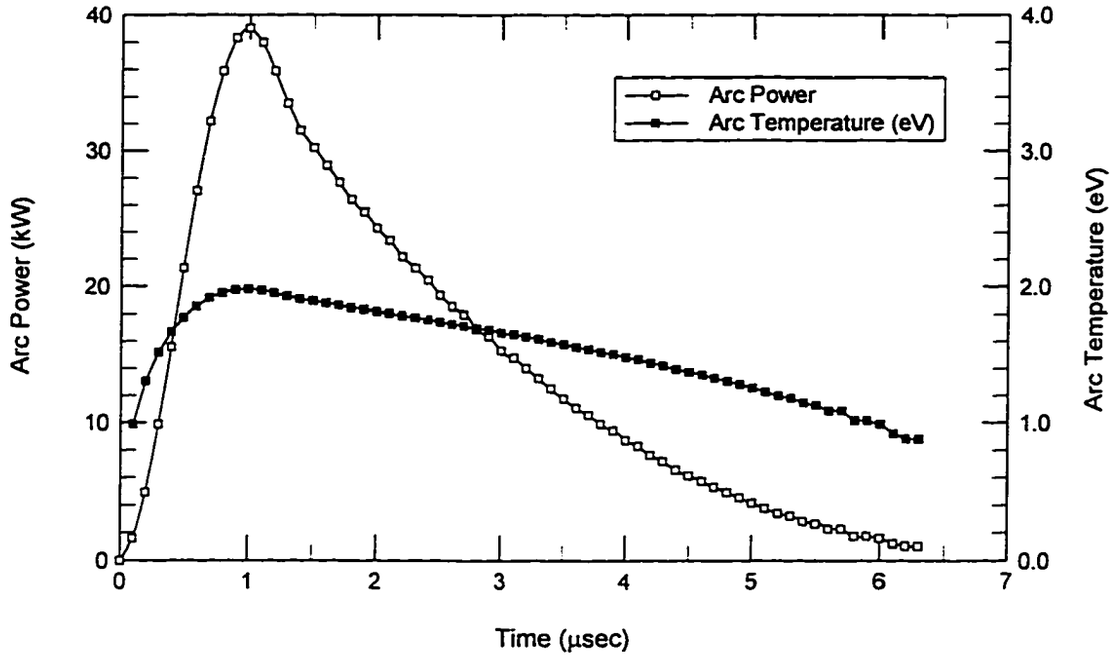

Fig. 5-13. Arc power and arc temperature from the channel model.

5.4 Photodiode Measurement

A photodiode was placed at the exit plane of the arcjet with an axial view of the nozzle throat. The photodiode signal is compared to the arc current measurement in Fig. 5-14. The photodiode is aligned by hand and is not calibrated, so the magnitude of the photodiode signal is not used as a diagnostic. Interestingly, the time of the peak photodiode occurs 2 μsec after the peak current, whereas, the channel model indicates that the peak temperature, peak arc power, and maximum arc radius occur at the same time as the peak current. Though the measurement is relatively simple to implement, a quantitative interpretation of the data is more complex and is not pursued here.

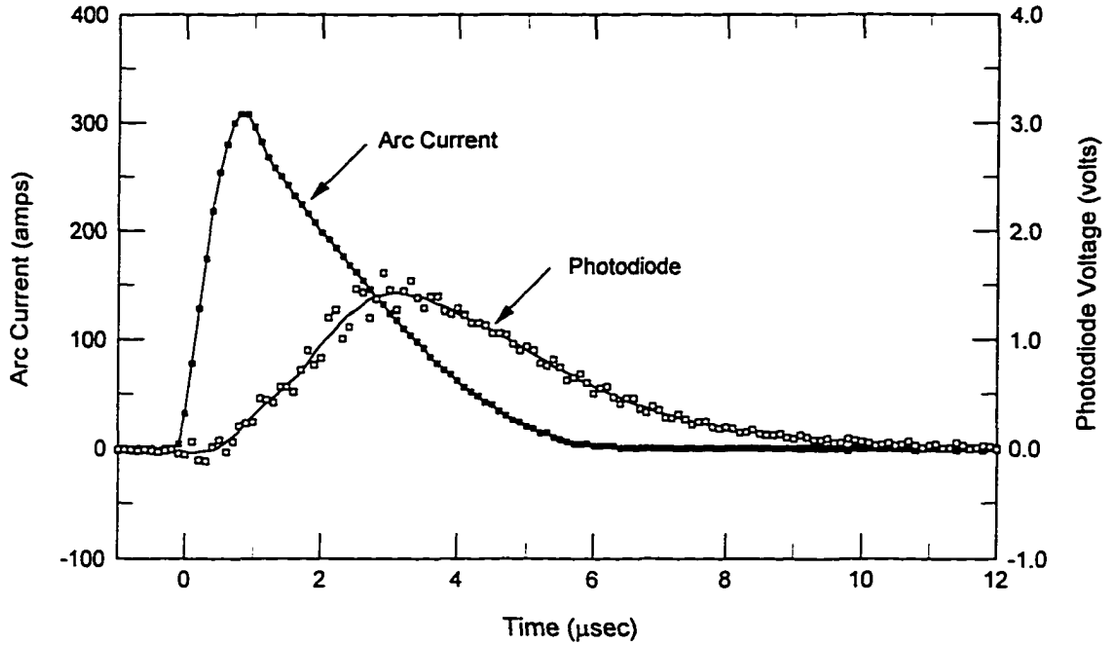

Fig. 5-14. Photodiode signal and arc current during a pulse. The photodiode response can be interpreted as an indication of the relaxation time in the plasma.

5.5 Energy Losses in the External Circuit.

The pulsed arcjet electrical circuit was designed to provide reasonably high efficiency for the transfer of energy from the capacitor to the propellant gas. Even though most of the initial stored energy is transferred to the propellant, the energy losses in the external circuit are non-negligible. The losses in the individual circuit elements can be estimated approximately from experimental data for the breakdown voltage, arc current, and parameters related to each component. From conservation of energy,

$$E_{TOTAL} = E_{ARC} + E_{CAP} + E_{DIODE} + E_{EXT} \tag{5.20}$$

The initial stored energy is given by,

$$E_{TOTAL} = \frac{1}{2} C V_B^2 \tag{5.21}$$

The four terms on the right hand side of the equation are determined in the following sections, where E_{ARC} is the energy transferred to the arc, E_{CAP} is the

energy lost in the capacitor, E_{DIODE} is the energy lost in the diode voltage drop, and E_{EXT} is the energy lost in high frequency resistance of the current path.

5.5.1 Energy Transferred to the Arc

The energy transferred to the propellant from Ohm's law is,

$$E_{ARC} = \int_0^{t_{final}} I^2 R_{ARC}\, dt \tag{5.22}$$

The arc resistance from the channel model is used to calculate the energy transferred to the arc. Alternatively, the constant arc voltage approximation could be used,

$$E_{ARC} = V_{ARC} \int_0^t I\, dt \tag{5.23}$$

5.5.2 Capacitor Losses

The arcjet storage capacitors are required to hold voltages up to several kV and discharge moderate currents of several hundred amperes at kilohertz pulse rates. In addition, the capacitor must have low internal losses to minimize internal heating. The power loss in a capacitor is given by,

$$P_{LOSS} = I_{RMS}^2 \times R_{ESR} \tag{5.24}$$

where R_{ESR} is called the equivalent series resistance of the capacitor. The root mean square current is calculated from

$$I_{RMS} = \frac{1}{\tau} \int_0^t I^2\, dt \tag{5.25}$$

where $1/\tau$ is equal to the pulse rate. The energy loss in the capacitors can be estimated from the discharge current measurement,

$$E_{CAP} = R_{ESR} \int_0^{t_{peak}} I^2\, dt \tag{5.26}$$

Since the current flows in the capacitor only during the first half cycle, the upper integration limit is the time at peak current, generally about 1 μsec. The equivalent series resistance is the sum of the series resistance (connections, leads, foil, terminals), shunt resistance (corona, leakage), and dielectric losses, though generally, the dielectric losses are the dominant loss factor.[17] In an ideal capacitor, the electric charge adjusts instantaneously to the applied electric field. In a real capacitor, there is a time lag for electrical charges in the dielectric to move in response to the applied field. This finite response time results in energy dissipation which is dependent on the frequency of the applied field. The capacitor resistance can be estimated from,

$$R_{ESR} = \frac{DF}{2\pi f C} \tag{5.27}$$

where DF is the dissipation factor, f is the repetition frequency in hertz, and C is the capacitance in farads. The dissipation factor is determined by the design of the capacitor's dielectric system, and DF may depend on frequency and temperature.

5.5.3 Diode

The diode is a critical component of the circuit. Without the diode, the current will oscillate through a series of voltage reversals, dissipating some energy in the capacitor continuously. With the diode, the capacitor is essentially removed from the circuit after the peak current is reached, where the diode provides a return path for the current. The amount of energy dissipated in the diode can be estimated from its voltage drop, which is approximately 2-3 volts.

$$E_{DIODE} = \int_0^t I_{DIODE}\, \Delta V_{DIODE}\, dt = \Delta V_{DIODE} \int_{t_{peak}}^{t_{final}} I\, dt \tag{5.28}$$

This equation is similar to the relationship for arc energy because it is a constant times the integral of the current. The fraction of energy lost in the diode is approximately equal to the ratio of ΔV_{DIODE} / V_{ARC}, or 1-3 percent. From an efficiency standpoint, the energy loss in the diodes is small, though the internal heating in the relatively small diode is not negligible. To keep the diode

temperature within limits during the performance tests, two diodes were installed in parallel connected to a copper heat sink with short leads. Still, for these experiments, the diode temperature was one of the limiting factors in the power levels that could be tested.

5.5.4 High Frequency Resistance

The effective resistance seen by a high frequency signal may be much larger than the dc resistance due to the skin effect. At high frequency, the internal magnetic and electric fields inside the conductor force the current to travel in a thin layer on the external surface rather than being uniformly distributed throughout the conductor cross section. The resistance of the conductor is determined from a cross-sectional area based on the skin depth, δ, given by,

$$\delta = \left(\frac{1}{2} \omega \mu \sigma \right)^{-1/2} \tag{5.29}$$

where ω is the frequency in rad/sec, μ is the relative permeability of the conductor in H/m, and σ is the electrical conductivity in mho/m. The high frequency resistance of all the individual conductors in the arcjet circuit are calculated from,

$$R_{EXT} = \frac{L}{P \delta \sigma} \tag{5.30}$$

where σ is the resistivity, L is the length, and P is the perimeter of the metallic conductors. The total resistances are calculated to be 17 and 21 mΩ at room temperature and at thruster operating temperature, respectively. Of the total resistance, 11 to 13 mΩ are from the inductors. Assuming that R_{EXT} is constant during the discharge, the energy lost in the external circuit resistance excluding the capacitors is,

$$E_{EXT} = R_{EXT} \int_0^{t_{final}} I^2 \, dt \tag{5.31}$$

5.5.5 Transfer Efficiency

The transfer efficiency can be defined as the energy transferred to the arc divided by the initial stored energy,

$$\eta_C = \frac{E_{ARC}}{\frac{1}{2} C V_B^2} \tag{5.32}$$

The theoretical transfer efficiency can be calculated using the analytical model for the arc current and the preceding equations. A comparison of theoretical transfer efficiency for a 100 mJ pulse, V_{ARC} = 150 volts, R_{EXT} = 20 mΩ, for the circuit with and without the diode is shown in Fig. 5-15. The circuit without the diode has lower efficiency due to higher losses in the capacitor. The efficiency also decreases rapidly at low values of inductance, which also corresponds to high peak currents. The circuit with the diode generally has efficiencies of 90-95 percent over a wide range of inductance, and the efficiency is relatively insensitive to values of capacitance. Without the diode, the transfer efficiency is uniformly lower, principally due to greater capacitor losses. The value of the capacitance is important because R_{ESR} is inversely proportional to the capacitance.

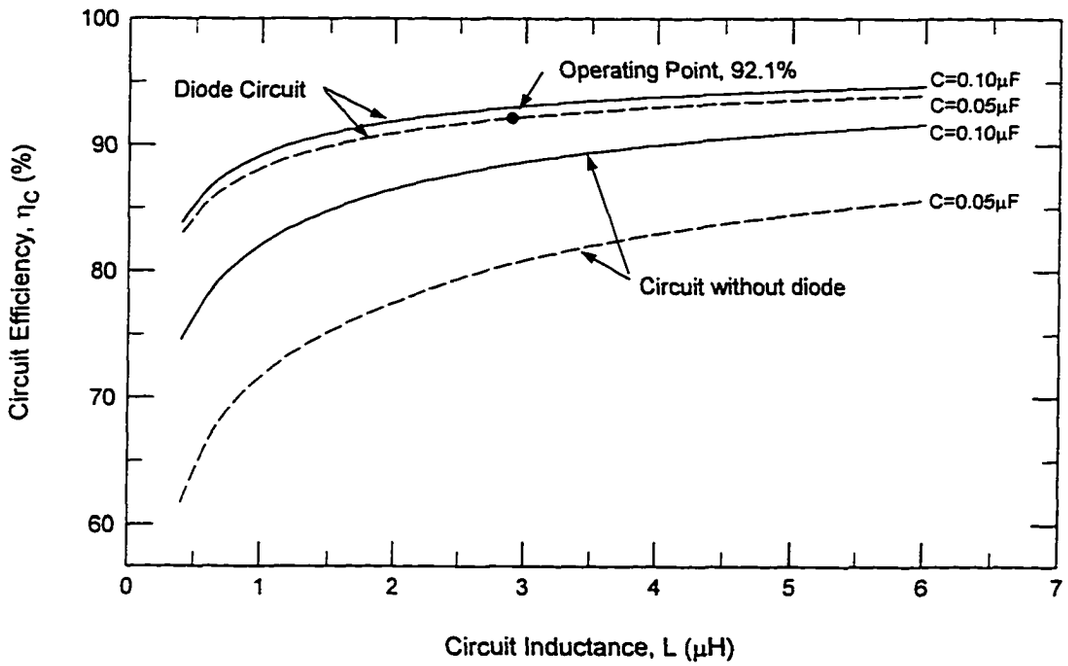

Fig. 5-15. Comparison of theoretical transfer efficiency for the circuit with and without the diode. R_{ESR} for the 0.05 and 0.10 μF capacitors are 250 and 125 mΩ, respectively.

5.5.6 Time Evolution of the Energy Transfer During the Discharge

Experimentally, the transfer efficiency can be obtained by numerical integration of the discharge current data together with the arc voltage obtained from the channel model. All but 4 percent of the energy is accounted for at the end of the pulse. The bulge in the energy summation at the peak current is unexplained, but it is not unexpected because it corresponds to the deviations of the experimental data from the theoretical current at the same time.

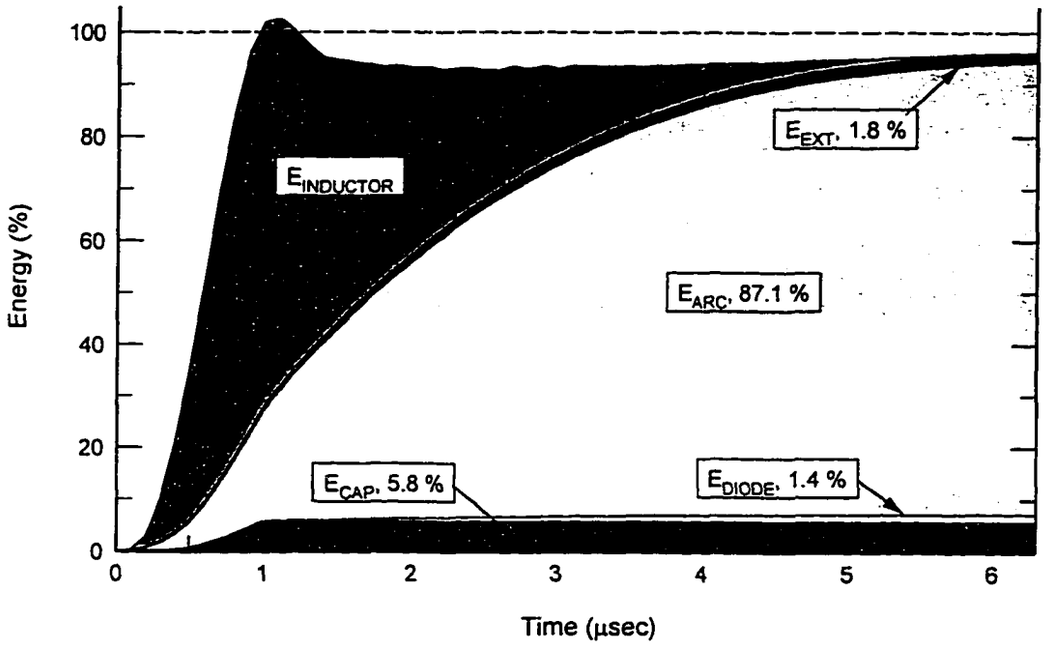

Fig. 5-16. Energy transfer during a pulse, from the experimental arc current and the arc voltage calculated with the channel model.

References

[1] Meek, J. M., and Craggs, J. D., *Electrical Breakdown of Gases*, John Wiley and Sons, New York, 1978.

[2] Brown, S. C., *Basic Data of Plasma Physics*, The M.I.T. Press, Massachusetts, 1966.

[3] Dutton, J., "A Survey of Electron Swarm Data," *J. Phys. Chem. Ref. Data*, Vol. 4, No. 3, pp. 577-758, 1975.

[4] PSPICE, vers. 5.4, computer software, MicroSim Corporation, Irvine, CA, 1993.

[5] Willmes, G. F., and Burton, R. L., "Pulsed Arcjet Performance Measurements," AIAA Paper 95-2823, 1995.

[6] Akiyama, H., Kristiansen, M., Krompholz, H., and Maas, B., "Current-Voltage Characteristics of a High-Current Pulsed Discharge in Air," *IEEE Transactions on Plasma Science*, Vol. 16, No. 2, pp. 312-316, 1988.

[7] Kushner, M. J., Kimura, W. D., and Byron, S. R., "Arc Resistance of Laser-Triggered Spark Gaps," *Journal of Applied Physics*, Vol. 58, No. 5, pp. 1744-1751, 1985.

[8] Lowke, J. J., Kovitya, P., and Schmidt, H. P., "Theory of Free-Burining Arc Columns Including the Influence of the Cathode," 1992

[9] Wong, K. L, and Chen, T. R. "Analysis of Time-Dependent Characteristics for a Pseudospark Discharge in Air," *IEEE Transactions on Plasma Science*, Vol. 19, No. 3, pp. 525-528, 1991.

[10] Bruzzone, H., Kelly, H., and Moreno, C., "The Effect of Transmission Lines and Switching Action on the Electrical Signals in a Powerful Capacitive Discharge," *IEEE Transactions on Plasma Science*, Vol. 18, No. 4, pp. 689-693, 1990.

[11] Engel, T. G., Donaldson, A. L., and Kristiansen, M., "The Pulsed Discharge Arc Resistance and its Functional Behavior," *IEEE Transactions on Plasma Science*, Vol. 17, No. 2, pp. 323-329, 1989.

[12] Robiscoe, R. T., Kadish, A., and Maier, W. B., "A Lumped Circuit Model for Transient Arc Discharges," *Journal of Applied Physics*, Vol. 64, No. 9, pp. 4355-4363, 1988.

[13] Maier, W. B., Kadish, A., and Robiscoe, R. T., "Comparison of the AWA Lumped-Circuit Model of Electrical Discharges with Empirical Data," *IEEE Transactions on Plasma Science*, Vol. 18, No. 6, pp. 1033-1037, 1990.

[14] Robiscoe, R. T., Kadish, A., and Maier, W. B., "Overdamped Arc Discharge Data and an AWA Model," *IEEE Transactions on Plasma Science*, Vol. 19, No. 3, pp. 529-534, 1991.

[15] Peter, Th., "Uber den Zusammenhang des Steenbeckschen Minimumprinzips mit dem thermodynamishen Prinzip der minimalen Entropieerzeugung," *Zeitschrift fur Physik*, Bd. 144, S. 612-631, 1956.

[16] Raizer, Y. P., "Arc Discharge," *Gas Discharge Physics*, Springer-Verlag, Berlin, 1991.

[17] Kingery, W. D., Bowen, H. K., Uhlmann, D. R., *Introduction to Ceramics*, John Wiley and Sons, New York, 1976.

6. Conclusions and Recommendations

The subject of this research was the experimental and numerical investigation of a pulsed arcjet operating on helium propellant at low power. The experimental work required the design and fabrication of the thruster hardware and development of techniques to measure thruster performance and arc characteristics. An important part of this research was the development of the unipolar pulse-forming electrical circuit, which may also have applications in other types of electric propulsion devices. The numerical work consisted primarily of a quasi-1D time-dependent computer code to calculate the specific impulse and thrust efficiency as well as the individual energy losses in the arcjet. The numerical results agreed sufficiently well with the experimental data that additional research can be focused in areas that may improve the thruster performance significantly.

6.1 Design Considerations

6.1.1 Mechanical

In the course of the design and testing of the pulsed arcjet thruster, several problems related to the mechanical design were identified, including the design of the propellant feed system and the thermal design of the thruster head. The inlet area to the capillary must be sufficiently small that the high pressure following a pulse is not wasted by internal leakage within the thruster. In the design used in these experiments, internal leakage was minimized by spring-loading the cathode into the boron nitride capillary. It was also recognized that the propellant feed system should be designed to minimize the time lag in the thrust caused by a change in mass flow rate or input power. The time lag was accounted for in the test procedure, but the thruster time response could be improved by reducing the total gas volume of the feed system.

The experimental data and numerical results show that the nozzle and capillary wall temperatures are important parameters affecting the pulsed arcjet performance. The thermal characteristics of the thruster were improved by

reducing the wall thickness of the front thruster body, but the thermal design based on a 1-kW device required further modifications to run efficiently at low power.

6.1.2 Electrical

A major consideration in the electrical design is the circuit transfer efficiency, since power losses in the external circuit can be large for a poor design. The energy losses for a given circuit can be predicted with reasonable accuracy, and the addition of the diode to the circuit produced transfer efficiencies greater than 85 percent without current reversals in the capacitor.

The power control of the pulsed arcjet turned out to be important because the coupling of the pulse rate to the breakdown voltage without active power control led to instabilities in the arcjet operation. In these experiments, the problem was solved by implementing the power supply control circuit, which eliminated the instabilities in the pulse rate and input power.

6.2 Recommendations for Additional Research

Possibilities for additional experimental work fall into two categories: thruster design enhancements that are intended to increase performance, and diagnostics to improve understanding of the pulsed arcjet physics. With regard to the numerical modeling, both the pulsed arcjet performance code and the channel model for the arc column have areas that would benefit from additional work.

6.2.1 Pulsed Arcjet Performance Enhancements

The numerical results discussed in Chapter 4 indicate that the specific impulse and efficiency of the pulsed arcjet can be increased to higher than 400 seconds and 60%, respectively, for helium propellant. The numerical model indicates that the primary energy loss is heat transfer from the gas to the capillary walls in the subsonic region. Wall temperature is the critical parameter, and the performance is relatively insensitive to the other design variables.

For most of the experimental conditions tested in this research, the nozzle design is not very important, and the performance gains that can be obtained through optimization are small. However, there are conditions where the nozzle

design may be critical, particularly at very low Reynolds numbers and low mass flow rates. The numerical results also indicate that there is an optimum value of the specific energy for a given nozzle at a particular input power. An unexpected conclusion from the numerical model is that average input power has a large effect on I_{SP}, while the influence of the peak power is small.

Several approaches for achieving higher performance in the pulsed arcjet are given as follows:

1. Redesign the pulsed arcjet front end to improve its thermal characteristics. The thruster head should be designed to operate at a high temperature at the desired power level. In addition, the thermal mass of the nozzle and capillary should be sufficiently low that the time to thermal steady state is relatively short, several minutes instead of the 10-15 minutes required in these experiments.

2. Evaluate techniques to reduce heat transfer losses in the capillary. The numerical model indicates that optimization of the basic capillary and nozzle design variables other than the wall temperature is not likely to dramatically improve the specific impulse. However, since capillary heat transfer appears to be such a large loss mechanism, any concepts that could potentially change the heat transfer / blowdown time scales should be investigated.

3. Configure the electrodes and dielectric insulator for diatomic propellants so that the breakdown distance is much smaller than the arc length. The breakdown distance, capillary volume, and value of capacitance, i.e. pulse energy, should be designed for a peak temperature and pressure that minimizes frozen flow losses.

4. Improve the propellant feed system to eliminate the time lag associated with the feed system volume.

6.2.2 Additional Diagnostics

The experiments in this research consisted primarily of overall performance measurements and data for the arc discharge current, and these diagnostics were sufficient to achieve most of the objectives in this research. Additional diagnostics that could be applied in pulsed arcjet tests are discussed below.

1. Obtain quantitative measurements of electrode erosion rates. Electrode erosion could potentially be a major limitation for the long term operation of the device. No measurements of electrode mass loss or total Coulomb transfer were obtained in these experiments, and this aspect of the pulsed arcjet should be investigated.

2. Obtain direct measurements of arc voltage during the arc discharge. Data for the arc voltage could be used to compare results from the channel model. The voltage measurement would also provide a better determination of the circuit transfer efficiency, since the calculations performed here use either the constant arc voltage model or results from the channel model.

3. Apply time-of-flight measurement techniques using probes in the nozzle exhaust to determine flow velocities at the exit plane. This data could be compared with results for exit velocity calculated by the numerical model.

4. Acquire sufficient temperature measurements of the thruster head to allow more accurate experimental evaluation of heat transfer losses. In this research, a single thermocouple mounted on the nozzle was used, and heat conduction to the thruster rear could not be determined with useful accuracy from a single measurement.

5. Evaluate the effect of the capillary dielectric on the breakdown voltage using more precise measurement techniques that eliminate some of the additional variables that were present in these breakdown voltage tests.

6.2.3 Improvements to the Numerical Model

The quasi-1D, time-dependent numerical model is a useful tool for evaluating the pulsed arcjet, and the code provides a reasonable calculation of the individual energy loss mechanisms. Several possible improvements to the model are listed as follows:

1. Improve the modeling of heat transfer in the capillary. Since heat transfer in the subsonic region accounts roughly half of the input energy, this mechanisms should be well understood. In this thesis, heat transfer losses in the capillary are calculated assuming convective heat transfer and a fixed empirical Nusselt number. Even though this assumption gave reasonable results compared to

the arcjet performance data, a more accurate physical representation of the energy transfer is warranted. For example, calculations for radiation heat transfer and heating in the anode and cathode sheaths could be included in the numerical model.

2. Add gas property subroutines and a frozen flow or a finite-rate chemical kinetic model for diatomic propellants such as hydrogen or simulated-hydrazine. The pulsed arcjet may be designed to run on nearly any low molecular weight propellant, though the initial development used helium to simplify both the experiments and the numerical model.

3. Determine if adding a time-dependent term and a radiation term to the Heller-Elenbaas equation is warranted. The arc voltage calculation using the energy equation for a steady arc in a channel gave an arc voltage that matched closely with the constant arc voltage model. However, assuming a form for the energy equation and neglecting radiation may apply only under limited conditions and should be evaluated further.

Appendices

A. Hydrazine

Preliminary experimental work on the pulsed arcjet used simulated-hydrazine (N_2+$2H_2$) propellant because of the advantages of using a storable propellant from an overall spacecraft system standpoint. The decomposition products of hydrazine were simulated using a gas mixture of hydrogen and nitrogen. Initial tests showed relatively poor performance with a maximum specific impulse of 235 seconds and 18% efficiency at 190 watts.[1] At this power level, the nozzle glowed orange at ~1200 K, measured with an infrared pyrometer. The potential to increase the I_{SP} by increasing the wall temperature was limited by the material properties of the boron nitride capillary. Analysis of the external circuit indicated that energy losses in the capacitors could be as high as 45%. Work to improve the circuit efficiency led to the diode circuit design with the unipolar pulse; however, the performance was still unacceptably low with simulated-hydrazine: 190 seconds I_{SP} and 15% efficiency at 85 watts input power, though the nozzle was relatively cold and not glowing in the visual range.[2]

The difficulties in running the pulsed arcjet with simulated-hydrazine are related to the breakdown characteristics of the diatomic gases. Electrical breakdown in hydrogen and nitrogen is more difficult to achieve than in helium, and a combination of low mass flow rates and high voltages was needed to initiate voltage breakdown with the experimental electrode/capillary design. The low flow rates led to large viscous losses in the nozzle as well as high dissociation frozen flow losses from the high peak temperatures following each arc discharge. It may be possible to run the pulsed arcjet with diatomic propellants by configuring the electrodes to make the breakdown distance less than the arc length.

With simulated-hydrazine, the peak temperatures were high enough to affect the wall surface of the boron nitride capillary: the surface became blackened, and the breakdown voltage decreased to <500 volts, independent of flow rate. Breakdown may have been initiating along the capillary wall. When the capillary diameter was drilled to a larger diameter to produce a clean surface, breakdown again followed Paschen's law.

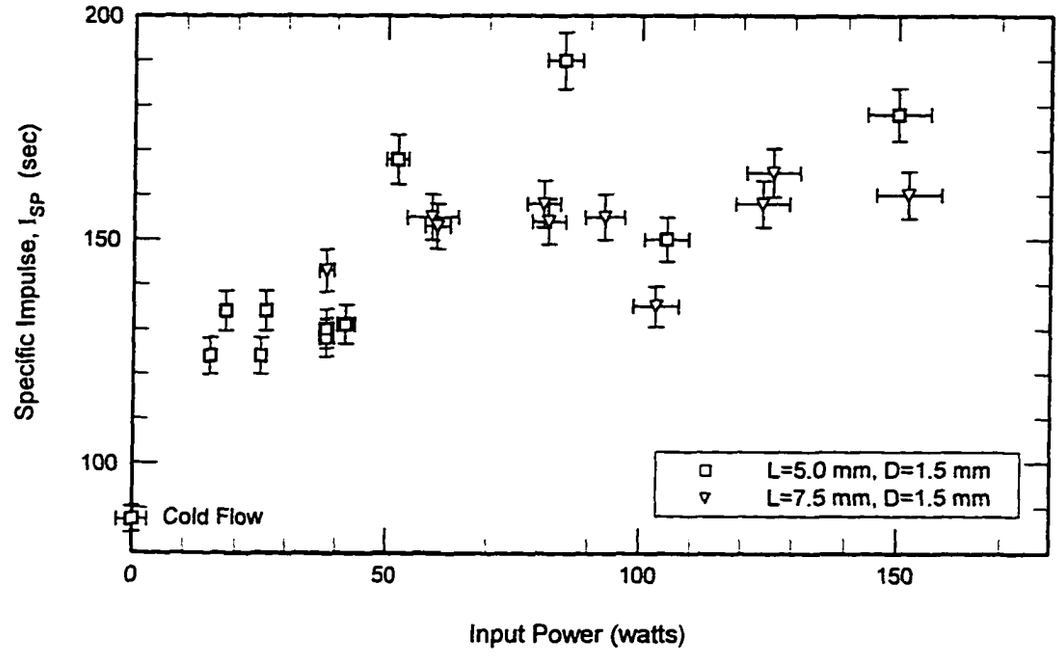

Fig. A-1. Specific impulse with N_2+2H_2 propellant for two capillary geometries with A/A* = 20 and C=0.05 μF.

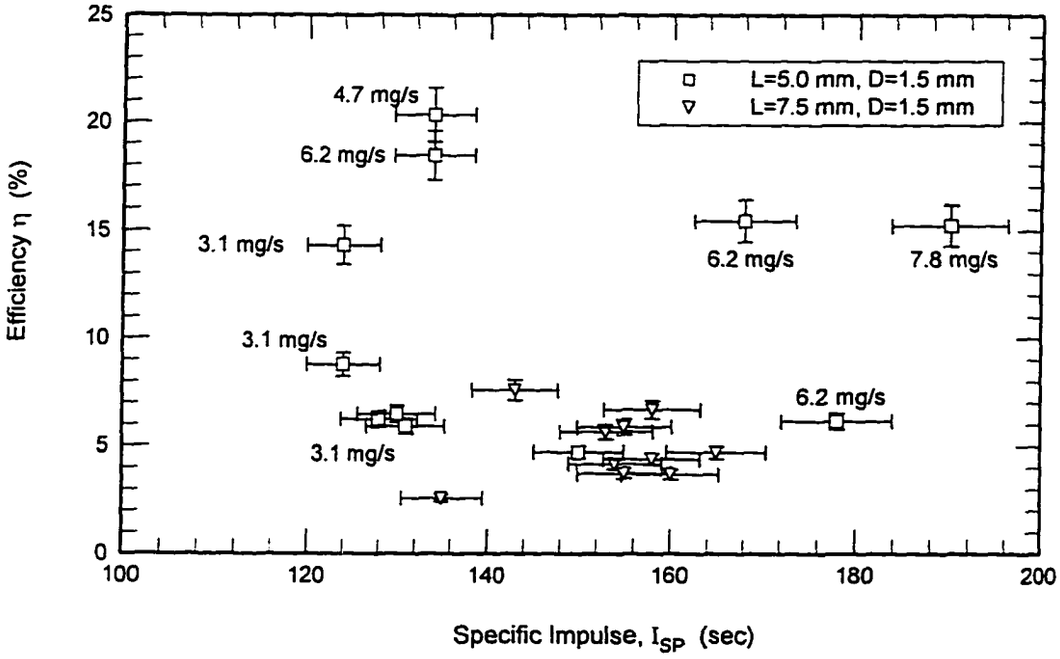

Fig. A-2. Efficiency versus specific impulse for N_2+2H_2. Performance improves at higher mass flowrates.

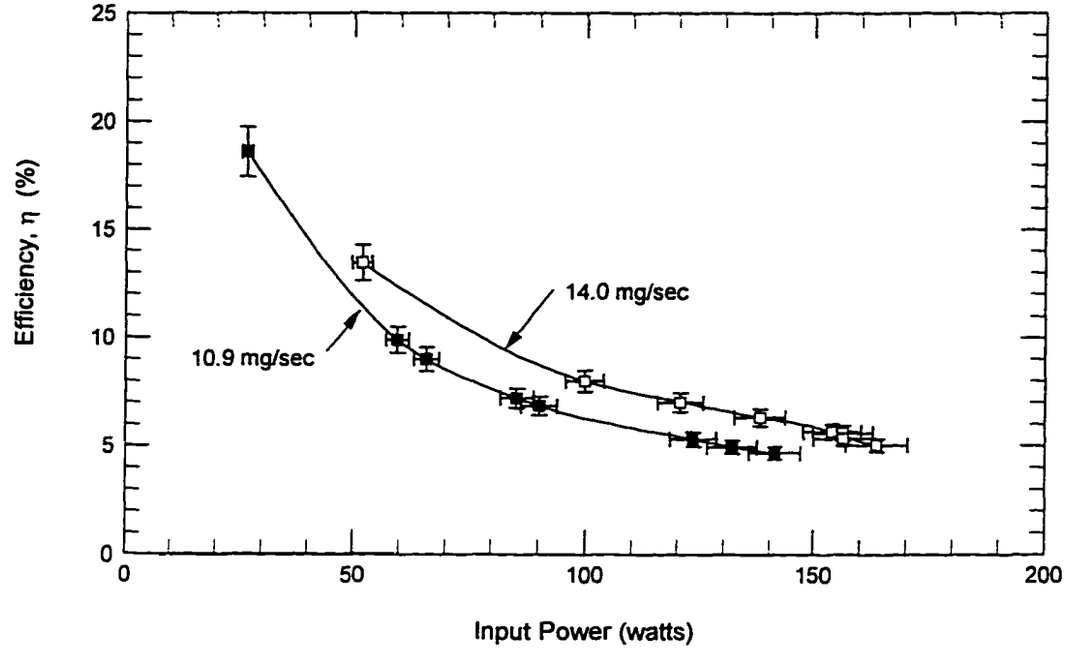

Fig. A-3. Cold wall efficiency with N_2+2H_2. The capillary length and diameter are L=3.7 mm, D=2.8 mm.

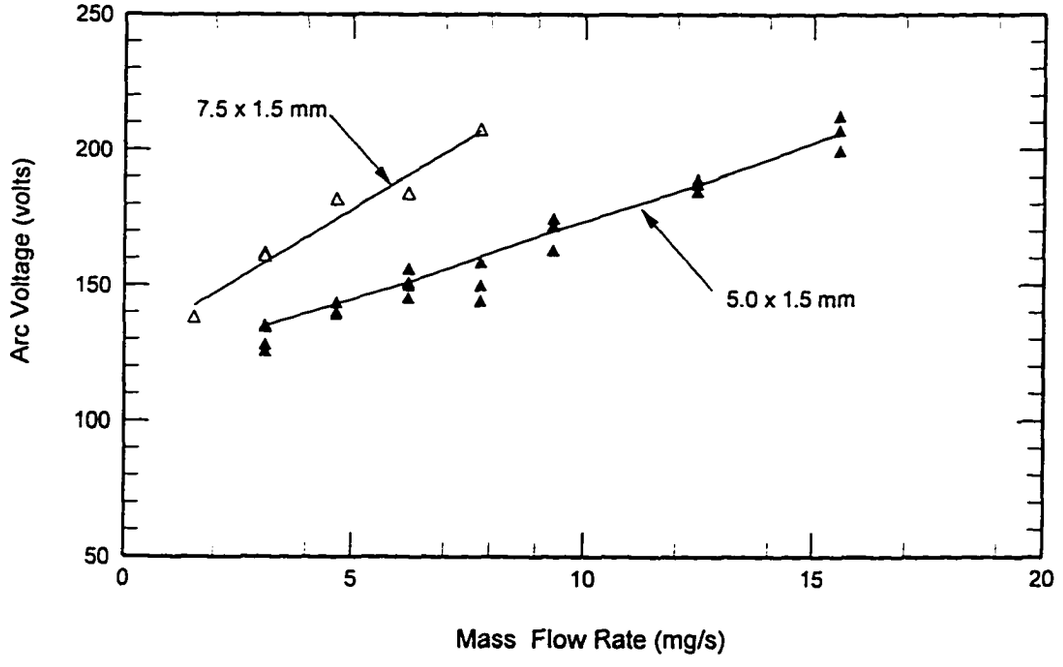

Fig. A-4. Arc voltage for two capillary geometries with N_2+2H_2 propellant.

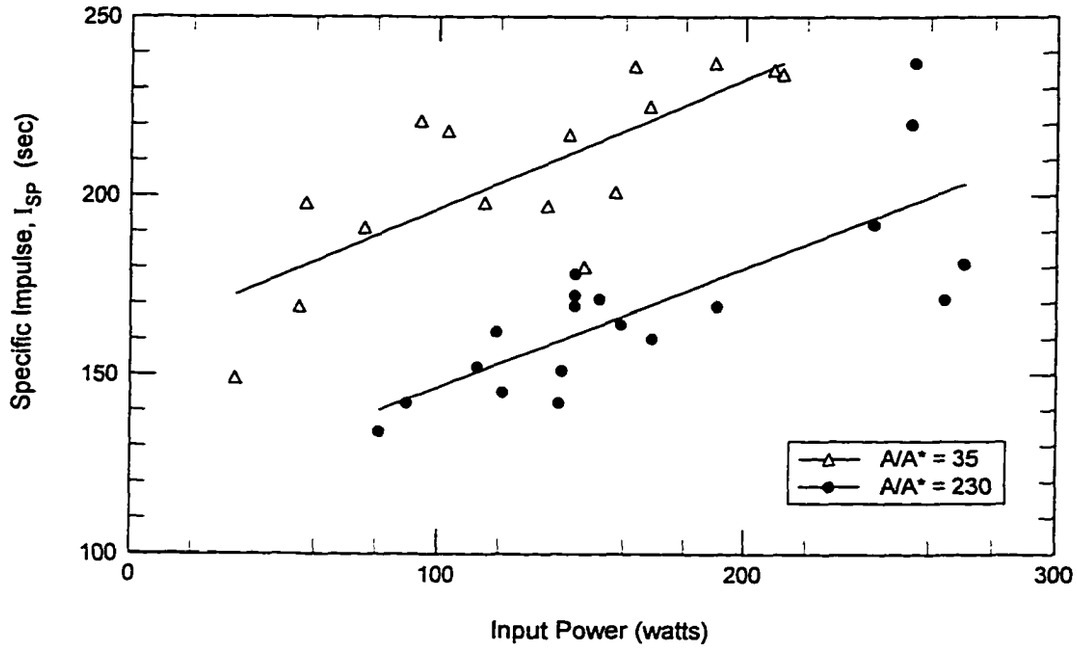

Fig. A-5. Area ratio effects on specific impulse without the diode in the pulse-forming electrical circuit. Losses in the external circuit are 40-50% during these tests.

B. Calibrations and Uncertainty Analysis

B.1 Mass Flow Rate

The mass flow controller is calibrated using a control volume method. The propellant gas fills the control volume at a constant flowrate set by the Unit Instruments flow controller. The initial and final gas pressure and temperature are measured, and the mass flow rate is determined from,

$$\dot{m} = \frac{\Delta m}{\Delta t} = \frac{1}{\Delta t}\left(\frac{P_2 V_2}{R T_2} - \frac{P_1 V_1}{R T_1} \right) \tag{B.1}$$

The uncertainty in this measurement is calculated from,

$$\frac{\omega_{\dot{m}}}{\dot{m}} = \left[\left(\frac{\omega_{\Delta P}}{\Delta P} \right)^2 + \left(\frac{\omega_V}{V} \right)^2 + \left(\frac{\omega_T}{T} \right)^2 + \left(\frac{\omega_t}{t} \right)^2 \right]^{1/2} \tag{B.2}$$

The control volume is 1061.3 ± 10 cm^3. The accuracy of the pressure gauge is taken to be the factory specification, 0.25% + 0.1 psi. Temperature and time are assumed accurate to within 1 degree K and 2 seconds, respectively.

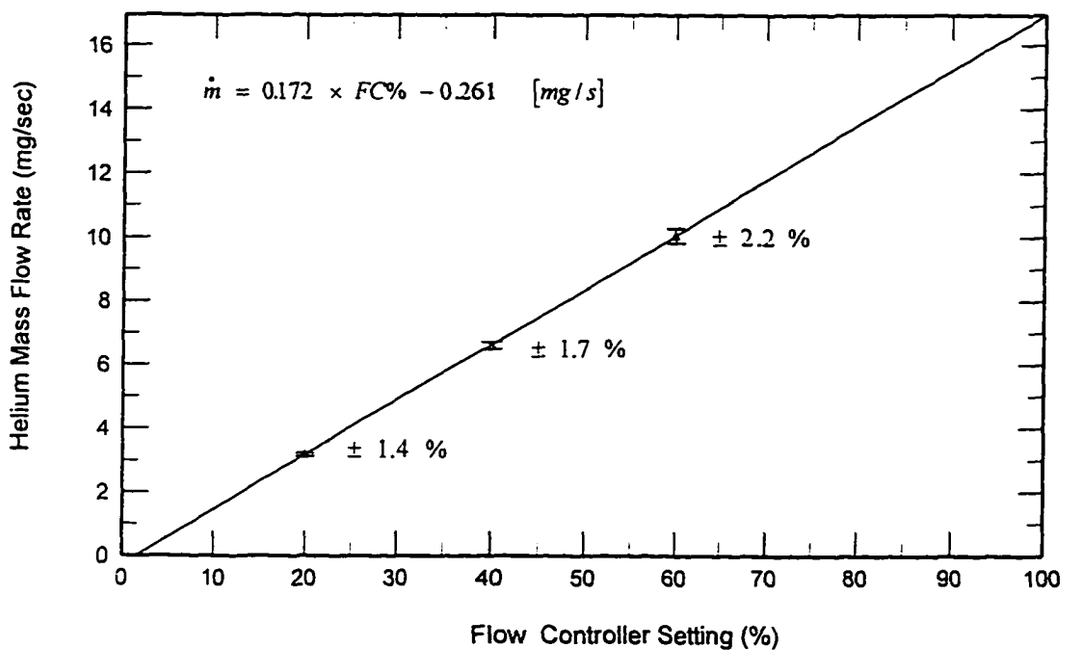

Fig. B-1. The calibration factor for the mass flow rate is obtained from a least squares fit to at least 3 data points at 3 or more different flowrates.

B.2 Thrust Stand Calibration

The thrust calibration system uses a set of three known masses and the pulley arrangement shown in Fig. B-2. The masses are ~1/2 gram lead weights, which are lowered and raised through two complete cycles. The 13 data points are used in a least squares fit to determine the thrust stand calibration factor. The thrust measurement is calibrated before and after each test, and the post-test calibration verifies that the calibration factor did not shift during the test. The thrust stand uncertainty is taken to be 0.8% based on the repeatability of the calibration factor.

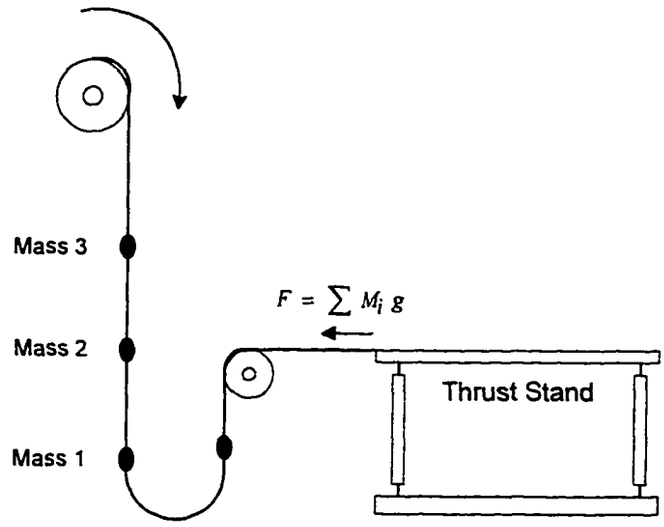

Fig. B-2. Schematic of thrust stand calibration system. The three masses are sequentially lowered and raised to provide known forces to the thrust stand.

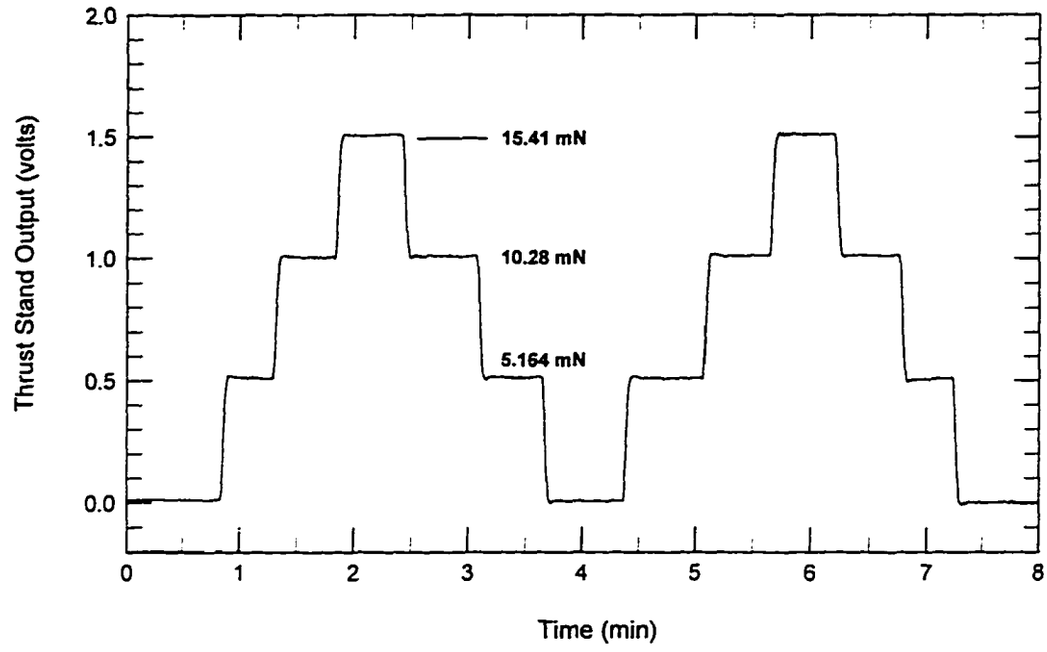

Fig. B-3. The thrust stand output is recorded at each step for a total of 13 data points. A least squares fit is used to obtain the calibration factor.

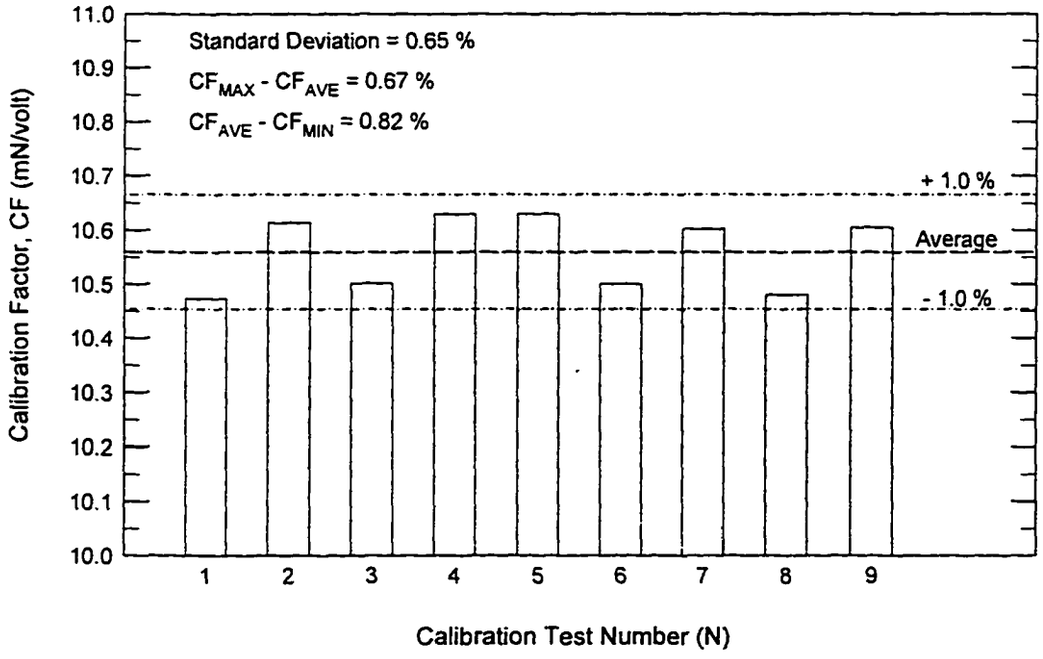

Fig. B-4. The thrust stand calibration factor, CF, is repeatable to 0.8%. Calibration is performed before and after each performance test.

B.3 Breakdown Voltage and Charging Current

An inductive current monitor (Pearson Model 4100) is used to measure the charging current to the arcjet storage capacitor. The high frequency characteristics of the charging current are far from constant (see Fig. B-5); however, the capacitor voltage that results from the integrated current approximates the sawtooth waveform that would result from a constant charge current (Fig. B-6). The data for the charge current is numerically integrated using the trapezoidal rule to obtain the voltage on the capacitor,

$$V_B(t) = \frac{\Delta t}{C} \sum_{t=0}^{\tau} I(t)$$

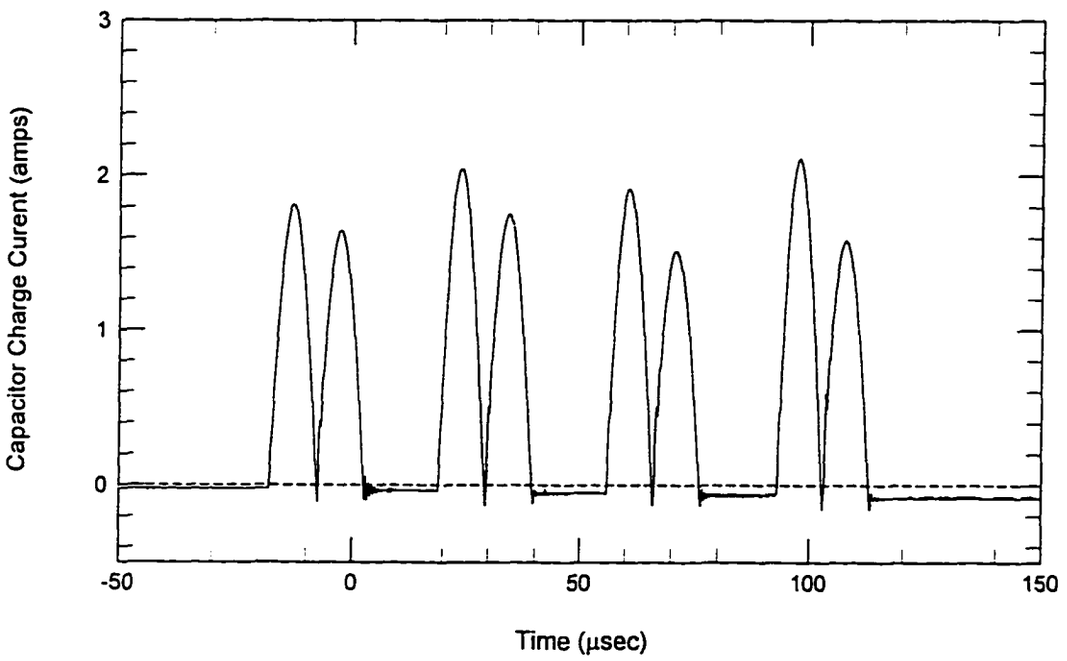

Fig. B-5. Capacitor charging current measured in the power cable to the arcjet. The current data is numerically integrated to provide data for the single pulse breakdown voltage measurements.

The power supply provides a low-level (0-10 volt) analog representation of its high voltage output, and this voltage measurement is compared to the voltage determined from the integrated current. A high voltage probe (Tektronix Model P6015) is used as an additional comparison, although it could not be used during

arcjet operation because it produced high frequency oscillations in the arc discharge. The three measurements of capacitor voltage are shown in Fig. B-6. Since the signal from the power supply exhibits a time lag compared to the voltage from the integrated current, the integrated current is considered a more accurate measurement, and this data is used for the single pulse breakdown measurements described in Chapter 5. The voltage used in determining the arcjet performance in Chapter 4 is from the power supply analog output because an additional signal conditioning circuit would have been needed to use the charging current for measuring the input power.

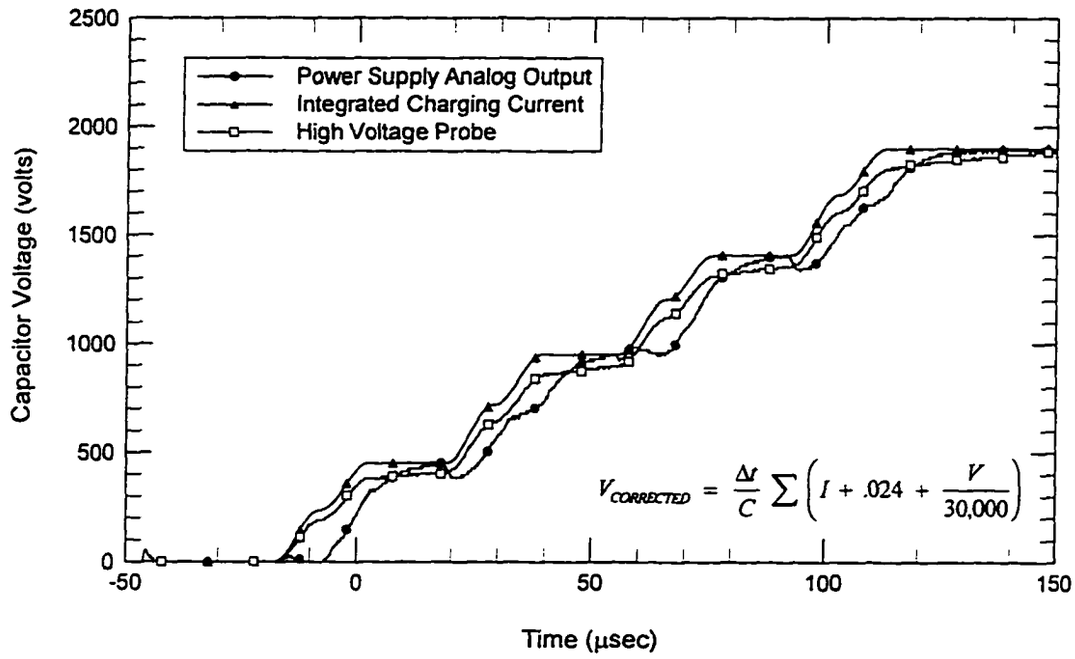

Fig. B-6. Three measurements of capacitor voltage. The integrated current is considered more accurate due to time lags in the other measurements.

B.4 Inductance Bench Tests

The inductance of the pulsed-forming electrical circuit and the internal inductance in the storage capacitor are required in the analysis of the external circuit. The total thruster inductance is obtained from the oscillation frequency for an ideal LCR circuit. The diodes are first electrically disconnected, then the capacitor is charged to a low voltage, ~6-12 volts, and a wire is touched between the cathode and anode to complete the circuit. The current in the circuit is measured, and the inductance is determined by matching Eq. B.3 to the experimental data.

$$I = V_0 \sqrt{\frac{C}{L_{EXT}}} \exp\left(\frac{-R_{EXT}\, t}{2\, L_{EXT}}\right) \sin\left(t \sqrt{\frac{1}{L_{EXT}\, C}}\right) \tag{B.3}$$

Equation B.3 is the solution for the current in an underdamped LCR circuit for the case where,

$$\frac{C\, R_{EXT}^2}{4\, L_{EXT}} << 1 \tag{B.4}$$

The inductance measurement for the complete thruster is shown in Fig. B-7, and the data for the 0.05 μF capacitor individually is shown in Fig. B-8.

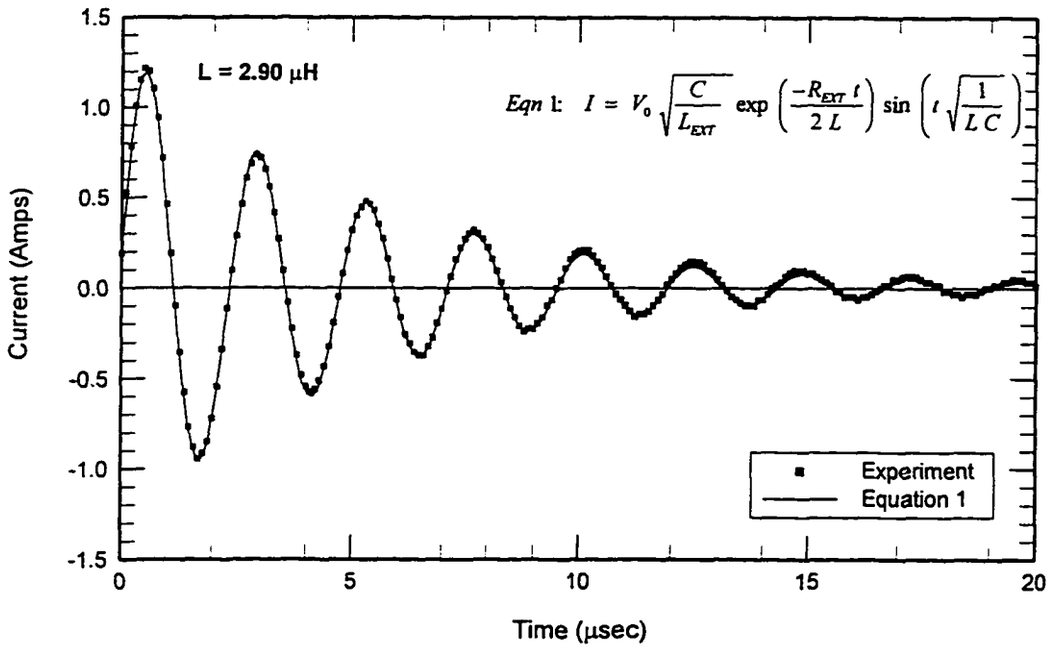

Fig. B-7. Measurement of thruster circuit inductance from oscillation frequency. The diodes are disconnected from the circuit.

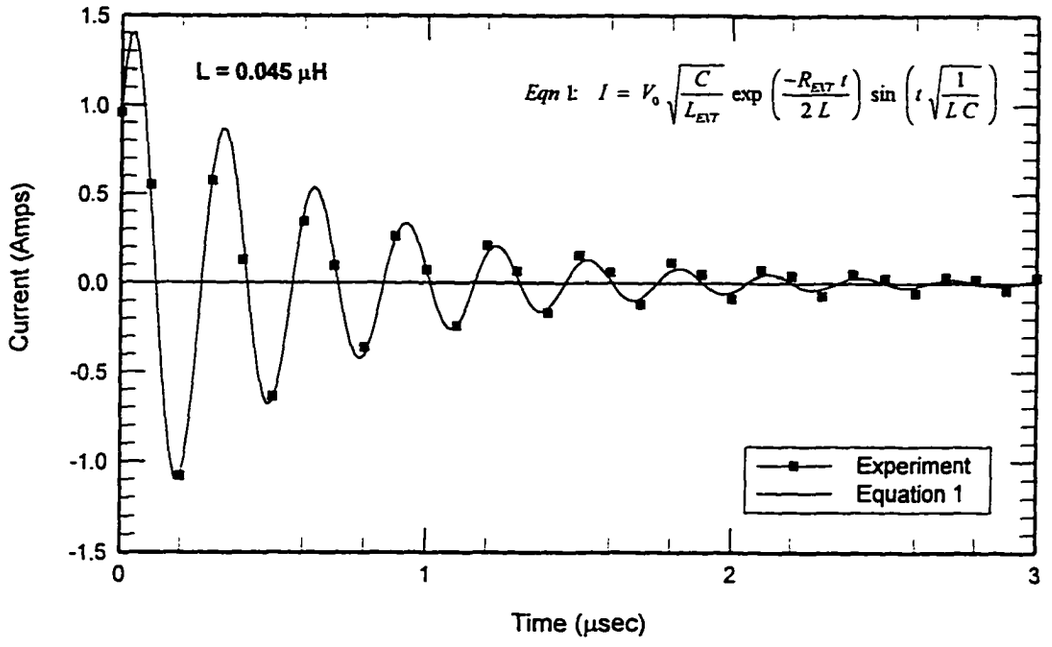

Fig. B-8. Measurement of capacitor internal inductance from oscillation frequency.

C. Electrical Schematics

C.1 Voltage Peak Detector

The pulsed arcjet power is determined from the breakdown voltage and the pulse rate. The 0-10 volt analog signal from the power supply is a series of sawtooth waveforms, and a signal conditioning circuit is required to pick off the breakdown voltage from this signal. The design of the signal conditioner is based on a peak detector described in Horowitz and Hill.[3] A peak detector circuit produces an output voltage that is held to the maximum voltage applied to its input. For the pulsed arcjet, the original circuit design is modified to allow the signal to follow changes in breakdown voltage. To accomplish this, the circuit allows the peak voltage to decay slowly based on an RC time constant that is long compared to the time between pulses but short compared to the 2 samples-per-second recording rate. During thruster operation, the peak voltage measured with this circuit tracks the actual breakdown voltage within 2% at a pulse rate of 500 pps and within 0.5% at a pulse rate of 2000 pps.

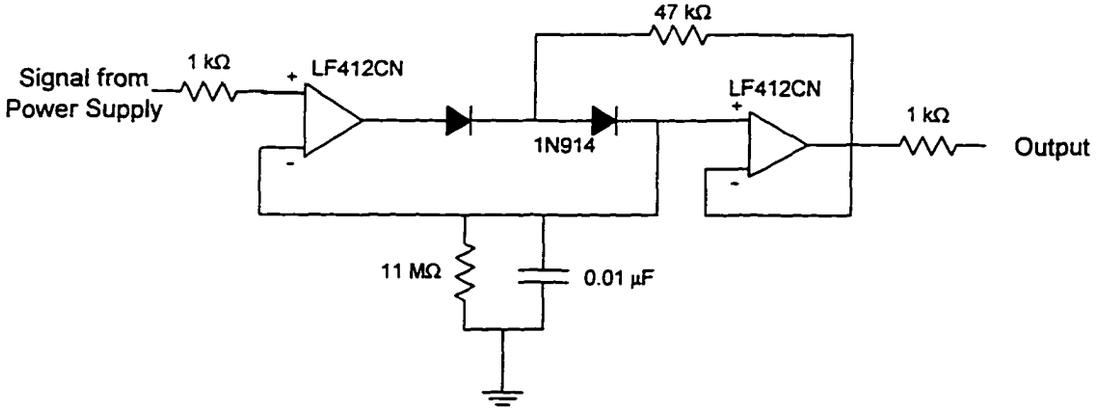

Fig. C-1. Breakdown voltage signal conditioning circuit. The peak detector tracks the breakdown voltage during thruster operation.

C.2 Pulse Rate Signal Conditioner

The analog output signal from the power supply is used to measure the arcjet pulse rate. This signal conditioning circuit uses a frequency-to-voltage converter chip (National Semiconductor LM2917N). The output signal has a 42

msec response time and an accuracy of 1 percent based on the linearity of the LM2917N chip. The signal conditioning circuit is calibrated using a WaveTek Model 147 sweep function generator.

C.3 Single Probe

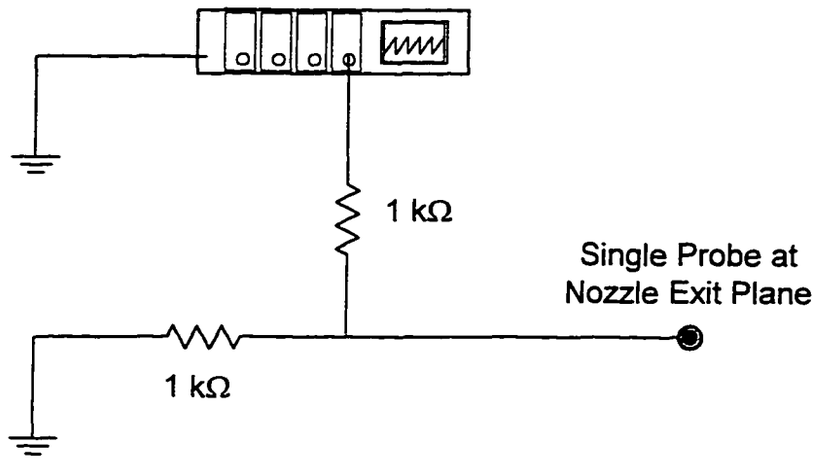

Fig. C-2. Circuit for measuring plasma potential in the plume.

C.4 Photodiode

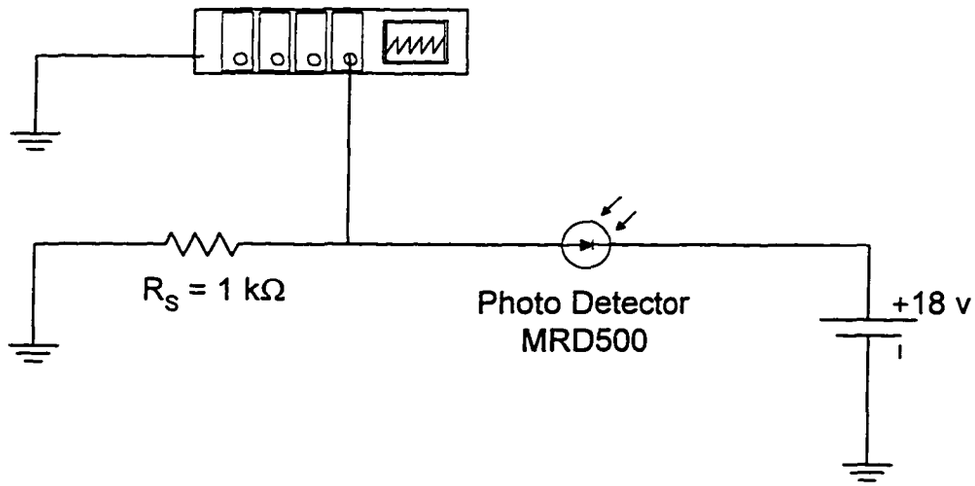

Fig. C-3. Photodiode circuit.

C.5 Power Supply Control Circuit.

The input signal to the control circuit is the 0-10 volt analog output from the power supply analog output with a 1000:1 gain. Since the thruster breakdown in 1000-2000 volts, the input to the control circuit is 1-2 volts. This input signal is amplified with a gain of 3:1. When the arc discharges, the falling edge of the power supply voltage is not steep enough to trigger the one-shot directly, and so a comparator is used to transform the analog signal to a 15 volt square wave, which has a much steeper falling edge. The diode at the comparator input keeps the voltage above -0.6 volts. The comparator circuit allows for hysterisis in order to eliminate multiple transitions that could be caused by a noisy input.

An RC pair (100 pF, 200 kΩ) functions as a differentiator. When the signal from the differentiator goes negative, the output of the one-shot goes high. The signal from the differentiator will increase back to its reference voltage based on the RC time constant, C2 R9. The output of the one-shot will remain high until the voltage on the capacitor C3 decays below the reference voltage set by the voltage divider R9, R10. the duration of the output pulse is determined by the time constant R12, C3. A rotary switch is used to select different values of R12, which sets different values for the 15 volt inhibit signal which controls the power supply.

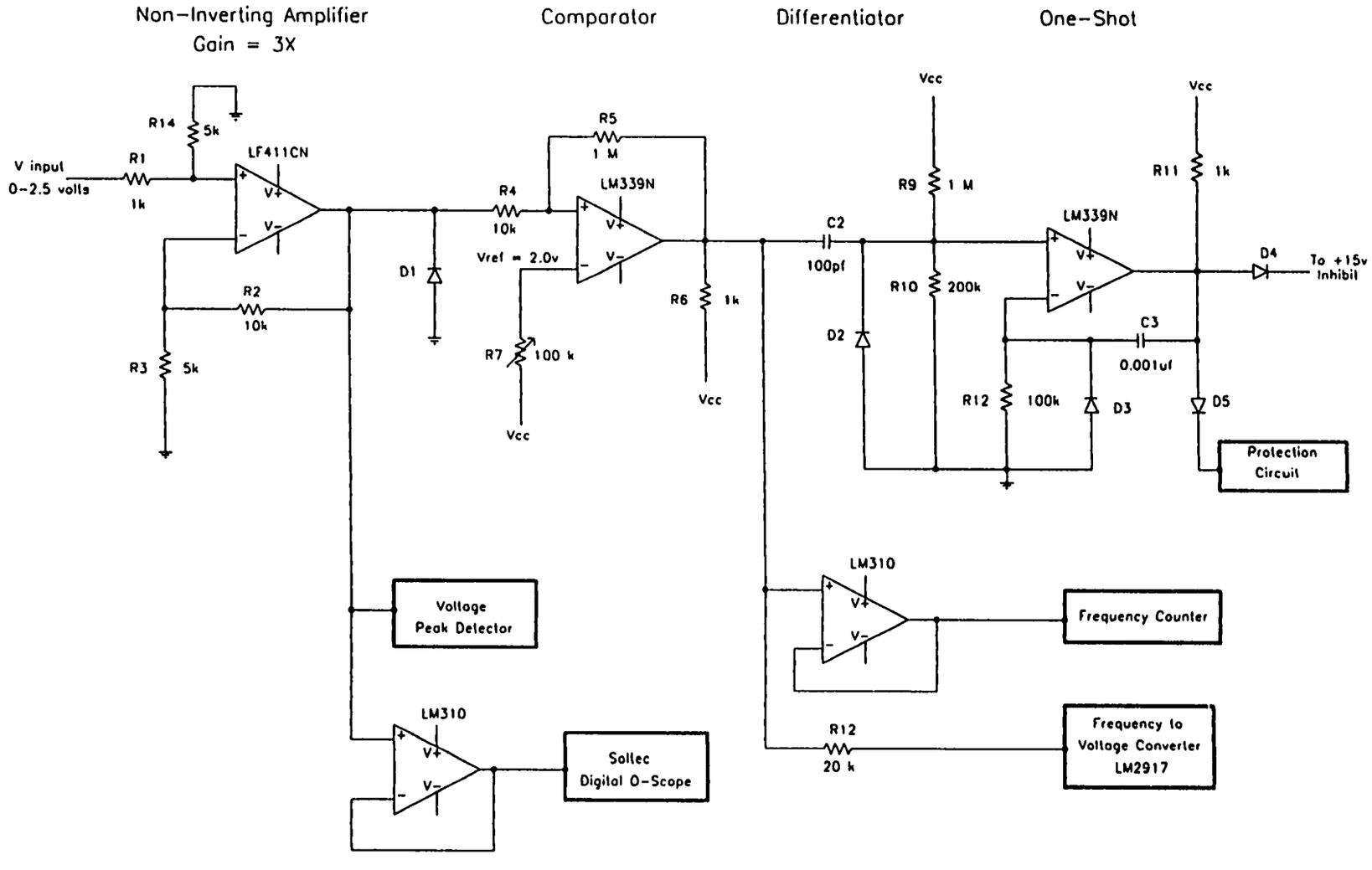

Fig. C-4. Power supply control circuit.

D. Equations for Constant Arc Voltage

The arc current, I(t), in the constant arc voltage model is calculated analytically using the equations from Robiscoe, et al.[4] The input variables are the arc voltage, V*, the breakdown voltage, V_0, and capacitance, resistance, and inductance (C, R, and L) of the external circuit

$$I = (-1)^K \left(|V_K| - V^*\right) A \exp\left[\frac{-R}{2L}(t - t_{K-1})\right] \sin\left[\omega(t - t_{K-1})\right] \qquad \text{(D.1)}$$

$$\textit{where} \quad t_{K-1} < t < t_K \quad \textit{and} \quad V_K \equiv V(t_{K-1}).$$

The variables in the above equations are determined from the following equations:

$$A = \omega C \left(1 + \frac{R^2}{4L^2\omega^2}\right) \approx \sqrt{\frac{C}{L}} \qquad \text{(D.2)}$$

$$\omega^2 = \frac{1}{LC} - \frac{R^2}{4L^2} \qquad \text{(D.3)}$$

$$V_{K+1} = (-1)^K (1 + \eta) V^* - \eta V_K \qquad \text{(D.4)}$$

$$\eta = \exp\left(\frac{-R\Delta}{2L}\right) \qquad \text{(D.5)}$$

$$\Delta = t_K - t_{K-1} = \frac{\pi}{\omega} \qquad \text{(D.6)}$$

E. Transport Properties of Helium

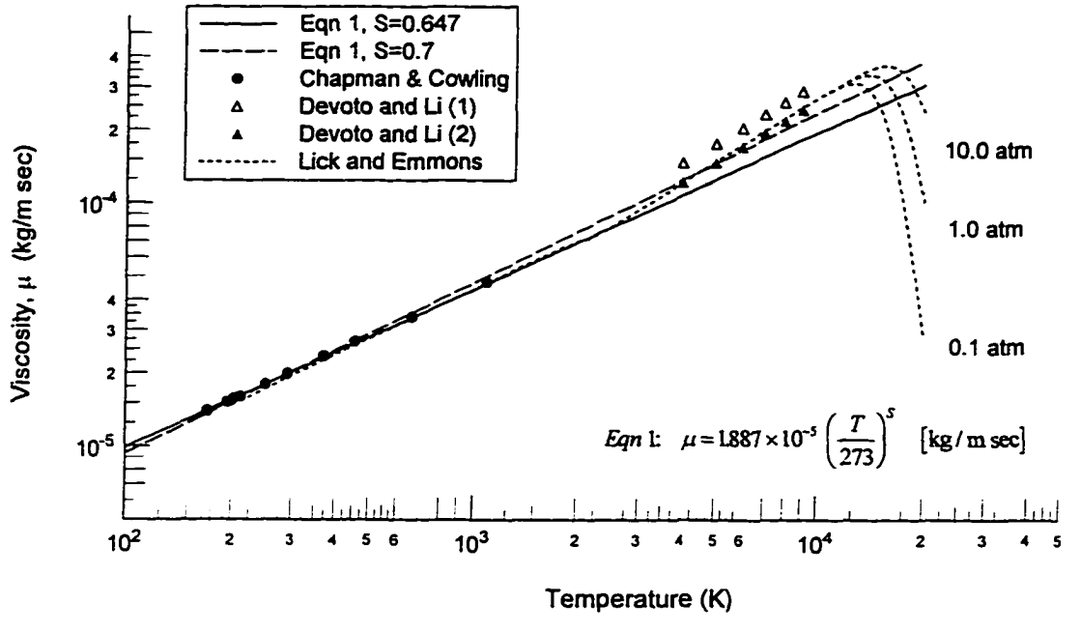

Fig. E-1. Helium viscosity from Chapman and Cowling,[5] Devoto and Li,[6] and Lick and Emmons.[7]

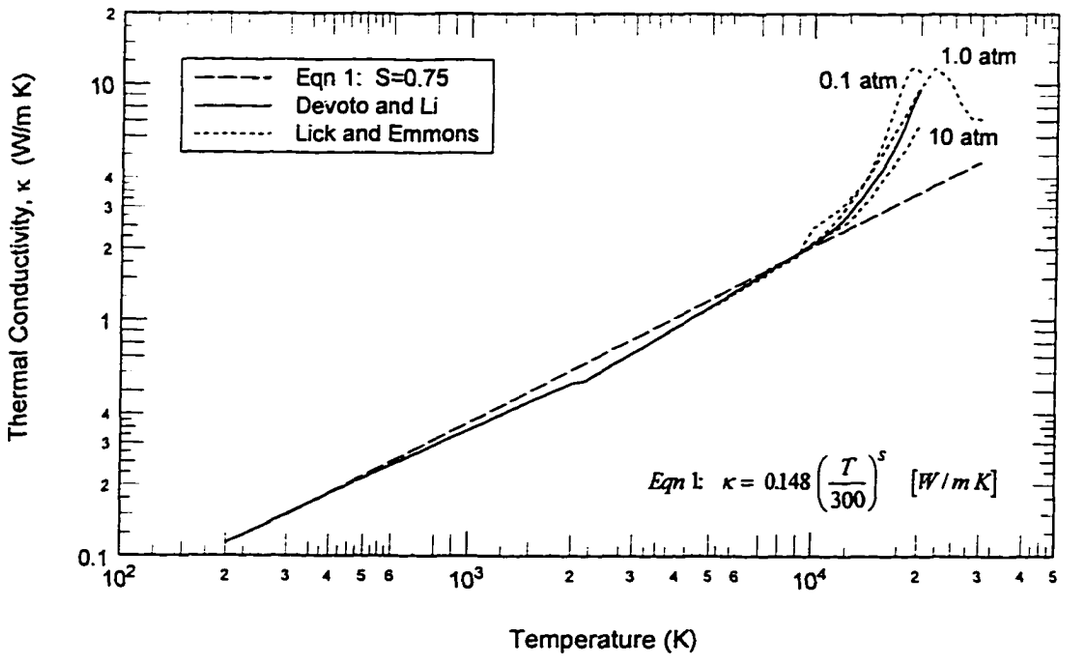

Fig. E-2. Helium thermal conductivity from Devoto and Li,[6] and Lick and Emmons.[7]

The electrical conductivity for a fully ionized gas is calculated using the Spitzer formula,[8]

$$\sigma = 1.53\times10^{-2}\ \frac{T^{3/2}}{\ln\Lambda}\quad [ohm-m]^{-1} \tag{E.1}$$

For a weakly ionized gas, the electrical conductivity is calculated by accounting for electron-neutral collisions,

$$\sigma = 4.535\times10^{-12}\ \frac{n_e}{\sqrt{T}}\ \frac{1}{\left(n_{He}Q_{ea} + \frac{n_e Q_{ei}}{1.975}\right)}\quad [ohm-m]^{-1} \tag{E.2}$$

$$Q_{ei} = 6\,\pi b_0^2\,(\ln\Lambda - 1.37)\quad [m^2] \tag{E.3}$$

$$\Lambda = 1.24\times10^{7}\sqrt{\frac{T^3}{n_e}} \tag{E.4}$$

$$b_0 = \frac{5.56\times10^{-6}}{T}\quad [m] \tag{E.5}$$

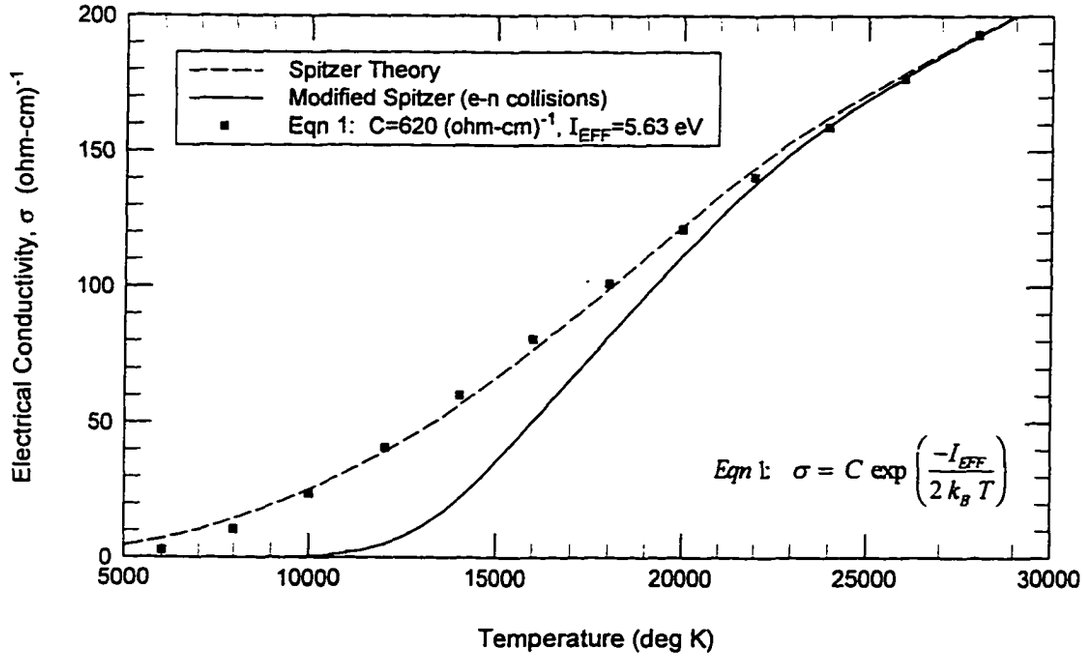

Fig. E-3. Helium electrical conductivity versus temperature.

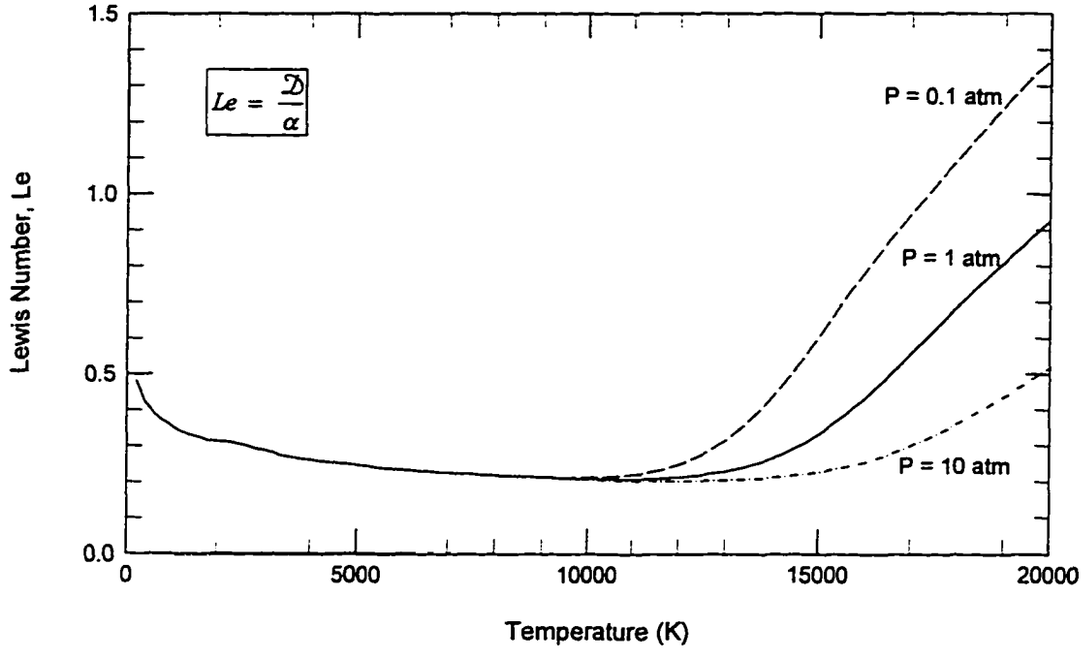

Fig. E-4. Lewis number for helium, from the calculations of Lick and Emmons.[7]

References

[1] Willmes, G. F. and Burton, R. L., "Pulsed Arcjet Performance Measurements," AIAA Paper No. 95-2823, July 1995.

[2] Willmes, G. F., and Burton, R. L., "Performance Measurements and Energy Losses in a 100 Watt Pulsed Arcjet Thruster," AIAA Paper No. 96-2966, July 1996.

[3] Horowitz, P., and Hill, H., "Feedback and Operational Amplifiers," *The Art of Electronics, 2nd ed.* Cambridge University Press, 1989.

[4] Robiscoe, R. T., Kadish, A., and Maier, W. B., "A Lumped Circuit Model for Transient Arc Discharges," *Journal of Applied Physics*, Vol. 64, No. 9, pp. 4355-4363, 1988.

[5] Chapman, S., and Cowling, T. G., "Viscosity: Comparison of Theory with Experiment," *The Mathematical Theory of Non-Uniform Gases, 3rd ed.*, Cambridge University Press, Cambridge, 1970.

[6] Devoto, R. S., and Li, C. P., "Transport Coefficients of Partially Ionized Helium," *Journal of Plasma Physics*, Vol. 2, No. 1., pp. 17-32, 1967.

[7] Lick, W., J., and Emmons, H. W., "Transport Properties of Helium from 200 to 50,000 K," *Physics Reference*, Harvard University Press, 1965.

[8] Mitchner, M., and Kruger, C. H., "Collisional and Radiative Processes," *Partially Ionized Gases*, John Wiley & Sons, Inc., 1973.

Vita

Gary Francis Willmes was born on August 7, 1963 in Livonia, Michigan. His parents are Francis E. and Carol L. Willmes, and he has a sister, Karen, and a brother David. He graduated from East Grand Rapids High School in 1981 and then moved to upstate New York to attend Rensselaer Polytechnic Institute, receiving his Bachelor of Science degree in aeronautical engineering in 1985. Having been an AFROTC cadet for four years, he was commissioned a 2nd lieutenant in the U.S. Air Force and was assigned to the Aero Propulsion Laboratory at Wright-Patterson AFB in Ohio where he was a program manager in the Turbine Engine Division. He attended the University of Dayton part time to obtain a Master of Science degree in aerospace engineering. In 1987 he married Liesel Golden, also a lieutenant in the Air Force, and was transferred to Vandenberg AFB, CA in 1988. He was assigned to the 6595th Aerospace Test Group and worked on six successful Titan launches at Space Launch Complex Four. As a member of the launch crew for the first West Coast Titan IV, he received the Air Force "Best Space Operations Crew" award in 1991. In 1992 he separated from the Air Force at the rank of captain to pursue a Ph.D. at the University of Illinois. On his happiest day, he became a father when his daughter Megan was born in 1993. During his nearly five year course of study, he was a University Fellow, an Aerospace Illinois Fellow, and a research assistant. He was awarded the Roger Strehlow award for outstanding research in 1997.

Gary has accepted a position at the Primex Aerospace Company in Redmond, Washington as a senior development engineer to continue working in the field of electric propulsion.